Measurements of Solvent Effects on Local Barrier Heights in Scanning Tunneling Microscopy

Thesis by

Teresa L. Longin

In Partial Fulfillment of the Requirements

for the Degree of

Doctor of Philosophy

California Institute of Technology

Pasadena, California

1995

(Submitted March 17, 1995)

Acknowledgments

No thesis is the sole work of one person; various individuals contribute varying degrees of intellectual and emotional assistance. This thesis had a lot of assistance. The first person I want to thank is my advisor, Nate Lewis. Nate's intelligence, scientific integrity, and enthusiasm for teaching are inspiring and encouraging. I greatly appreciate his support for my teaching goals; I also appreciate that he never gave up on me.

Mike Heben and Reg Penner started the STM project in the group and taught me the fundamentals of the technique. Rik Blumenthal and Russ Pylkki worked with me in later stages of the project; they and Tom Dunn taught me more about the design, building, and maintenance of electronics than I ever dreamed I'd learn. Iver Lauermann and Alan Rice taught me how to use the UHV apparatus and never yelled at me when I screwed up. They were also very soothing influences on some of my more hideous days. I am profoundly greatful to Art Hubbard and Doug Frank at the University of Cincinnati for their help in preparing the Pt-I surface I needed for my experiments. I imagine that, without their help, this thesis would be much thinner.

The Lewis group in general has always provided an incredible environment for learning. Amit Kumar, Bruce Tufts, Mike Sailor, Sharon Lunt, Gail Ryba, Xiuling Li, Marcel Sturtzenegger, Gary Shreve, Ming Tan, Chris Kenyon, Ashish Bansal, SonBinh Nguyen, Janet Kesselman, Chris Karp, Kathy Pomykal, Arnel Fajardo, Chris Claypool, Mark Lonergan, Marion Cass, Stephen Doig, and Marya Lieberman have provided me with useful or at least amusing conversations over the years. Gail was (and still is) particularly inspiring in her ability to be an excellent scientist, a remarkable athlete, and a very good person, all in one package. Gary and Nancy Shreve fed me, drank with me, and otherwise lifted my spirits on many occasions. Particular thanks go to Marcel, Chris C., Mark, Stephen, Ashish, and Marya for reading and editing various portions of this thing.

Enough of the sober, intellectual acknowledgements; time for the not so sober, intellectual thanks. Karen Shannon, Elizabeth Burns, Chrissy Nelson, and Elaine Marzluff have been very good friends. Their

friendship and support over the years have greatly reduced my need for therapy. Chrissy, in particular, shares my penchants for hiking and tequila, and her presence made grad school bearable on many occasions.

Donnie Cotter will always have my gratitude for introducing me to backpacking. He and Sakae Suzuki were always up for a nice death march, and I've seen alot of the Sierras and San Gabs with one or the other. The Bercaw group has permitted me to tag along on several of their trips, and they have always proved to be charming companions. Pat Kearney came back to check on me on a couple of trips--his concern was and still is greatly appreciated (particularly on the trail).

Many people have helped make grad school not so bad in other ways. Chrissy, Elizabeth, Christy, Sharon, Gary, Nancy, Donnie, Leroy, Amit, Sharad, Bob, Mick, Chris K., Andy, Neil, Gui, Tim, Alison, Susan, Stephen, Marion, Limey, and Karl have shared the occasional pitcher of beer or bottle of wine with me at the Ath and other places. I have many pleasant if somewhat hazy memories of evenings spent in their company.

My family has been a constant, reliable source of emotional (and occasionally financial) support. My parents listened with sympathy to my depressed phone calls and always suggested that I come home for a while, which was always the right thing to say. They deserve alot of credit for my degree.

If I've missed anyone who should be listed here, I'm sorry and thanks for all the help.

Abstract

Scanning tunneling microscopy (STM) has proven to be a powerful tool for obtaining atomic resolution images of surfaces and adsorbates on surfaces. In addition, the technique can be used to make highly localized electronic measurements of surfaces, adsorbates, and molecules in the tunnel gap. Such measurements, generally known as scanning tunneling spectroscopy (STS), can probe either the electronic density of states or the effective barrier height. Studying the effects of solvent on the effective barrier height is particularly interesting, since that is a direct measure of the bridging capacity of the solvent and has analogs in heterogeneous electron transfer and electron transfer in proteins and frozen glasses. Unfortunately, the effective barrier height as measured in STM experiments is very sensitive to contamination on the sample surface and on the tip, and it is difficult to differentiate between solvent effects and contamination effects. We attempted to measure effective barrier heights in air and in hexadecane using a solvent compatible STM and a sample whose surface is resistant to contamination. The cleanliness and order of the sample surface was determined before and after STM experiments using LEED and XPS, and estimates were made of the degree of contamination. Unfortunately, the barrier heights in air were much lower than expected (<1 eV) and indistinguishable from those measured in hexadecane.

Table of Contents

Chapter 1:
General Introduction:
Principles of Scanning Tunneling Microscopy

Introduction

The first scanning tunneling microscopy (STM) images[1] and scanning tunneling spectroscopy (STS) measurements[2] showed that spatially localized studies with angstrom resolution were feasible. Since then, atomic resolution images have been obtained in a variety of environments, including ultrahigh vacuum,[1,3] air,[4] non-polar solvents,[5] pure water,[6] and water containing concentrated electrolytes.[7] A surprising range of substrates have been imaged, such as biological molecules,[8] ordered arrays of organic molecules,[9] and thick organic films such as Langmuir-Blodgett films[10] and self-assembled monolayers of alkanethiols on silver and gold.[11] In addition, the basic technology involved in STM has spawned a variety of techniques for obtaining highly spatially resolved information. Such techniques include atomic force microscopy,[12] scanning electrochemical microscopy,[13] and near-field scanning optical microscopy.[14] Scanning tunneling microscopy and its related techniques have proven to be versatile and powerful tools for exploring the world at a truly microscopic level.

Scanning tunneling microscopy is based on the phenomenon of quantum mechanical tunneling. When two conductors (such as a sharpened metal tip and a conducting solid) are brought within a few angstroms of each other and a bias voltage applied across them (as depicted in Figure 1), electrons will tunnel through the energy barrier between them. The probability that electrons are transmitted, which translates into current density, is related to the extent of overlap of the wavefunctions on each side of the barrier. Since the wavefunctions tail off exponentially into the vacuum, the current is exponentially related to the width of the barrier, usually referred to as the tunnel gap.

In the simplest approximation, for low bias voltages and low temperatures (i.e., normal operating conditions for most STM experiments), the tunneling current can be expressed as:[15]

$$i_t \propto V_B \exp(-A\phi_{eff}^{1/2} s)$$

where V_B is the bias voltage, A is a constant equal to 1.025 $eV^{-1/2}Å^{-1}$ when using the free electron mass, ϕ_{eff} is the barrier height in eV, and s is the gap

width in angstroms. A detailed discussion of this equation and the various factors in it appear in the next chapter. The important aspects to note are the exponential dependence on the distance between the tip and the sample and on the square root of the barrier height. In the ideal case, the effective barrier height is the average of the work functions of the materials composing the tip and the sample; this value is in the range of 4-6 eV for most metals and semi-conductors. Thus, for a one angstrom increase in the gap width, the tunneling current should decrease by about an order of magnitude. It is this exquisite dependence of the current on the tip-sample separation that allows sub-angstrom resolution in the vertical direction (commonly referred to as the z direction) and angstrom resolution in the lateral, or x and y, directions.

Imaging of Surfaces

Most scanning tunneling microscopes share the same essential technologies for maintaining the tunnel gap and monitoring the tunneling current, as shown in Figure 2. Generally, the tip is attached to a piezoelectric material (which changes its dimensions by a few angstroms as the voltage across it is changed), a bias voltage is applied across the tip and the sample, and the tip is rastered across the sample surface while the tunneling current is monitored. Feedback electronics change the voltage across the piezo in response to changes in the tunneling current in order to maintain the tunnel gap. A plot of changes in the z piezo voltage (or changes in the tunneling current) versus the lateral scanning voltages reveals a three dimensional image of the electronic topography of the surface.

There are two basic ways of operating an STM to obtain atomic resolution images. In the first method, called the constant current mode, the piezo voltage is changed to move the tip such that a constant average current (generally on the order of nanoamps) is maintained. The second mode is known as the constant height mode; the feedback response is damped such that the tip maintains a constant average height above the surface. Generally, constant current imaging involves very slow scan rates and yields true topographic images of a surface. Constant height mode

requires much faster scan rates in order to override the feedback electronics and has the potential for imaging real time events.

It is important to note that the STM essentially images electronic densities of states; thus, the current is dependent on the density of states at the Fermi level as well as on the tip-sample separation. Consequently, an atom that lies slightly below the surface but is part of an electronic band which is particularly rich in electronic density might be imaged preferentially to the top lying atoms. If both the first and second layers of atoms share the same lattice spacing and symmetry, one cannot tell which layer or set of atoms is being imaged, as in the case of many metal chalcogenides.[16] In addition, calculations by Lang indicate that in some cases, such as a helium atom adsorbed on a jellium surface, an adsorbate could produce decreased, rather than increased, current.[17] Consequently, the question always remains of whether a feature that appears topographically prominent is actually higher in electron density than the other surface atoms and lies at or below the top layer of atoms rather than resting on top of them.

The different environments in which one is operating an STM places different requirements on the system. In particular, tunneling in polar solvents, particularly water, places strong demands on the system. The tip-sample combination is essentially a two electrode arrangement, and the presence of any dissolved metal ions or other redox active species can result in large Faradaic currents which can swamp out tunneling currents. Faradaic currents can be suppressed by operating in extremely pure solvents or using bias voltages at which no Faradaic current flows. Since Faradaic current is proportional to the exposed area of the electrodes involved in the redox reaction, partially insulating the tip such that only a few square nanometers are exposed also suppresses the Faradaic current below the level of the tunneling current. The last method is the most versatile, and much study has gone into finding suitable coating materials.[18]

Images can also depend on both the magnitude and sign of the bias voltage. For example, in a study by Kato and Osaka,[19] corrugation amplitude in images of semi-conducting quantum wells showed a strong dependence on bias magnitude. Parkinson, Ren, and Whangbo obtained

distinctly different images of a $ReSe_2$ surface at positive and negative biases.[20] They attributed the different images to different layers of the compound which composed different electronic bands and were accessed at different bias voltages. Changing the bias voltage magnitude and sign can supply information about the topographical and electronic structure of a surface.

Scanning Tunneling Spectroscopy

The same technology that allows atomic resolution images to be obtained also enables highly localized electronic measurements to be made. Such measurements are generally referred to as scanning tunneling spectroscopy. There are two forms of scanning tunneling spectroscopy, and each probes different electronic aspects of the tip-sample interaction. In the first type, the width of the tunnel gap is held constant while the bias voltage is swept and the current is monitored. This probes the local density of states around the Fermi level of the sample (assuming that the density of states in the tip remains constant).

Current versus bias voltage spectroscopy can provide interesting clues about the electronic structure of a substrate or adsorbate on a substrate. For example, a report by Feenstra, Thompson, and Fein includes current-voltage curves of semi-conductors showing a zero-current region relating to the band-gap.[21] Parkinson, Ren, and Whangbo saw similar behaviour for $ReSe_2$.[20] Studies by Baker, Rossman, and Baldeschwieler on such exotic materials as boron-doped diamond showed the phenomenon of Fermi-level pinning.[22] It is also possible that current-voltage curves of adsorbates on surfaces could show fine structure in the electronic bands of the adsorbate.

The second type of spectroscopy involves probing the effective barrier height. To do this, the bias voltage is held constant and the barrier width is modulated while the response in the tunneling current is monitored. Modulation of the gap can be done in two ways: the tip is retracted from the surface (or extended toward it), or a small amplitude sinusoidal voltage is applied to the z piezo voltage, causing sinusoidal modulations in the gap width on the order of 0.1 Å. A detailed discussion of barrier heights and barrier height measurements is presented in

Chapter 2. Such spectroscopy has also been used to obtain images of adsorbates or islands, since such features generally have a different barrier height than the substrate.[23]

Summary

Scanning tunneling microscopy and its related techniques provide powerful tools for making high resolution measurements of surfaces and surface processes. With appropriate modifications, STM can be used in a variety of media, enabling researchers to obtain *in situ* images of surfaces that cannot be obtained by any other means. In addition, STM related technology can be used to make highly localized electronic measurements of surfaces, adsorbates, and solutions. Of particular interest to this thesis is the use of STM to investigate the effect of solvents on the effective barrier height.

Organization of the Thesis

This thesis is mainly concerned with investigations of how solvent molecules in the tunnel gap influence effective barrier heights and is divided into four chapters, two of which have appendices. The first chapter is this introduction, which provides an overview of the principles of STM and some of the studies that have been done. The second chapter involves a detailed discussion of STM barrier heights and barrier height measurements in various ambients. The third chapter and its appendix provide a detailed description of the STM used in this experiment, including detailed circuit diagrams. The fourth chapter addresses the barrier height measurements themselves, detailing the experimental method and discussing the results. The appendix that goes with the final chapter details the preparation and characterization of the surface used in the experiment.

References

(1) Binnig, G.; Rohrer, H.; Gerber, Ch.; Weibel, E. *Phys. Rev. Lett.* **1983**, *50*, 120-123.

(2) Binnig, G.; Rohrer, H.; Gerber, Ch.; Weibel, E. *Appl. Phys. Lett.* **1982**, *40*, 178-180.

(3) Examples include: Berndt, R.; Gimzewski, J.K.; Schlittler, R.R. *Surf. Sci.* **1994**, *310*, 85-88. Boland, J.J. *Adv. Physics* **1993**, *42*, 129-171. Baker, S.M.; Rossman, G.R.; Baldeschwieler, J.D. *J. Appl. Phys.* **1993**, *74*, 4015-4019. Land, T.A.; Michely, T.; Behm, R.J.; Hemminger, J.C.; Cosma, G. *J. Chem. Phys.* **1992**, *97*, 6774-6783. Villegas, I.; Stickney, J.L. *J. Vac. Sci. A* **1992**, *10*, 3032-3038.

(4) Examples include: Lercel, M.J.; Redinbo, G.F.; Craighead, H.G.; Sheen, C.W.; Allara, D.L. *Appl. Phys. Lett.* **1994**, *65*, 974-976. Delawski, E.; Parkinson, B.A. *J. Am. Chem. Soc.* **1992**, *114*, 1661-1667. Colton, R.J.; Baker, S.M.; Driscoll, R.J.; Youngquist, M.G.; Baldeschwieler, J.D.; Kaiser, W.J. *J. Vac. Sci. A* **1988**, *6*, 349-353.

(5) Examples include: Schneir, J.; Sonnenfeld, R.; Mart, O.; Hansma, P.K.; Demuth, J.E.; Hamers, R.J. *Appl. Phys. Lett.* **1988**, *63*, 717-721. Schneir, J.; Hansma, P.K. *Langmuir* **1987**, *3*, 1025-1027. Giambattista, B.; McNairy, W.W.; Slough, C.G.; Johnson, A.; Bell, L.D.; Coleman, R.V.; Schneir, J.; Sonnenfeld, R.; Drake, B.; Hansma, R.K. *Proc. Nat. Acad. Sci. U.S.A.* **1987**, *84*, 4671-4674.

(6) Examples include: Song, J.P.; Mørch, K.A.; Carneiro, K.; Thölén, A.R. *Surf. Sci.* **1993**, *296*, 299-309. Penner, R.M.; Heben, M.J.; Lewis, N.S.; Quate, C.F. *Appl. Phys. Lett.* **1991**, *58*, 1389-1391.

(7) Examples include: Shohat, I.; Mandler, D. *J. Electrochem. Soc.* **1994**, *141*, 995-999. Heben, M.J.; Penner, R.M.; Lewis, N.S.; Dovek, M.M.; Quate, C.F. *Appl. Phys. Lett.* **1989**, *54*, 1421-1423. Sonnenfeld, R.; Schneir, J.; Drake, B.; Hansma, P.K.; Aspnes, D.E. **1987**, *50*, 1742-1744. Sonnenfeld, R.; Hansma, P.K. *Science* **1986**, *232*, 211-213.

(8) Examples include: Allison, D.P.; Thundat, T.; Jacobson, K.B.; Bottomley, L.A.; Warmack, R.J. *J. Vac. Sci. Technol. A* **1993**, *11*, 816-819. Häussling, L.; Bruno, M.; Ringsdorf, H.; Rohrer, H. *Angew. Chem. Int. Ed. Engl.* **1991**, *5*, 569-572. Driscoll, R.J.; Youngquist, M.G., Baldeschwieler, J.D. *Nature* **1990**, *346*, 294-296. Dahn, D.C.; Watanabe, M.O.; Blackford, B.L.; Jericho, M.H.; Beveridge, T.J. *J. Vac. Sci. Technol. A* **1988**, *6*, 548-552. Baro, A.M.; Miranda, R.; Alamen, J.; Garcia, N.; Binnig, G.; Rohrer, H.; Gerber, Ch.; Carroscosa, J.L. *Nature* **1985**, *315*, 253-254.

(9) Examples include: Allen, M.J.; Balooch, M.; Subbiah, S.; Tench, R.J.; Siekhaus, W.; Balhorn, R. *Scanning Microsc.* **1991**, *5*, 625-630. Rabe, J.P.; Buchholz, S. *Science* **1991**, *253*, 424-427. McGonigal, G.C.; Bernhardt, R.H.; Thomson, D.J. *Appl. Phys. Lett.* **1990**, *57*, 28-30.

(10) Sasaki, A.; Iwata, F.; Katsumata, A.; Fukaya, J.; Aoyama, H.; Akiyama, T.; Nakano, Y.; Fujiyasu, H. *Jpn. J. Appl. Phys.* **1993**, *32*, 2952-2957. Bourdieu, L.; Silberzan, P.; Chatenay, D. *Phys. Rev. Lett.* **1991**, *67*, 2029-2032. Fuchs, H. *Phys. Scripta* **1988**, *38*, 264-268. Smith, D.P.E.; Bryant, A.; Quate, C.F.; Rabe, J.P.; Gerber, Ch.; Swalen, J.D. *Proc. Natl. Acad. Sci. U.S.A.* **1987**, *84*, 969-972.

(11) Examples include: Li, W.; Virtanen, J.A.; Penner, R.M. *J. Phys. Chem.* **1994**, *98*, 11751-11755. Kim, Y.T.; McCarley, R.L.; Bard, A.J. *J. Phys. Chem.* **1992**, *96*, 7416-7421. Widrig, C.A.; Alves, C.A.; Porter, M.D. *J. Am. Chem. Soc.* **1991**, *113*, 2805-2810.

(12) Binnig, G.; Quate, C.F.; Gerber, C. *Phys. Rev. Lett.* **1986**, *56*, 930-933.

(13) Liu, H.Y.; Fan, F.R.F.; Lin, C.W.; Bard, A.J. *J. Am. Chem. Soc.* **1986**, *108*, 3838-3839.

(14) Betzig, E.; Lewis, A.; Harooticnian, A.; Isaacson, M.; Kratschner, E. *Biophys. J.* **1986**, *49*, 269-279.

(15) Hansma, P.K.; Tersoff, J. *J. Appl. Phys.* **1987**, *61*, R21-R23.

(16) Parkinson, B.A. *J. Am. Chem. Soc.* **1990**, *112*, 1030-1033. Tang, S.L.; Kasowski, R.V.; Parkinson, B.A. *Phys. Rev. B* **1989**, *39*, 9987-9991. Weimer, M.; Kramar, J.; Bai, C.; Baldeschweiler, J.D. *Phys. Rev. B* **1988**, *37*, 4292-4295.

(17) Lang, N.D. *Comments Cond. Mat. Phys.* **1989**, *14*, 253-275.

(18) Bach, C.E.; Nichols, R.J.; Beckmann, W.; Meyer, H.; Schulte, A.; Besenhard, J.O.; Jannakoudakis, P.D. *J. Electrochem. Soc.* **1993**, *140*, 1281-1284. Mao, B.W.; Ye, J.H.; Zhuo, X.D.; Mu, J.Q.; Fen, Z.D.; Tian, Z.W. *Ultramicrosc.* **1992**, *42*, 464-467. Penner, R.M.; Heben, M.J.; Lewis, N.S. *Anal. Chem.* **1989**, *61*, 1630-1636. Nagahara, L.A.; Thundat, T.; Lindsay, S.M. *Rev. Sci. Instrum.* **1989**, *60*, 3128-3130.

(19) Kato, T.; Osaka, F. *J. Appl. Phys.* **1992**, *72*, 5716-5720.

(20) Parkinson, B.A.; Ren, J.; Whangbo, M.-H. *J. Am. Chem. Soc.* **1991**, *113*, 7833-7837.

(21) Feenstra, R.M.; Thompson, W.A.; Fein, A.P. *Phys. Rev. Lett.* **1986**, *56*, 608-611.

(22) Baker, S.M.; Rossman, G.R.; Baldeschwieler, J.D. *J. Appl. Phys.* **1993**, *74*, 4015-4019.

(23) Song, J.P.; Mørch, K.A.; Carneiro, K.; Thölén, A.R. *J. Vac. Sci. Technol. B* **1994**, *12*, 2237-2242. Youngquist, M.G.; Driscoll, R.J.; Coley, T.R.; Goddard, W.A.; Baldeschwieler, J.D. *J. Vac. Sci.Technol. B* **1991**, *9*, 1304-1308.

Figure 1:
A graphic depiction of the phenomenon of electron tunneling as utilized in scanning tunneling microscopy. E_F indicates Fermi level energy for a given material, and ϕ is the work function. The effective barrier height for an ideal system is estimated to be the average of the work functions of the tip and the sample.

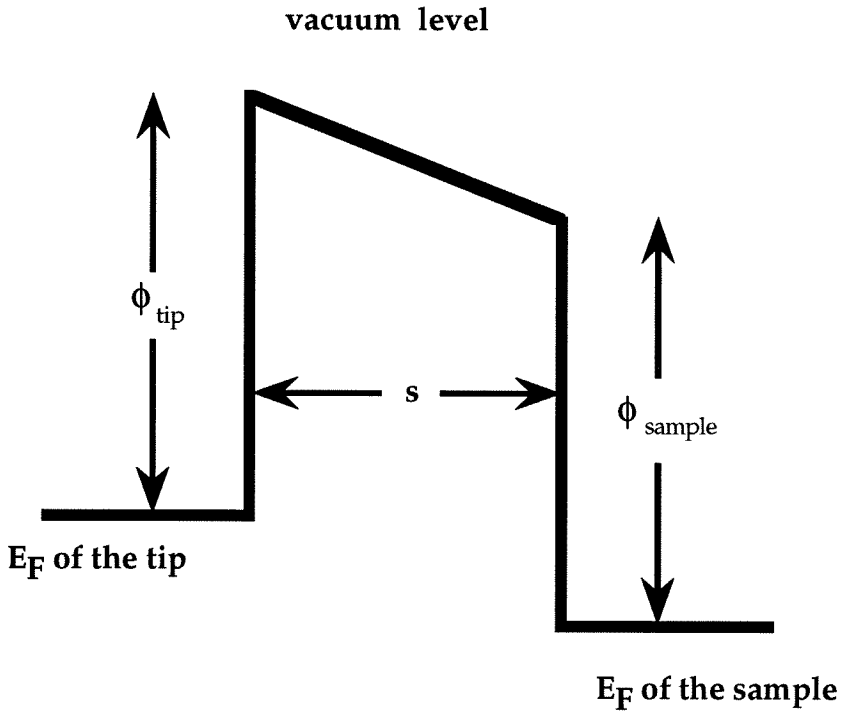
vacuum level
ϕ_{tip}
s
ϕ_{sample}
E_F of the tip
E_F of the sample

Figure 2:
Schematic of a typical STM experiment (not to scale). An adjustable bias voltage is applied across the tip and bulk of the sample. The feedback electronics monitor the tunneling current and make the appropriate adjustments to the z piezo voltage, as well as generating the x and y scanning voltages. The piezo depicted here is tubular; the same principles apply to separate x, y, and z piezoelectric materials. The dotted trace represents the path the tip would follow in the constant current mode of STM; it could also represent the current fluctuations in constant height mode imaging. The trace dips down over the missing surface atom; a dip would also appear over an atom with lower electron density than its neighbors.

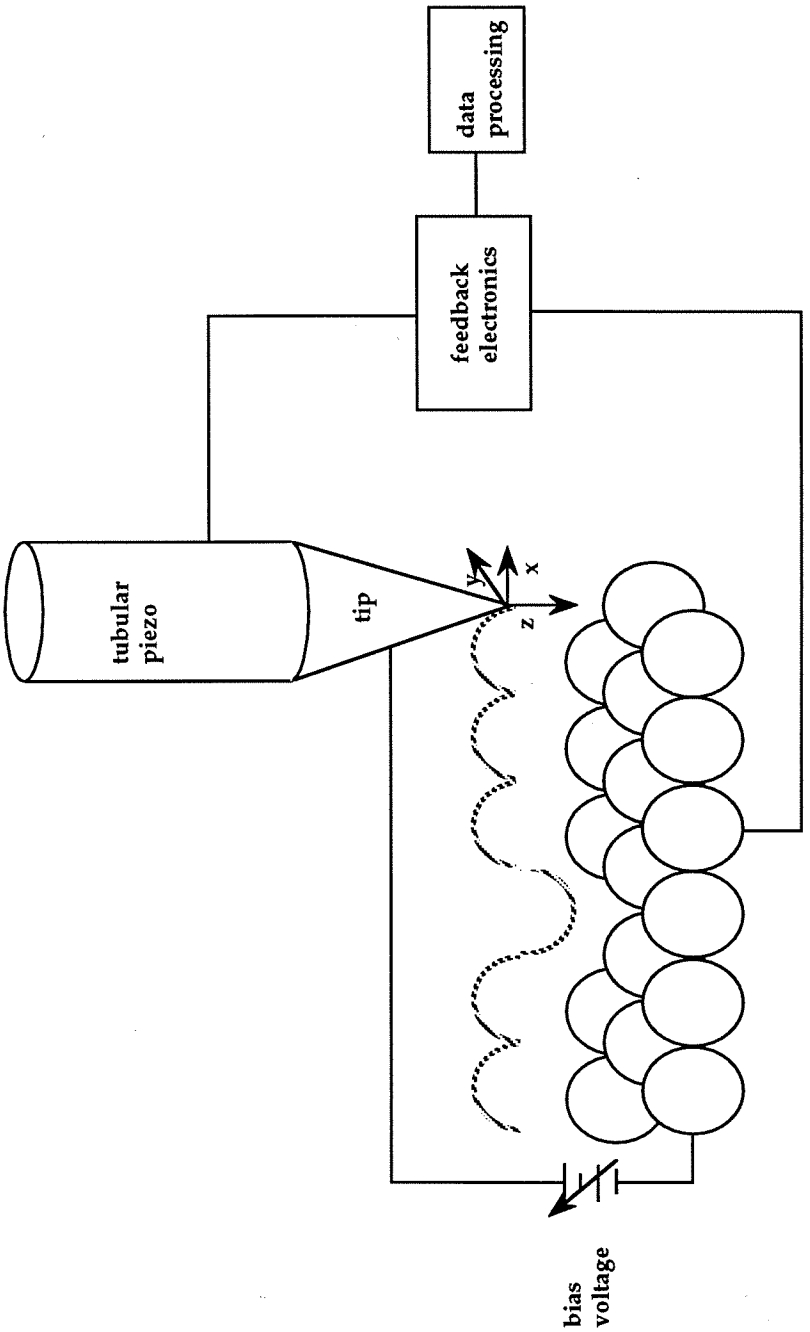
data processing
feedback electronics
tubular piezo
tip
y
x
z
bias voltage

Chapter 2:
Barrier Heights in STM,
Theory and Measurements

Introduction

The theory for electron tunneling is reasonably well developed and understood for simple one dimensional tunneling through a vacuum between two conductors.[1] Theory has also been developed for three dimensional tunneling, as occurs in scanning tunneling microscopy (STM), detailing the wave functions of the sample and approximating wave functions for the tip.[2] Consequently, it is fairly easy to model and explain clean systems of conductors in ultrahigh vacuum conditions. However, more interesting, realistic, and complicated situations are more difficult to model.

It is abundantly clear that it is possible to obtain molecular (and sometimes atomic) resolution images of organic molecules deposited on conducting substrates, even with film thicknesses of 100 Å or more.[3,4] Various theories have been put forth which attempt to explain how such molecules, which are generally insulators, can support tunneling current and how they interact with the wavefunctions of the tip and surface.[5] In addition, the theory for non-vacuum type tunnel gaps (i.e., where there is a solvent in the gap) has been developed at a very qualitative level. One of the most important factors in tunneling that these theories describe is the effective barrier height. Unfortunately, any actual experiments that would provide information purely about adsorbates or solvents are complicated by contaminants on the sample surface and on the tip. Such contaminants are difficult to define and consequently almost impossible to treat theoretically.

Understanding the role of molecules in the tunnel gap has ramifications outside of STM. Solvent in the tunnel gap can be thought of as a model for the Helmholtz layer in cases of heterogeneous electron transfer, where electrons make their way through layers of solvent and electrolyte between an electrode surface and redox molecules. Tunneling through organic adsorbates and solvent molecules is also analogous to long range electron transfer through proteins and DNA. Thus, identifying and understanding the role of molecules in the tunnel gap will also shed light on electron mobility in other systems.

In the simplest theory, at low bias voltages and temperatures, the current can be expressed by:[6]

$$i_t \propto V_B \exp(-2\kappa s) \qquad (1)$$

where V_B is the bias voltage, s is the gap width in angstroms, and κ is the decay length of the wavefunctions in the gap. The decay length is related to the effective (or apparent) work function, ϕ_{eff}, by:

$$\kappa = (2m\phi_{eff})^{1/2}/\hbar \qquad (2)$$

where m is the mass of the electron in the gap, generally taken to be the free electron mass. For simple approximations, ϕ_{eff} is taken to be the average of the work functions of the materials forming the tip and the sample, and so it generally should be 4-6 eV. The effective (or apparent) barrier height can be measured by simply monitoring the change in current with change in gap width. The presence of substances such as solvent molecules or contaminants in the tunnel gap are predicted to lower the effective barrier height and reduce the rate at which the current falls off, as shown in the calculated curves depicted in Figure 1. In addition, more detailed theories suggest that the effective barrier height is not merely the average work function, but might also be affected by image forces and other long-range potentials at the surfaces of the tip and sample.

Generally, barrier height measurements are made in one of two ways. In the most direct method, the tip is simply retracted from or extended toward the surface, and the tunneling current is monitored as a function of changing gap width. The slope of a plot of the logarithm of the current versus change in gap width is proportional to the square root of the effective barrier height.

In the second method, a small modulating voltage is applied to the z piezo, causing modulations of the gap width on the order of 0.1 Å. The resulting current modulations are the derivative of the current with respect to changes in s. From equations 1 and 2, it is clear that di_t/ds is given by:[7]

$$di_t/ds = -2i_t(2m/\hbar)^{1/2}(\phi_{eff})^{1/2} \qquad (3)$$

Consequently, a plot of di_t/ds versus i_t yields the effective barrier height. Both methods should give the same effective barrier height for a true vacuum barrier. However, di_t/ds spectra can show unexpected (and unexplained) modulations in the barrier height for highly corrugated surfaces, while simple i_t versus Δs curves yield constant barrier heights for the same surfaces.[7] In addition, the modulations in gap width for di_t/ds experiments are not necessarily large enough to allow solvent molecules into the gap for solution experiments.

Background

The first barrier height measurements were conducted by Binnig *et al.* in the course of their development of an atomic resolution STM.[8] They used a platinum plate for the sample and a sharpened tungsten wire for the tip, and they performed their experiments in a vacuum system with a pressure of ~10^{-6} torr. Before any sort of cleaning of the tip and sample, they found the gap resistance to be weakly dependent on distance and non-exponential. They cleaned their sample and tip by reaching point contact between them, then applying 10 V_{pp} at 10 kHz, which resulted in some form of ultrasonic cleaning. The barrier height stabilized at ~0.6-0.7 eV; with a better vacuum and more cleaning, they obtained a barrier height of 3.2 eV, which was reasonably close to the predicted value of ~5 eV. More importantly for their purposes, the decay in current was exponential with increasing distance, showing true vacuum-type tunneling.

Another example of low effective barrier heights was reported by Mamin *et al.*[9] They found that they could obtain atomic resolution images of graphite (in air) even over progressive tip displacements of as much as 100 Å. While the authors did not report actual barrier height measurements, their observations of long range imaging would translate to effective barrier heights of under a millielectronvolt. They did not observe such results over a heated (and presumably contaminant free) surface under ultrahigh vacuum conditions with a field-emitted tip. The authors suggested a contamination-mediated deformation of the graphite surface where the surface literally followed the tip as the tip was retracted.

This explanation for anomalously low barrier heights was elaborated upon by Coombs and Pethica.[10] They proposed that spring constants could be associated with the tip, tunneling gap, and surface contaminants. If contact is made between the tip and surface contaminants and the tip is subsequently retracted, the "surface spring" stretches more than the "gap spring." While the current still decreases exponentially with apparent gap width, the decay is much less rapid than if the vacuum gap itself were actually increasing. They further went on to suggest that topographical images themselves might be suspect for systems with low apparent barrier heights, since the surface might be "stretching" and distorting the true structure.

Gimzewski, Möller and co-workers carried out measurements of tunneling current versus tunneling gap width in ultrahigh vacuum conditions.[11] They found barrier heights of 3.5-5 eV for a freshly cleaned polycrystalline silver sample with a freshly field emitted tip, attributing barrier heights of less than 3.5 eV to contamination. For their experiments, they started some distance from the surface, held the bias voltage constant, and extended the tip toward the sample until point contact was made. They observed an abrupt increase in the tunneling current when the tip was within 3 Å of the surface, which they ascribed to the onset of metallic conduction due to significant overlap of electron densities at the Fermi level. In addition, the slope of the natural logarithm of the tunneling current was not strictly linear with decreasing tunneling gap; they calculated larger effective barriers at greater gap widths.

Lang carried out calculations using a sodium atom as a model for the tip and a flat, jellium sample to estimate the gap resistance for an experiment such as that carried out by Gimzewski and Möller.[12] He found that the apparent barrier height should actually show a distance dependence at small tip-sample separations. Just before point-contact, the barrier should be close to zero, then gradually increase to the sample work function at a tip-sample separation of ~8 Å, where the barrier then levels off. He compared these results to the data obtained by Gimzewski and Möller and found good agreement. However, his calculations did not take into account or explain any effects due to contamination.

Sasaki *et al.* measured barrier heights over a variety of substrates in air, then measured barrier heights for Langmuir-Blodgett (L-B) films prepared on those same substrates.[4] For both highly oriented pyrolytic graphite (HOPG) and indium tin oxide (ITO), they found average barrier heights of ~0.12 eV, while they found an average barrier height of ~0.6 eV for gold. They evaporated films of stearic acid onto the substrates under conditions such that the films were oriented and averaged ~30 nm in thickness. The films all gave barrier heights of 2 eV, regardless of the substrate on which they were grown. The authors contended that the low barrier heights observed on bare substrates were due to contamination mediated surface deformations; such deformations were not present for the L-B films. They also stated that the oriented films had high electrical conductivity, although they did not describe a mechanism for that conductivity.

Sass and Gimzewski considered the theoretical effects of solvent in the tunnel gap by treating the tunneling phenomenon as an analog to an electron transfer reaction.[13] They suggested that a bulk solvent in the gap would lower the effective barrier as a result of a combination of factors. One such factor is that a bulk solvent has an effective vacuum level lower in energy than that of the true vacuum level. This effective vacuum level is due to an effective conduction band edge resulting from the solvent's rapid ability to reorient dipoles around a charged species--either a redox molecule or a biased STM tip. This rapid reorientation briefly lowers the barrier height, making it energetically more facile for an electron to leave one conductor and tunnel to another.

Another factor Sass and Gimzewski considered was the presence of low lying energy levels in the gap that are electrostatic in nature. Fluctuations of solvent dipoles would be expected to provide fleeting pockets of hydration for excess electrons, forming temporary, microscopic trapping sites. This would provide a favorable electrostatic environment for the electrons, increasing the tunneling probability at a given tip-sample separation. This increased probability translates into a higher current density, which in turn implies a lower effective barrier height. Figure 2 shows a qualitative depiction of these two effects.

There are recent reports about actual measurements of solvent effects on barrier heights. Pan, Jing, and Lindsay measured barrier heights over gold in water and decalin.[14] They used a hermetically sealed electrochemical STM and examined the effect of changing the sample potential and the tunneling bias on the barrier height, as well as examining solvent effects. Although they admitted that their barrier heights at atmospheric pressure were variable and lower than that predicted for purely vacuum tunneling, they still suggested that their average barriers of greater than 1 eV represented vacuum tunneling (i.e., high barrier heights as well as exponential dependence of current on gap width). Most importantly, the authors suggested that the barrier heights measured in solvent were sufficiently different from those measured in air to draw conclusions about solvent effects.

Pan *et al.* reported a lower barrier in the presence of water with added electrolyte than in the presence of pure water (~1 eV vs. 1.8 eV). Decalin gave a barrier height slightly lower than that for pure water and slightly higher than that for water containing electrolyte. They also reported a bias dependence on the barrier height, with the barrier showing an abrupt dip between 0 and 10 mV. The extent of this dip was dependent on the potential of the sample; the dip was more pronounced with the sample held at 0.14 V vs. SCE than with it at 0.34 V vs. SCE. A similar dip was not seen for decalin. They attributed this dip to a realignment of the solvent dipoles with change in bias magnitude and sign. In addition, they added cytosine to the aqueous solution to form an adlayer and found a potential dependent barrier height between 2-3.8 eV, similar to the barrier heights for Langmuir-Blodgett films found by Sasaki *et al.*[4] However, the scatter in the data obtained by Pan *et al.* and their admission that barrier heights can change over time for a given solvent and sample bring into question whether any conclusions can be drawn.

Song *et al.* also measured barrier heights in air and water with platinum tips and gold samples.[15] They described their results as "statistical," with the barrier heights measured for a given set of parameters fluctuating around a central value. They also observed that the standard deviation increased over time, while the average barrier height decreased slightly. They could observe general trends--the average

high barrier heights in air ranged from 0.64-1 eV, while those in water ranged from 0.16-0.25 eV. They also looked at samples consisting of islands of TiN on tungsten with tungsten tips and found reproducibly higher barriers over tungsten sites than over TiN sites. They did not look for any barrier height dependence on the magnitude or sign of the bias.

Various groups have considered the effect of the image potential on the apparent barrier height in an STM experiment. Binnig *et al.* calculated the effect of the image potential on the average barrier height, assuming the average barrier height to be the average of the work function of the tip and sample.[16] They found that the image force should lower the effective barrier height by at least an eV at large gap widths and cause the apparent barrier height to fall off rapidly with decreasing gap width. Consequently, the barrier heights inferred from di_t/ds experiments should always be much lower than the average of the work functions of the tip and sample, and the natural log of the current should not be linear with distance, contrary to what is generally observed experimentally. In addition, the inferred barrier heights should change rapidly as a function of gap width. They modified this prediction with further calculations for the tunneling current that indicate that the various distance dependent factors cancel for the current, yielding linear slopes of $\ln i_t$ versus distance.

Conversely, Coombs *et al.* carried out calculations suggesting that the image potential should play a negligible role in the barrier height as well as the current.[17] They used a different approximation for the image potential to obtain an analytic solution for $d\ln i_t/ds$, which yields the effective barrier height. In their solution, the image reduced effective barrier height is close to the average work function and nearly constant for gap widths of 3-20 Å (the expected gap width for most tunneling experiments). In their model, the various distance dependent factors in the expression for the barrier height nearly cancel, producing small distance dependent perturbations on the work function.

There are other theoretical and experimental arguments that the barrier height itself should be dependent on the distance between the tip and sample even in the absence of image potentials.[11,12] Exchange correlation effects and induced coulombic effects cause the electron density at the surface (and hence the effective barrier height) to decay more slowly

into the vacuum than would be expected from a simple square well approximation. In fact, the barrier is predicted to decay nearly to zero near point-contact distances. The effect should be most pronounced at very small gap widths ranging from 3 Å to point-contact, with the effective barrier height approaching the work function at a tip-sample separation of about 5 Å. In this case, as well as in the case of the image potential, perturbations of the barrier height with distance are expected to be small in the gap width range of most STM experiments.

Discussion

As can be seen from the background, there are a variety of results and theories about apparent barrier heights measured in a variety of environments. The theoretical factors that have been proposed which could affect the apparent barrier height are the image potential, a dependence of the barrier height on the gap width, the presence of solvent in the gap, and contaminants on the tip and surface. This thesis is mainly concerned with measuring the effects of solvent in the gap on the barrier height, and it is necessary to understand the other factors in order to isolate solvent effects.

The main experimental concerns raised by theoretical considerations such as the image potential is whether the barrier height should vary significantly with gap width, and how the tunneling current should fall off as a function of gap width. If the barrier height is intrinsically strongly dependent on the gap width, it would be very difficult to extract information about how adsorbates or solvents modify the barrier height as inferred from current versus gap width measurements. What is generally observed experimentally is that the logarithm of the tunneling current is linearly dependent on the gap width, as predicted from simple tunneling theory. This would imply that the effective barrier height for most systems has a weak (if any) dependence on the gap width, in accordance with the predictions of Coombs *et al.*[17] In turn, this suggests that the image potential plays a small role in the tunneling process and can be disregarded in considerations of barrier height measurements.

In light of other observations discussed above, simple measurements of barrier heights in air and liquid might be complicated by changes in the barrier height itself with gap width, regardless of the medium or levels of contamination. However, barrier height changes should be most extensive at small tip-sample separations, the upper range being that for normal tunneling. Consequently, if measurements are made such that the gap is increased from a starting width of 3-5 Å and then decreased back to the starting point, convolutions of the barrier height with gap width can probably be ignored.

One general experimental trend is that barrier heights for a given substrate are generally lower in air or solution than in clean, ultrahigh vacuum conditions. Since contaminants of various types are known to exist on almost any surface that is not under clean, ultrahigh vacuum conditions, it is plausible to attribute the lowered apparent barrier heights to surface contamination. However, it is still necessary to explain how the contamination affects the barrier height, especially since it seems that ordered organic layers can show relatively high barrier heights. This would imply that it is not merely the presence of an organic layer that causes the low barrier heights, but rather the presence of a disordered overlayer. Any explanations for the effect of contamination on the apparent barrier height must take this factor into account.

It has been proposed that surface contaminants lower the apparent barrier height by mediating an interaction between the tip and surface such that the surface deforms and stretches as the tip moves up and down relative to the surface. This implies a physical effect rather than an electronic one, and consequently one would expect little or no dependence on bias magnitude or sign. Chen and Hamers further suggest that tip-sample interactions can cause deformations and low apparent barrier heights even for clean samples and ultrahigh vacuum conditions.[18]

In some cases, the results obtained in a given experiment can be explained by various models. For example, in the case of Chen and Hamers, barrier heights of 3.5-4.8 eV were observed at large displacement, while the barrier height dropped by an order of magnitude and continued to decrease at small tip-sample separations. Chen and Hamers attributed this phenomenon to tip-sample forces, yet Lang predicted similar behavior

using a density of states model.[12] This suggests that the result could be electronic rather than physical. In addition, the results obtained by Chen and Hamers are very similar to the results obtained by Gimzewski *et al.*[11]

The presence and degree of force interactions is by no means certain, in that high barrier heights are often measured in vacuum. In addition, Meepagala and Real measured tip-sample force gradients during STM operation in air and concluded that they had little effect on lowering apparent barrier heights over gold samples.[19] It is also not clear why organic overlayers such as Langmuir-Blodgett films would not show similar or even more extensive surface deformations. Consequently, while invoking force gradients or surface deformations provides an explanation for low barrier heights, the extent of such effects is still in question.

The degree of the effects of solvent in the tunnel gap is also an interesting question that has yet to be addressed in detail. For most cases of imaging by STM, solvent appears to have little effect on the tunneling current, in that images of a given surface generally appear the same regardless of ambient,[20] except for cases of surface rearrangement or disordering. The simple explanation for this is that the tunnel gap in most STM experiments is sufficiently narrow that solvent molecules are excluded from the gap. In some cases, the presence of water on the surface can appear to amplify the height of features, presumably by adding in a surface force.[21] Such an effect would tend to support the postulation that contaminants affect the apparent barrier height by modulating surface interactions. However, it does not indicate the presence or degree of electronic interaction between the tip, sample, and solvent.

That electrons can travel long distances through different media is well established in electron transfer experiments conducted in media such as proteins[22] and solvent glasses.[23] Electron transfer under such conditions is frequently treated as quantum mechanical tunneling since the adiabatic coupling is very weak. The rate of electron transfer is dependent on both the medium and path between the donor and acceptor molecules.

If one considers such situations as analogs to an STM experiment, one could consider that solvent molecules should couple to the surface

work functions of the tip and sample, providing a bridge for electron tunneling, as suggested by Sass and Gimzewski.[13] Essentially, solvent molecules should extend the overlap of wavefunctions, effectively lowering the barrier height. The polarizability of a solvent should determine its effectiveness as a bridge, since polarizability is a reflection of the degree to which molecular orbitals on a molecule can interact with other wavefunctions. Electron transfer experiments in solvent glasses indicate that electrons can travel further in more polarizable solvents such as 3-methylpentane than in solvents such as water.[23] This would tend to support the simple picture of more polarizable solvents acting as better bridges for tunneling electrons.

Support for these predictions can be found in the work of Pan *et al.*[14] and Song *et al.*[15] Both groups measured lower barrier heights in water over a given substrate than they did over the bare substrate. In addition, Pan *et al.* found a lower barrier in the presence of decalin (which should be highly polarizable) than in the presence of pure water. At the time the work described in this thesis was undertaken, no such results had yet been reported. Even in light of the work done by Pan *et al.* and Song *et al.*, measurements over a contaminant-free surface are still desirable in order to provide unambiguous information about solvent effects on barrier heights. Consequently, the approach taken was to use a surface that would essentially be free of contaminants and adsorbed water to give information about solvents in the gap. Such a surface should give reproducible barrier heights in air, allowing any differences in the barrier in the presence of solvent to be attributed purely to the solvent. In addition, we intended to determine the cleanliness of the surface before and after the barrier height experiments using surface analytic techniques.

Summary

It is clear that there is much to be understood about the phenomenon of electron tunneling. There are both experimental and theoretical disagreements about the effective wavefunction decay lengths for samples and tips composed of clean metals or semiconductors. The concepts of barrier heights and wavefunction overlap rapidly become more complicated in the presence of molecular adsorbates or disordered

molecules in the tunnel gap. While it seems intuitively clear that anything should be more conductive than a vacuum, the extent to which various adsorbates and liquids appear to support current is still a puzzle. It is apparent that the presence of contaminants on the sample or tip can lower the effective barrier in an STM experiment, either through electronic bridging or by mediating surface deformations. In addition, solvent in the gap also appears to lower the effective barrier height.

References

(1) For example, see G. Baym, *Lectures on Quantum Mechanics;* Benjamin Cummings Publishing Co.: Menlo Park, CA, 1973.

(2) Tersoff, J.; Hamann, D.R. *Phys. Rev. Lett.* **1983**, *50*, 1998-2001.

(3) Examples include: Frommer, J. *Angew. Chem. Int. Ed. Engl.* **1992**, *31*, 1298-1328. Li, W.; Virtanen, J.A.; Penner, R.M. *J. Phys. Chem.* **1994**, *98*, 11751-11755.

(4) Sasaki, A.; Iwata, F.; Katsumata, A.; Fukaya, J.; Aoyama, H.; Akiyama, T.; Nakano, Y.; Fujiyasu, H. *Jpn. J. Appl. Phys.* **1993,** *32*, 2952-2957.

(5) Garcia, R.; Garcia, N. *Chem. Phys. Lett.* **1990**, *173*, 44-50. Ou-Yang, H.; Marcus, R.A.; Källebring, B. *J. Chem. Phys.* **1994**,*100*, 7814-7824.

(6) Hansma, P.K.; Tersoff, J. *J. Appl. Phys.* **1987**, *61*, R1-R23.

(7) Schuster, R.; Barth, J.V.; Wintterlin, J.; Behm, R.J.; Ertl, G. *Ultramicroscopy* **1992**, *42-44*, 533-540.

(8) Binnig, G.; Rohrer, H.; Gerber, Ch.; Weibel, E. *Appl. Phys. Lett.* **1982,** *40*, 178-180.

(9) Mamin, H.J.; Ganz, E.; Abraham, D.W.; Thomson, R.E.; Clarke, J. *Phys. Rev. B* **1986,** *34*, 9015-9018.

(10) Coombs, J.H.; Pethica, J.B. *IBM J. Res. Develop.* **1986,** *30*, 455-459.

(11) Gimzewski, J.K.; Möller, R. *Phys. Rev. B* **1987,** *36*, 1284-1287. Gimzewski, J.K.; Möller, R.; Pohl, D.W.; Schlittler, R.R. *Surf. Sci.* **1987**, *189/190*, 15-23.

(12) Lang, N.D. *Phys. Rev. B* **1987,** *36,* 8173-8176. Lang, N.D. *Phys. Rev. B* **1988,** *37,* 10395-10398.

(13) Sass, J.K.; Gimzewski, J.K. *J. Electroanal. Chem.* **1988,** *251,* 241-245. Sass, J.K.; Gimzewski, J.K.; Haiss, W.; Besocke, K.H.; Lackey, D. *J. Phys. Condens. Matter* **1991,** *3,* S121-S126. Sass, J.K.; Gimzewski, J.K. *J. Electroanal. Chem.* **1991,** *308,* 333-337.

(14) Pan, J.; Jing, T.W., Lindsay, S.M. *J. Phys. Chem.* **1994,** *98,* 4205-4208.

(15) Song, J.P.; Mørch, K.A.; Carneiro, K.; Thölén, A.R. *J. Vac. Sci. Technol. B* **1994,** *12,* 2237-2242.

(16) Binnig, G.; Garcia, N.; Rohrer, H.; Soler, J.M.; Flores, F. *Phys. Rev. B* **1984**, *30,* 4816-4818.

(17) Coombs, J.H.; Welland, M.E.; Pethica, J.B. *Surf. Sci.* **1988**, *198,* L353-L358.

(18) Chen, C.J.; Hamers, R.J. *J. Vac. Sci. Technol. B* **1991,** *9,* 503-505.

(19) Meepagala, S.C.; Real, F. *Phys Rev. B* **1994,** *49,* 10761-10763.

(20) Sonnenfeld, R.; Hansma, P.K. *Science,* **1986**, *232,* 211-213. Heben, M.J.; Penner, R.M.; Lewis, N.S.; Dovek, M.M.; Quate, C.F. *Appl. Phys. Lett.* **1989**, *54,* 1421-1423.

(21) Woodward, J.T.; Zasadzinski, J.A. *Langmuir* **1994**, *10,* 1340-1344.

(22) Winkler, J.R.; Gray, H.B. *Chem. Rev.* **1992**, *92,* 369-379.

(23) Miller, J.R. *J. Phys. Chem.* **1972**, *56,* 5173-5183. Miller, J.R.; Beitz, J.V. *J. Chem. Phys.* **1981**, *74,* 6746-6756.

Figure 1:
Calculated curves of i_t vs. Δs for three different effective barrier heights (ϕ_{eff}) according to the equation:

$$i_t \propto V_B \exp(-A\phi_{eff}^{1/2}s)$$

where V_B is the bias voltage, $A=(4\pi/h)(2m)^{1/2}$, m is the mass of the electron in the gap, and s is the gap width in angstroms. If m is equal to the free electron mass, $A=1.025\ eV^{-1/2}Å^{-1}$. As the barrier height decreases, the current falls off more weakly as a function of increasing gap width.

Current vs. Δs for different effective barrier heights

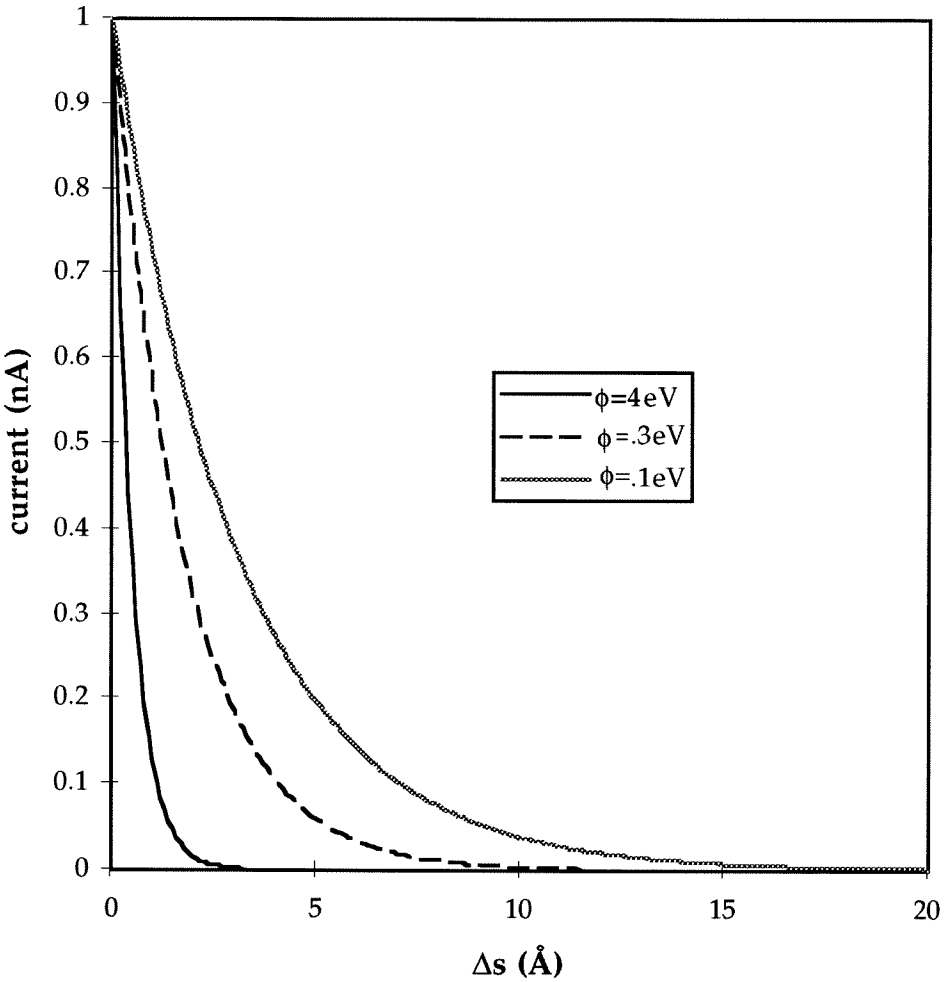

Figure 2:
Schematic depictions of the barrier for a vacuum gap (upper figure) and the barrier for a gap with water molecules (lower figure). The effective conduction band of the water lowers the effective vacuum level and the effective barrier height. In addition, the water molecules can provide temporary microscopic trapping sites.

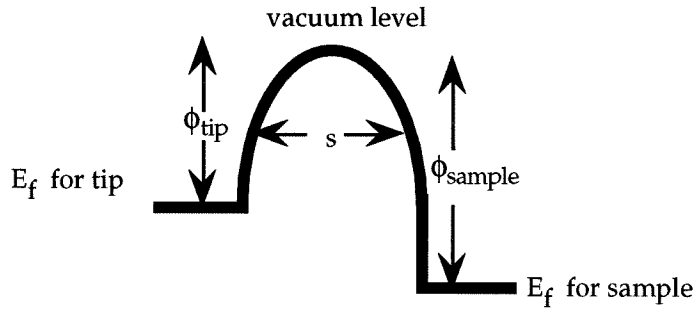

vacuum barrier

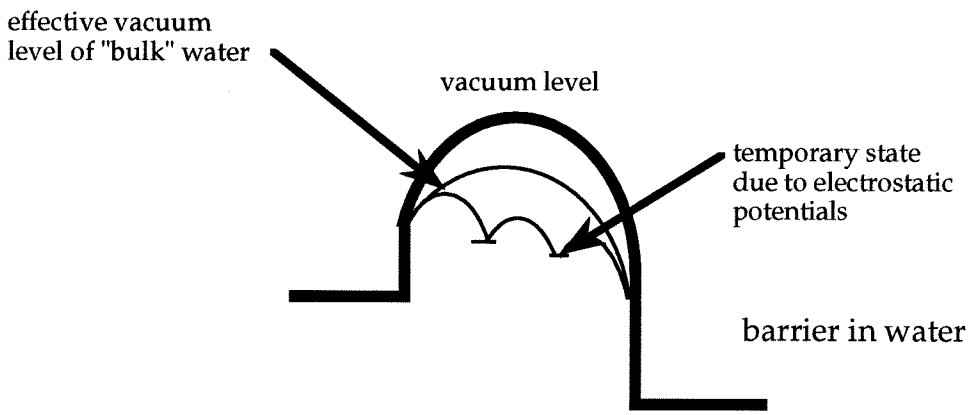

Chapter 3:
Design of an Electrochemistry Compatible STM

Introduction

Scanning tunneling microscopes consist of two major components: the body of the microscope itself and the electronics that monitor and control the microscope. The body generally consists of a scanning head and a sample base. The x, y, and z piezos and the tip are mounted on the scanning head; there is also generally some mechanism to allow for coarse approach of the tip to the sample. The sample base holds the sample in place and makes electrical contact to it. Forms of vibration and thermal isolation can also be considered part of the body of the microscope.

The electronics generally consist of feedback controls and data processing. The feedback circuitry monitors the tunneling current as a function of tip position and adjusts the z piezo voltage. The data processing records either fluctuations in the current or z piezo voltage as a function of x and y piezo positions.

The microscope described in this chapter is an analog system that allows great control by the user. It is designed to function in air or under solution and allows for electrochemical control of both the tip and the sample. Both the body and electronics are based on a design originally developed by Dovek, Heben *et al.*, and detailed discussions of the original system appear elsewhere.[1,2] Consequently, this chapter will focus on aspects peculiar to the system and central to the main experiment of this thesis.

Microscope Body

Scanning Head

The STM head consists of approach mechanics and a tubular piezo, as shown in Figure 1. The approach mechanics involve a stepper motor that is mounted on a steel plate and drives a screw pressing against another steel plate. The lower plate is held in tension against the screw by three springs strung between the lower and upper plates. The travel of the lower plate is guided by three steel rods that fit into divots in the quartz base. The stepper motor can be driven by either an adjustable DC voltage in the manual mode for coarse approach or by voltage pulses generated by the approach pulse circuit in the automatic mode. As the screw extends, the lower plate moves along the steel rods.

Once coarse approach is achieved, the approach system is switched to the automatic mode and voltage pulses that are 12 ms in width and of adjustable height (generally 4-8 V) are sent to the stepper motor in 85 ms intervals. When tunneling current is established, the pulse train is terminated and a +15 V signal is sent to the z piezo amplification circuit, causing the piezo to fully retract. This signal slowly leaks off, allowing the piezo to slowly extend until tunneling current is again established and the feedback circuitry begins controlling the piezo voltage. In addition, a panel switch allows the user to terminate the pulse train at any time.

The tubular piezo, constructed of PZT-5H piezoelectric ceramic, is mounted off-center on a macor base which in turn is mounted to the lower plate with screws. The piezo is held to the macor base with silicone sealant which provides a reasonably stable mount, but allows the piezo to be removed without damaging it. The silicone sealant also provides excellent, inert insulation against most solvents to the piezo and attached wires. The tip is held by a pin holder which is attached to the side of the piezo by silicone sealant. The whole assembly is reasonably rigid, insulated, and the various components can be easily disassembled.

Base and Sample Holders

The main portion of the base is a quartz cup-shaped cell depicted in Figure 1. A hole in the bottom of the cell allows insertion of the sample holder, and a sealed window on the side provides a view of the sample when the base is assembled. Small holes drilled near the bottom of the cell allow for the easy introduction of solution through plastic or Teflon tubing, which is sealed in place with silicone sealant. The cell is mounted to a brass base with nylon screws; the brass lowers the center of gravity of the assembly, increasing its stability. The brass base has a large tapped hole in line with the hole in the quartz cell. The sample holder fits through this hole and is held in place with a Teflon screw.

The sample holders (also shown in Figure 1) consist of quartz cylinders, about 1 cm in diameter, with a broader base. A Teflon o-ring can be placed around the cylinder, providing a water-tight, inert seal when the sample holder is firmly in place. A small hole drilled through the long axis of the cylinder allows wires to pass through the quartz to provide electrical contact to the sample.

Samples can be mounted in two ways. In the first, the contact wires are attached to the back of the sample with silver print. The sample is than cemented to the sample holder with white epoxy. The epoxy serves to hold the sample in place and insulate the edges, back, and wires from contact with solution. In the second mounting system, a metal plate is cemented to the top of the sample holder and the contact wires with silver epoxy. Conducting samples can simply be placed on top of the metal plate and held in place with a Teflon cap with a hole in the center. The Teflon cap insures contact between the sample and metal plate and insulates the metal plate and edges of the sample from solution. Further insulation can be achieved by wrapping the quartz post with Teflon tape.

Control Electronics

The electronics for this system are essentially analog, allowing the user great control over the system. They involve a pre-amplifier, feedback control electronics, a bias supply, x and y scanner drives, and methods for data collection and processing. Since the previous generation of these electronics appear elsewhere,[1] this discussion will focus on the details unique to this system, particularly those developed for and used in the central experiment in this thesis. Detailed schematics for the electronics used in our system appear in the appendix.

Pre-amplifier

The role of the pre-amplifier is to convert the small tunneling current to a voltage that is large enough for the feedback control electronics to monitor and respond to easily. In our system, the pre-amplifiers consist of a current to voltage converter followed by an instrument amplifier with a selectable gain. In the current to voltage converter, the current is dropped across a quiet, high precision 10 MΩ resistor, either in the feedback loop of an op-amp or between the non-inverting input of an op-amp and the bias. That voltage is then boosted by a gain of 1, 10, or 100 by the instrument amplifier. In general, the gain is set such that 1 nA of tunneling current results in an output of 1 V. The whole circuit is enclosed in a small, grounded box that is held to the brass base with Velcro.

Feedback Control Electronics

The feedback control electronics monitor the output of the pre-amplifier, compare it to the setpoint current, and make adjustments to the voltage applied to the z piezo to maintain that current. The setpoint is actually the output of a voltage regulator and can be controlled by the user. The difference between this setpoint voltage and the absolute value of the output of the pre-amplifier can be boosted by integral and proportional gain circuits. The boosted signal is then passed through a low pass filter with an adjustable RC-time constant to damp the response time of the feedback signal. Finally, this signal is amplified by a factor of 20 and applied to the z piezo.

The presence of the adjustable time constant allows the microscope to be operated in either constant current or constant height mode. For constant height mode, the slow time constant is chosen. This filter consists of a 100 μF capacitor and a 10 kΩ potentiometer and damps the response of the feedback circuit such that the z piezo voltage changes very little. For constant current mode, either an 8 μF or 10 nF capacitor is selected for the damping circuit, allowing the electronics to respond rapidly to small changes in the tunneling current. Changes in the z piezo voltage are monitored by an offset circuit, described below.

Sample and Hold Circuit

A slow memory sample and hold circuit enables the measurement of small changes in the z piezo voltage as well as permitting the temporary disablement of active feedback while maintaining control over the z piezo. The ultimate input to the sample and hold circuit is the voltage being sent to the final high voltage op-amp that drives the z piezo. Since this voltage is 1/20 of the voltage actually being applied to the z piezo, it will be referred to as $Z_{out}/20$. This voltage is continuously monitored, divided by a factor of ten, and applied to the input of a 12-bit analog-to-digital converter with a built in sample and hold and a range of +3 V to -3 V. When the analog-to-digital converter is triggered, conversion is complete within 40 μs, and the digital output remains constant until conversion is again initiated. The digital output is continuously converted to an analog voltage by a digital-to-analog converter with a range of +5 V to -5 V. The output is then readjusted to the initial value of $Z_{out}/20$ through a voltage

amplifier involving a potentiometer. Thus, the output voltage can be adjusted by the user.

This circuit has several advantages over a standard sample and hold circuit. The primary advantage is that there is no droop in the output voltage. Most sample and hold circuits begin to drift by tens of millivolts per second within a few microseconds of being triggered. Since the output of the sample and hold circuit is multiplied by a factor of 20 before being applied to the z piezo, such a droop would translate to hundreds of millivolts per second, which in turn means a drift of several angstroms per second. Such a drift would make both monitoring and controlling the voltage difficult. Since the output of the analog to digital converter is stable until conversion is initiated, there is no drift in the z voltage when the sample and hold output is enabled.

The second advantage is that the actual output of the sample and hold circuit can be adjusted by the user. This is actually a necessity, since the analog-to-digital converter is very sensitive to any ring in its triggering signal and has a tendency to make conversion errors. The user can compensate for these errors, adjust for thermal drift, or adjust the tunnel gap for a desired tunneling current.

Offset Circuit

Monitoring a change in the z piezo voltage relating to a change of a few angstroms in the tunneling gap involves detecting a change of a few hundred millivolts (with millivolt precision) in a voltage ranging from -100 V to +100 V. This is accomplished with an offset circuit based on a differential amplifier. One input to the amplifier is $Z_{out}/20$. The other input is the output of the sample and hold circuit described in the previous section. The difference between these inputs is then amplified by a gain of 1, 2, 20, or 40. The gain of twenty is equivalent to the change in the actual z piezo voltage. Since the offset circuit takes the difference between the sample and hold output voltage and $Z_{out}/20$, it is automatically zeroed upon switching from active feedback to the sample and hold output.

Bias Supply

The bias supply consists of an adjustable voltage supply with two ranges. The large range is from +15 V to -15 V with fine adjust on the

configuration of the body of the microscope provides for easy change of the tip, sample, and solution. In addition, the inertness of the materials used in its construction make it possible to establish and maintain tunneling current in air, non-polar solvents, polar solvents, and in solutions containing relatively high concentrations of electrolytes. The configuration of the electronics allows imaging in either constant current or constant height mode as well as allowing the carrying out of spectroscopic measurements.

The establishment of tunneling current is facilitated by an approach system based on a stepper motor that can be operated in both a manual and automatic mode, as described above. The user can easily bring the tip within tens of microns of the sample surface by applying an adjustable DC voltage to the stepper motor while viewing the sample surface through a microscope aimed through the window set into the sample cell. The stepper motor control is then switched to the automatic mode, and a pulse train drives the stepper motor until tunneling current is sensed. At that point, the pulse train is terminated, and the piezo is retracted and allowed to relax into tunneling range.

The pulse height and number of pulses necessary to bring the tip within tunneling range of the sample varies depending on various factors. One factor is the tautness of the springs holding the lower, moving plate in tension against the stepper motor screw. In general, the more "sprung" the springs, the larger the pulse height needed to overcome inertia and the spring constant. Another factor, of course, is the initial distance between the tip and sample when the pulse train is initiated. In general, with patience on the part of the user, the tip can be brought within tunneling range of the sample without crashing.

Various forms of isolation are needed to isolate the microscope body and electronics from sources of noise in order to establish and maintain steady, quiet tunneling current. Vibration isolation is achieved by placing the assembled microscope body on a gel pad (of ~1 in. thickness) on a section of a sub-basement floor that is physically separate from the rest of the floor and the building. The gel pad rests on a piece of grounded copper mesh, and a steel can covered with acoustic foam is placed over the whole assembly. This arrangement provides both thermal and acoustic

insulation and acts as a reasonable Faraday cage. Both the microscope body and electronics are ultimately grounded to a copper stake driven into the earth.

The choice of tip material is also an important factor in an STM experiment. If the microscope is operated in vacuum, air, or non-polar solvents, a bare piece of cut wire will do. However, a cut wire has an undefined morphology at the tip. It is beneficial to use an electrochemically sharpened tip which can then be partially insulated for use in polar solvents or high concentrations of electrolytes. Good methods for etching, coating, and characterizing tungsten, platinum, and platinum-iridium tips have been developed and described elsewhere.[1,4-6]

Once tunneling current is established, images can be obtained using the image processing method described above. The user can adjust the gain, RC-time constant, and bias to maximize the stability of the tunneling current and z piezo response. In addition, the signal being monitored (i.e., tunneling current or variations in z piezo voltage) frequently requires filtering to remove noise due to coupling to scan voltage, line noise, or an unwanted DC component. The scan window and frequency can also be adjusted by the user over a wide range, essentially limited only by the response ability of the piezo. Generally, thermal drift is less than 5 Å/min. within an hour of establishing tunneling current.

The configuration of the bias supply serves several purposes. The most basic purpose is to provide a quiet, fully adjustable bias voltage between the tip and the sample. The option of pulsing the bias enables the user to carry out lithography, particularly on graphite.[7-10] In addition, applying voltage pulses to the tip has been shown to improve imaging performance, presumably by cleaning adsorbates or oxides from the tip.[11]

The instrument can be used to carry out localized electronic measurements, also called scanning tunneling spectroscopy. All forms of scanning tunneling spectroscopy require that the active feedback be disabled while some form of control over the z piezo is still maintained. This is done by triggering the sample and hold circuit and adjusting its output until the output of the offset circuit is close to zero. The input to the final amplifier for the z piezo voltage is then switched from active feedback to the sample and hold voltage. The user can make small

adjustments in the sample and hold voltage to adjust the position of the z piezo. An overview of this system is shown in Figure 2, and detailed schematics of the individual circuits are given in the appendix to this chapter.

One type of spectroscopy involves probing the local density of states by monitoring the change in tunneling current while sweeping the bias voltage without allowing the tunneling gap to change. A constant tunneling gap is maintained by disabling the active feedback, as described above. The bias can be swept in a controlled fashion using the output of a Princeton Applied Research Corporation (PARC) 175 Universal Programmer rather than the bias circuit output as the bias source.

Another type of spectroscopy, and the one upon which this thesis is based, involves measuring the local barrier height. A detailed overview of theory and measurements of this type is presented in Chapter 2 of this thesis. Measurements of the barrier height are made by monitoring the decay in tunneling current as the tunnel gap is slowly increased. Local barrier heights can also be measured by varying the tunneling gap in a sinusoidal fashion, essentially measuring the derivative of the current with respect to the gap width. While this will give the barrier height at small gap widths, it does not necessarily provide information about the barrier height at larger gap widths or allow solvent molecules into the gap. The presence of solvent molecules in the gap should influence the effective barrier height as discussed in Chapter 2 of this thesis.

The accurate measurement of tunneling current as a function of changing tunneling gap width places certain demands on the electronics. One must be able to control the retraction and extension of the z piezo and measure and record those distance changes. These demands are met by applying an external scanning voltage to the z piezo voltage and monitoring the change in voltage being applied to the z piezo. This voltage change relates directly to a change in length of the z piezo and consequently to the width of the tunneling gap.

Scanning of the z piezo voltage is accomplished by applying an external voltage to the z voltage before final amplification. This can be done while the feedback electronics are active, but the result is noisy and can be non-linear since the feedback circuitry attempts to maintain the

setpoint current. Instead, the active feedback is switched out, and the output from the sample and hold is sent to the final amplifier instead. The signal from a PARC 175 can then be added to the voltage, driving the extension or retraction of the z piezo.

It is important to know the response of the z piezo to changes in the applied voltage. The piezo used in this system was calibrated using interferrometry, and the long-range distance versus voltage curve was fit to a third order polynomial equation to yield an average short-range response of 32 Å/V. The interferrometer used was a Zygo Corporation Model #ZMI100 with an instrument resolution of 12.4 Å and an effective resolution of 50 Å for the set-up. A typical calibration curve is shown in Figure 3.

Summary

This chapter and its appendix give a complete description of a scanning tunneling microscope that can be used in a variety of ambients, including conditions suitable for electrochemistry. The microscope can be used for both constant height and constant current imaging and can also be used for scanning tunneling spectroscopy. The discussion includes materials, noise isolation, and various details that affect the operation of the system.

References

(1) Heben, M. J. Ph.D. Thesis, California Institute of Technology, 1990.

(2) Dovek, M.M.; Heben, M.J.; Lang, C.A.; Lewis, N.S.; Quate, C.F. *Rev. Sci. Instrum.* **1988,** *59,* 2333-2336.

(3) The image processor used can be either an Arlunya TF5000 Series Temporal Filter and Image Store or an Arlunya TF6000 Series Image Processor.

(4) Penner, R.M.; Heben, M.J.; Lewis, N.S. *Anal. Chem.* **1989,** *61,* 1630-1636.

(5) Heben, M.J.; Penner, R.M.; Lewis, N.S. *Appl. Phys. Lett.* **1989,** *54,* 1421-1423.

(6) Penner, R.M.; Heben, M.J.; Longin, T.L.; Lewis, N.S. *Science* **1990**, *250*, 1118-1121.

(7) Albrecht, T.R.; Dovek, M.M.; Kirk, M.D.; Lang, C.A.; Quate, C.F.; Smith, D.P.E. *Appl. Phys. Lett.* **1989**, *55*, 1727-1729.

(8) Penner, R.M.; Heben, M.J.; Lewis, N.S.; Quate, C.F. *Appl. Phys. Lett.* **1991**, *58*, 1389-1391.

(9) Li, W.J.; Virtanen, J.A.; Penner, R.M. *Appl. Phys. Lett.* **1992**, *60*, 1181-1183.

(10) Parkinson, B. *ACS Symp. Series* **1992**, *499*, 76-85.

(11) Gimzewski, J.K.; Moller, R. *Phys. Rev. B* **1987**, *36*, 1284-1287.

Figure 1:
Depiction of the assembled body of the STM. The inset shows the quartz sample holder as mounted into the base. The various important parts are labelled and a complete description can be found in the text. Not shown: a shielded wire is contacted to the back of the sample or sample plate, runs through a hole drilled through the sample holder and Teflon screw, and plugs into the pre-amplifier.

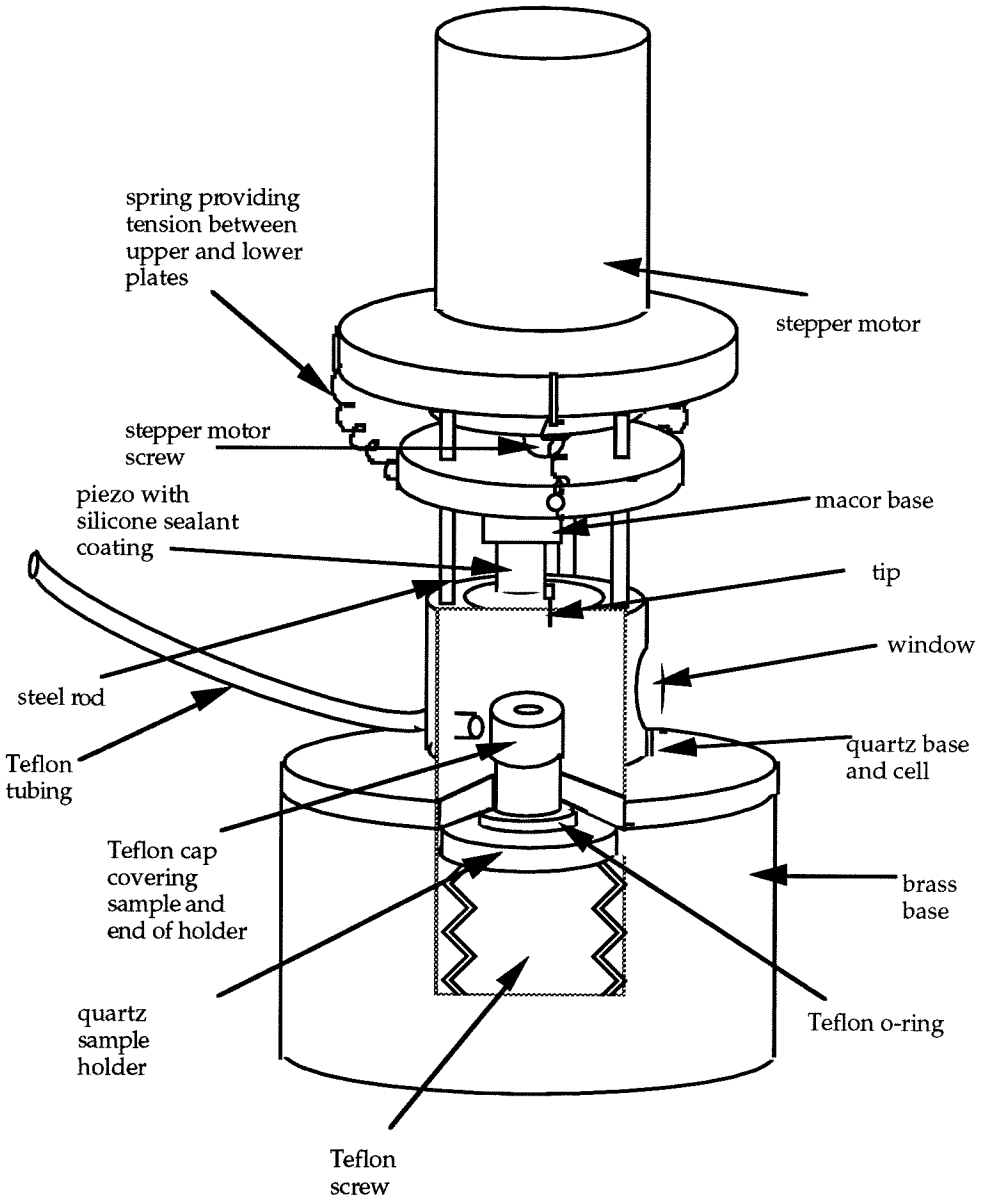
spring providing tension between upper and lower plates
stepper motor
stepper motor screw
piezo with silicone sealant coating
macor base
tip
window
steel rod
Teflon tubing
quartz base and cell
Teflon cap covering sample and end of holder
brass base
quartz sample holder
Teflon o-ring
Teflon screw

Figure 2:
Overview of the circuitry that controls the movement of the z piezo. Detailed schematics of the various portions appear in the appendix. The feedback circuitry monitors the signal from the pre-amplifier, compares it to the setpoint current, and alters the z piezo voltage to try to match the setpoint current within the boundaries set by the adjustable gain and damping filter. The sample and hold circuit enables long interruptions in the active feedback. The offset circuit simplifies the monitoring of small changes in the z piezo voltage.

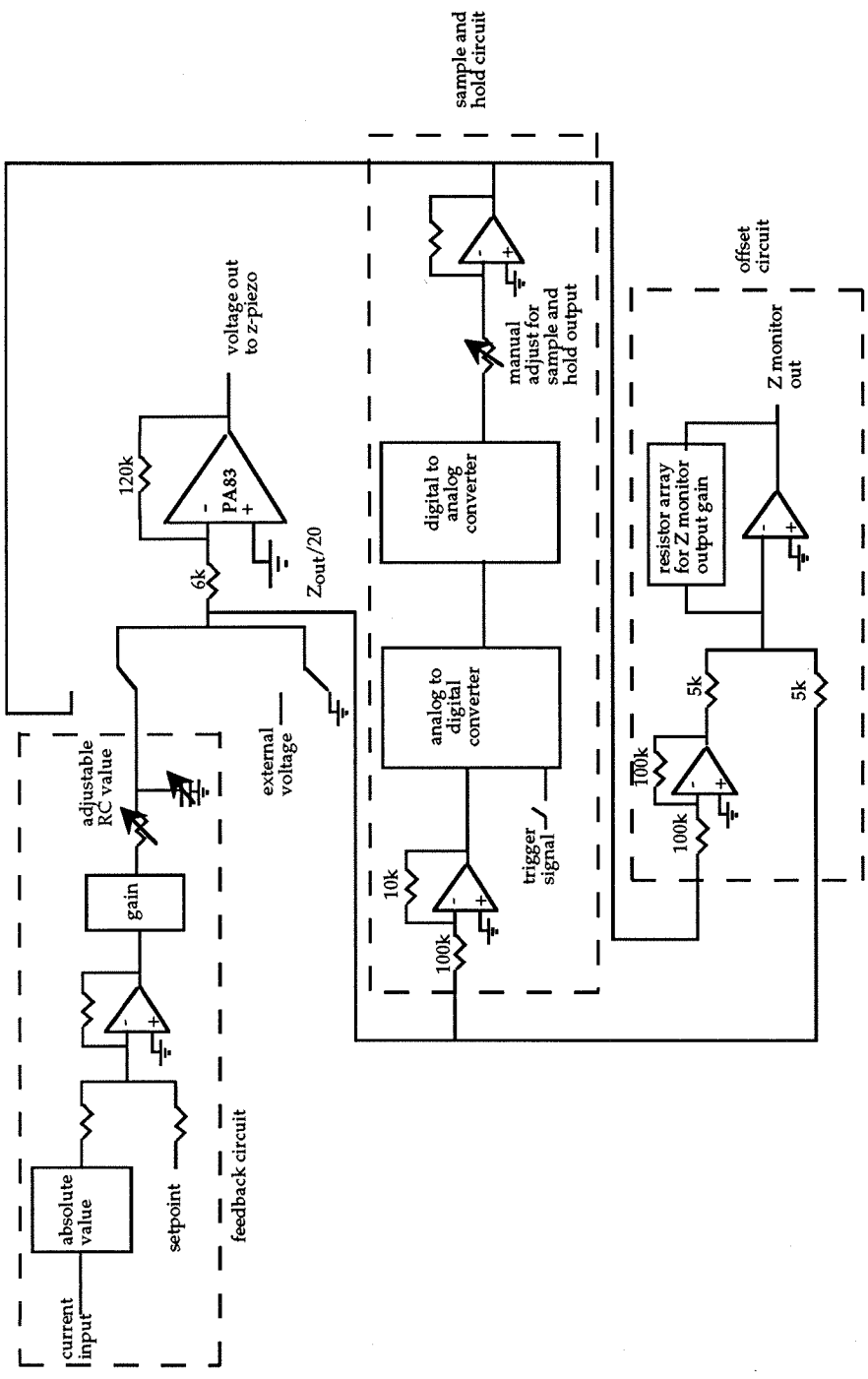
sample and hold circuit
offset circuit
voltage out to z-piezo
120k
PA83
6k
Zout/20
digital to analog converter
manual adjust for sample and hold output
resistor array for Z monitor output gain
Z monitor out
adjustable RC value
external voltage
analog to digital converter
trigger signal
10k
100k
5k
100k
5k
100k
gain
absolute value
current input
setpoint
feedback circuit

Figure 3:
Typical calibration curve for the z piezo response to a change in applied voltage. The open circles indicate data points and the line is the third order polynomial fit to the data. Four different measurements were made; the average response was 32 Å/V.

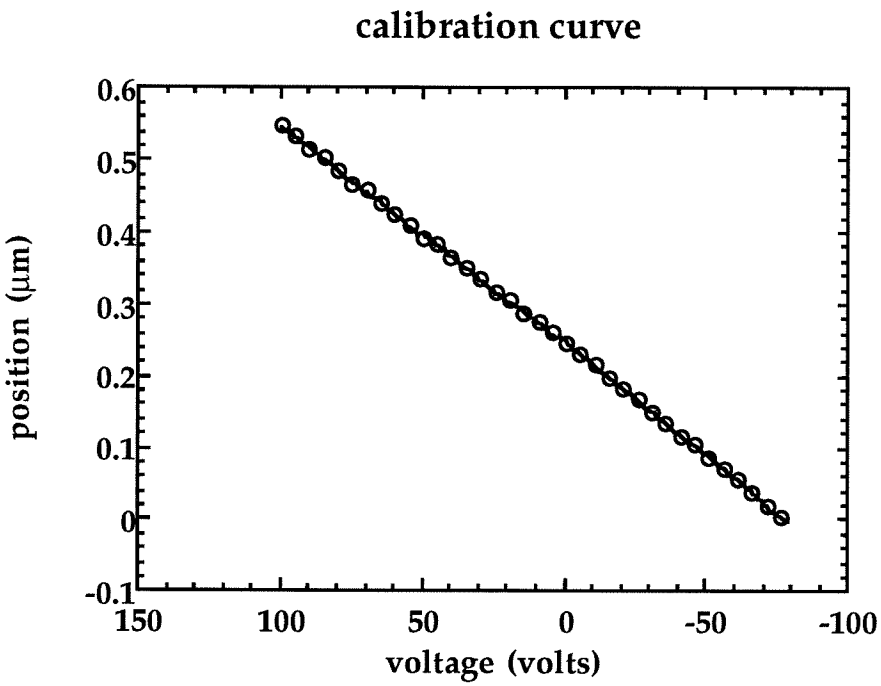
calibration curve
position (μm)
0.6
0.5
0.4
0.3
0.2
0.1
0
-0.1
150
100
50
0
-50
-100
voltage (volts)

Appendix: Circuit Diagrams

This appendix provides detailed schematics and descriptions of the circuitry that comprise the control electronics for the scanning tunneling microscope. Diagrams are provided for the feedback circuit, the sample and hold circuit, the z piezo driver circuit, the offset circuit, the x and y scanner circuit, the approach pulse circuit, and the bias supply circuit.

Figure A1: Feedback Circuit

The feedback circuit takes the absolute value of the current input and compares it to a setpoint value. The difference is amplified by integral and proportional gain circuits and damped by an adjustable time constant.

S1 is a panel switch allowing the integral gain to be turned on and off.

S2 is an internal switch that selects between the positive and negative feedbacks.

S3 is a panel switch that selects for various capacitors in the damping circuit, providing for coarse gains in the RC time constant.

P1 is a panel potentiometer that adjusts the current setpoint.

P2 and **P3** are panel potentiometers that adjust the integral and proportional gains, respectively.

P4 is a panel potentiometer for fine adjust of the RC-time constant.

All op-amps are AD544s or equivalent.

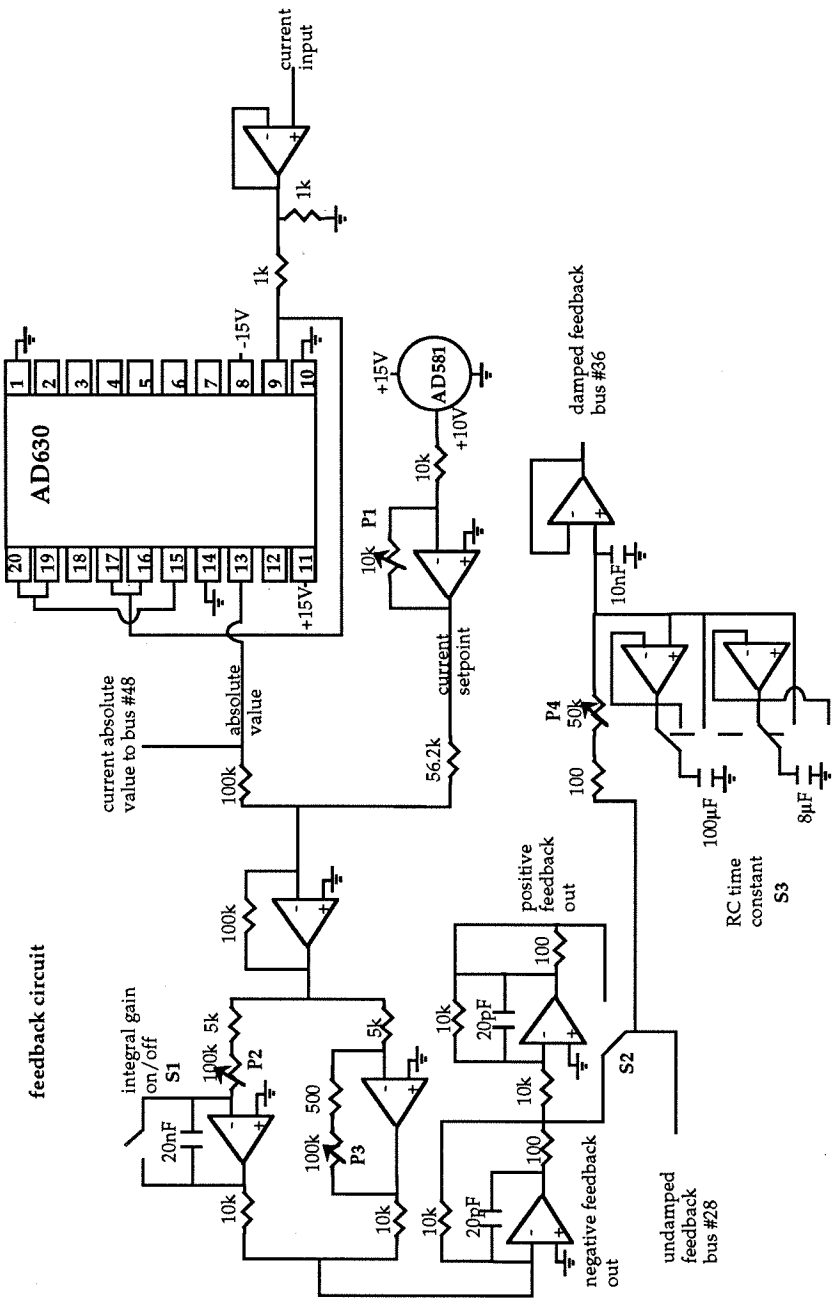
feedback circuit
AD630
AD581
+15V
-15V
+10V
current input
1k
current absolute value to bus #48
absolute value
current setpoint
integral gain on/off
S1
S2
S3
P1
P2
P3
P4
20nF
100k
5k
500
10k
56.2k
100
20pF
positive feedback out
negative feedback out
undamped feedback bus #28
damped feedback bus #36
10nF
100µF
8µF
RC time constant

Figure A2: Sample and Hold Circuit

The sample and hold circuit is centered around the AD7870 which is an analog to digital converter with 12-bit accuracy and a built in sample and hold. It begins conversion of the analog input voltage when the CS signal makes a high to low transition; conversion is complete with 40 μs. The data are enabled for reading and conversion to an analog voltage when the RD input signal makes a high to low transition. The digitized voltage remains unchanged until the CS input signal again makes a high to low transition. The triggering pulses are generated by monostable vibrator #2 (74221), which is triggered by a pulse from monostable vibrator #1. The initial pulse is triggered by a panel momentary closed switch. The AD 7870 has an input range of +3 V to -3 V; consequently, the input voltage from $Z_{out}/20$ is reduced by a factor of ten to protect the device. The digitized voltage is converted to an analog voltage by the AD566A, which is a continuous digital to analog converter with a range of +5 V to -5 V. Consequently, the output of the AD566A is 5/3 the input to the AD7870. The final output of the AD566A is re-adjusted to the desired voltage by a voltage amplifier with a panel potentiometer as one of the resistors. This allows the user to compensate for digitization errors, since the AD7870 is sensitive to ringing in the trigger signal and has a tendency to make conversion errors.

S1 is a panel switch, momentary closed, that begins the series of pulses that trigger the sample and hold circuit.

P1 is a panel potentiometer that adjusts the final output of the sample and hold circuit.

All op-amps are AD544s or equivalent unless otherwise specified.

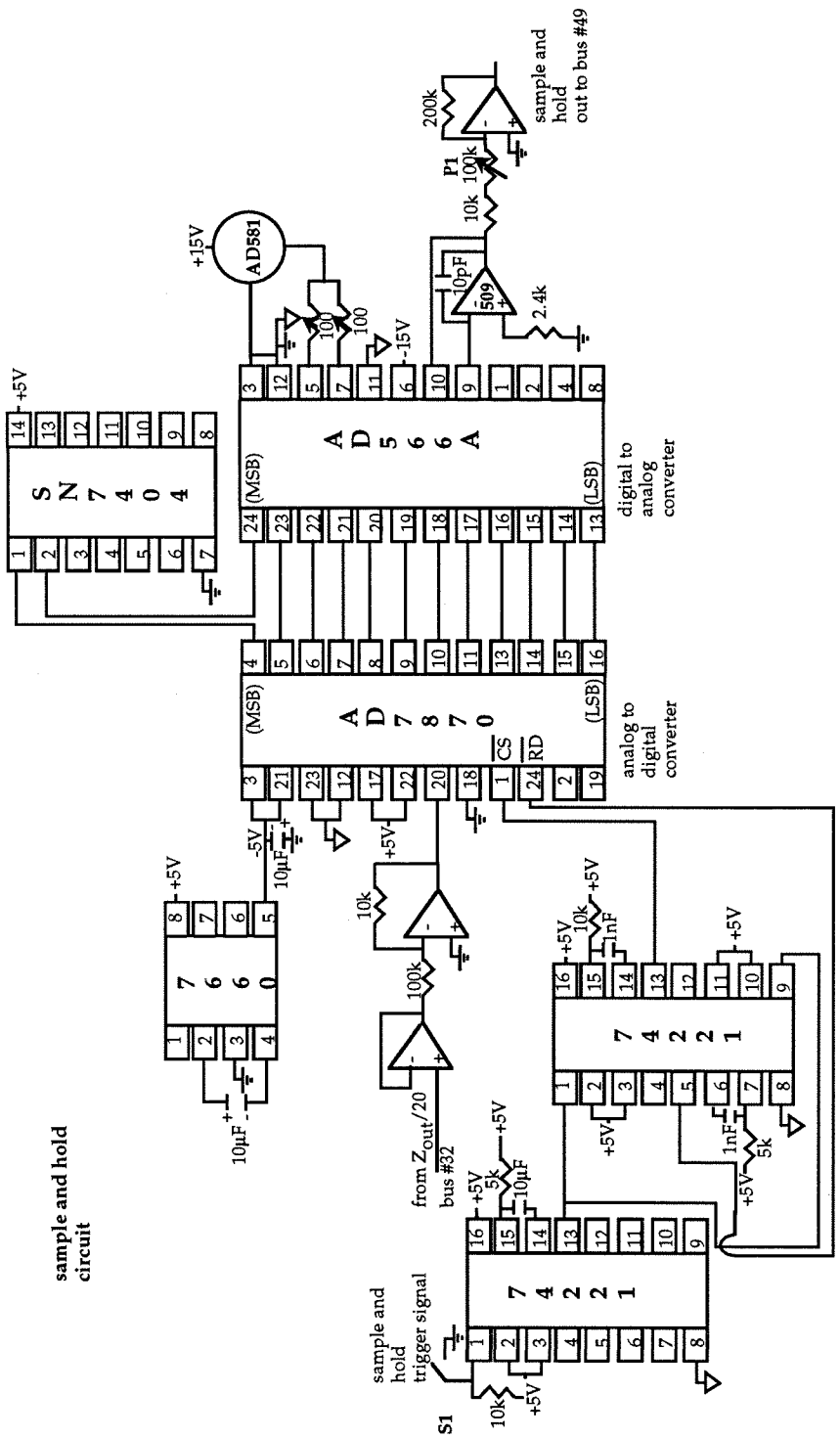
sample and hold circuit
SN7406
AD581
+15V
-15V
+5V
-5V
ADC566A
(MSB)
(LSB)
digital to analog converter
ADC7870
CS
RD
analog to digital converter
sample and hold out to bus #49
200k
P1
100k
10k
10pF
509
2.4k
100
10µF
10k
100k
from Zout/20 bus #32
sample and hold trigger signal
S1
5k
1nF
74221

Figure A3: Z Piezo Driver Circuit

The z piezo driver circuit amplifies inputs from a variety of sources and applies the amplified signal to the inner electrode of the piezo, driving it in the z direction.

S1 is a panel switch that selects between active feedback or the sample and hold output.

S2 is a panel switch that enables the application of an external voltage source to the z piezo signal.

The AD7510 and AD7511 are electronic switches that enable a retraction signal, generated by the approach pulse circuit, to be applied to the piezo during fine approach. All op-amps are AD544s or equivalent unless otherwise specified. The PA83 is a high voltage op-amp with power supplies of ±150 V.

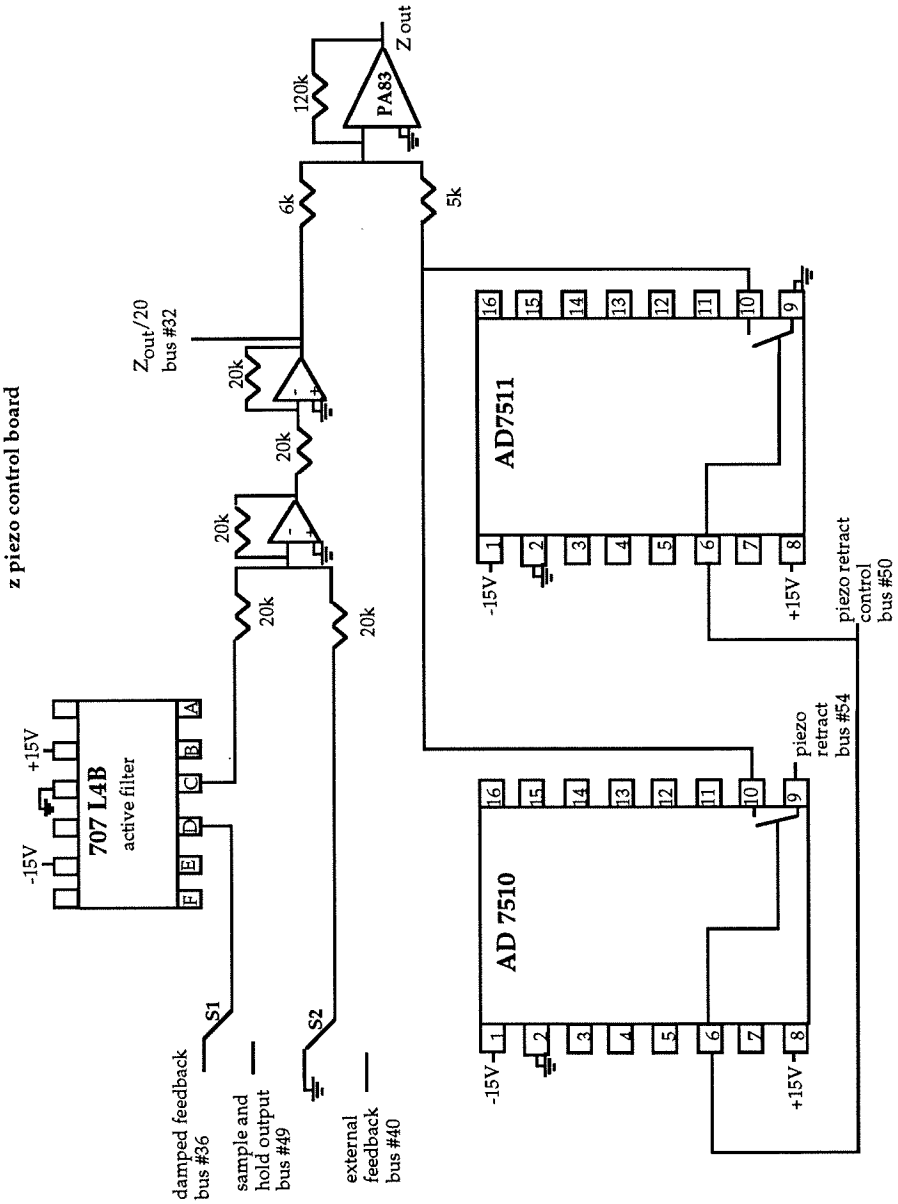
z piezo control board
707 L4B
active filter
-15V
+15V
A
B
C
D
E
F
20k
20k
20k
20k
6k
5k
120k
PA83
Z out
$Z_{out}/20$
bus #32
S1
S2
damped feedback
bus #36
sample and
hold output
bus #49
external
feedback
bus #40
AD7511
AD 7510
-15V
+15V
piezo retract
control
bus #50
piezo
retract
bus #54

Figure A4: Offset Circuit

The offset circuit sums and amplifies the outputs from the sample and hold circuit and $Z_{out}/20$. The degree of amplification is selected at a panel switch. All op-amps are AD544s or equivalent.

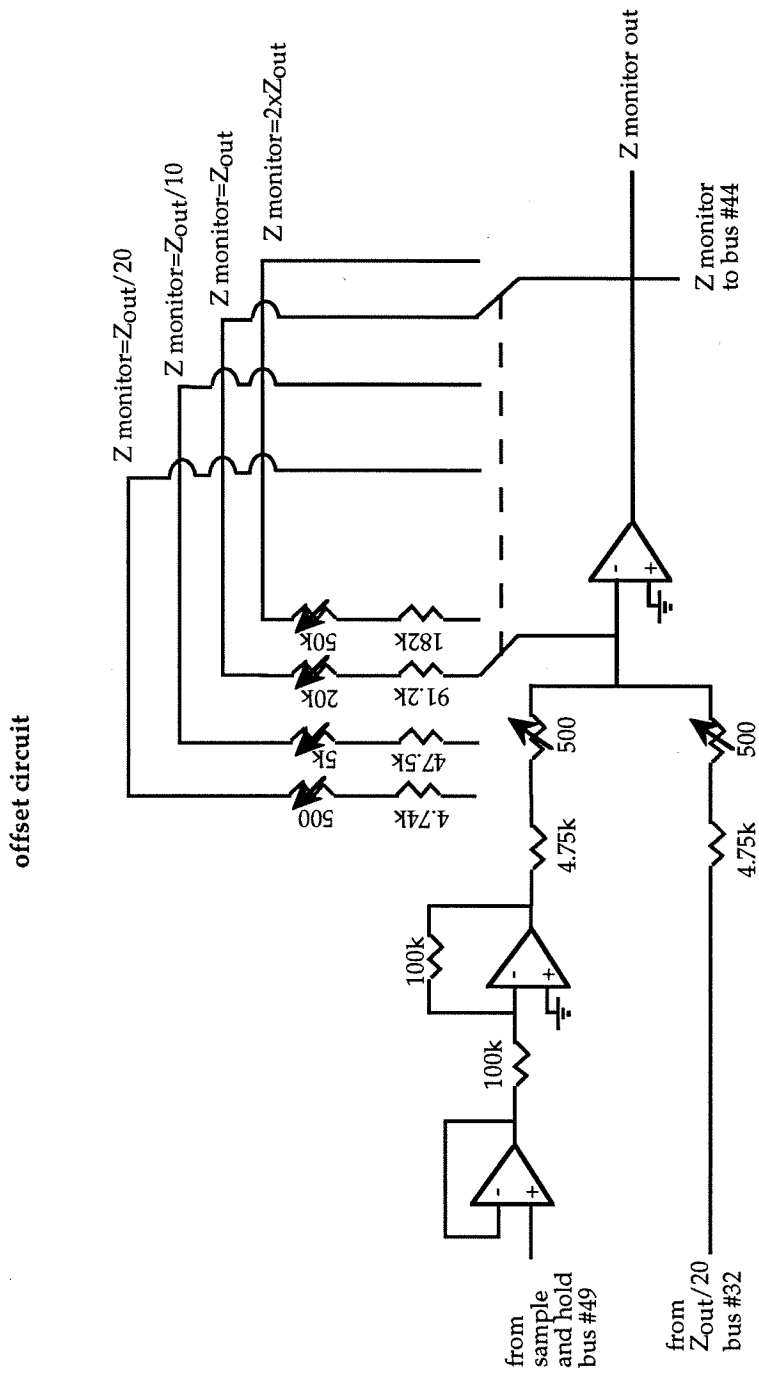
offset circuit
Z monitor=Zout/20
Z monitor=Zout/10
Z monitor=Zout
Z monitor=2xZout
Z monitor out
Z monitor to bus #44
500
4.74k
5k
47.5k
20k
91.2k
50k
182k
500
500
4.75k
4.75k
100k
100k
from sample and hold bus #49
from Zout/20 bus #32

Figure A5: X and Y Scanner Circuit

The x and y scanner circuit drives the scanning motion of the piezo. A sinusoidal or sawtooth signal applied to the input of each circuit, amplified several times, and applied to one electrode of the outer tube of the piezo. The opposite electrode is grounded. The scan width can be adjusted by panel potentiometers and a panel switch. In addition, an adjustable DC offset can be applied to each circuit. The offset is adjusted by a panel potentiometer.

P1 and **P1'** are panel potentiometers that adjust the scan width. They are tied together so that the x and y scan windows are adjusted symmetrically.

P2 and **P3** adjust the DC offset in the x and y piezos, respectively.

S1 is a panel switch that selects between wide range and small range scans. It can also be used to disable the scan signal.

S2 allows the user to select and adjust different shapes for the scan window.

All op-amps are AD-544s or equivalent unless otherwise specified. The PA83s are high voltage op-amps with power supplies of ±150 V.

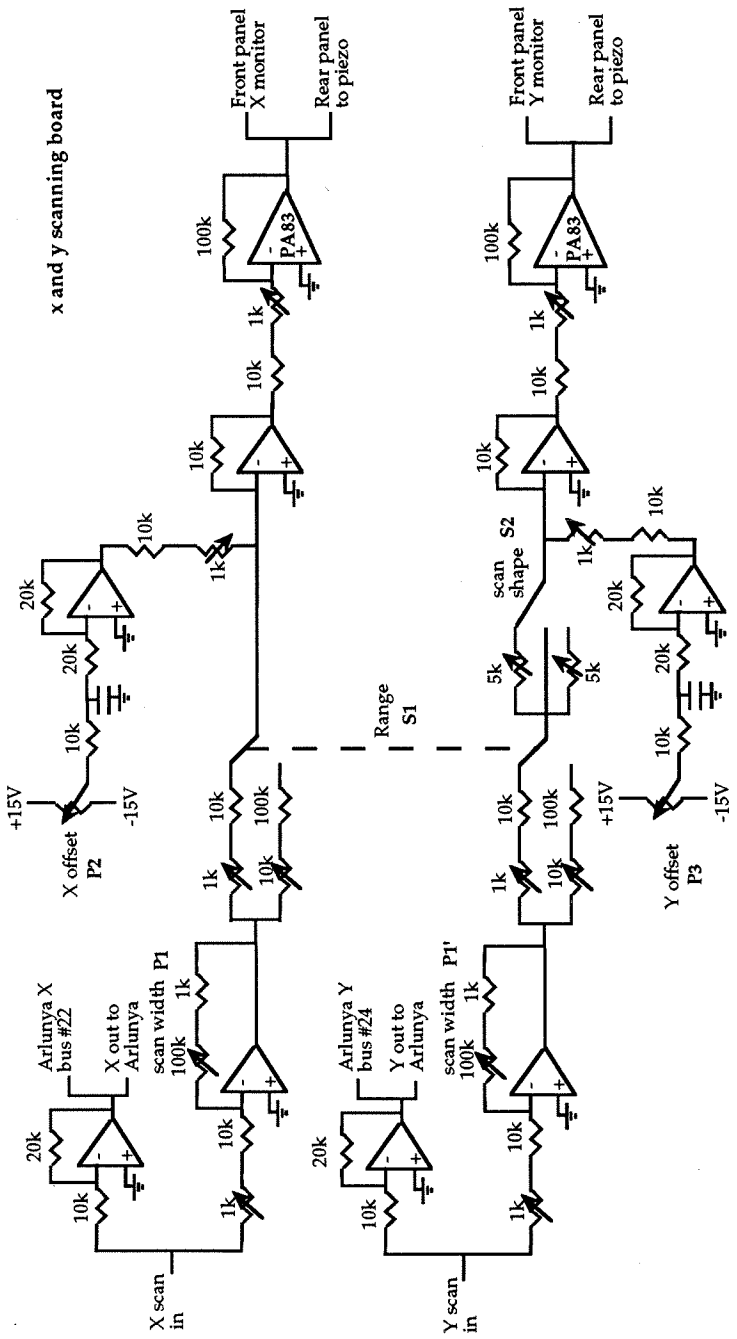
x and y scanning board
Front panel X monitor
Rear panel to piezo
Front panel Y monitor
Rear panel to piezo
PA83
PA83
Range S1
scan shape S2
X offset P2
Y offset P3
+15V
-15V
Arlunya X bus #22
X out to Arlunya
scan width P1
Arlunya Y bus #24
Y out to Arlunya
scan width P1'
X scan in
Y scan in
20k
10k
1k
100k
5k

Figure A6: Approach Pulse Circuit

This circuit generates a train of 12 ms wide pulses, 85 ms apart, which is sent to the stepper motor during fine approach of the tip to the sample. When tunneling current is sensed, the pulse train is terminated and a +15 V signal is sent to the z piezo amplification circuit, causing the z piezo to retract. The voltage slowly drains off, allowing the piezo to re-extend until the feedback circuitry takes over.

S1 is a panel switch, momentary closed, that triggers the start of the pulse train.

S2 is a panel switch that allows the user to disconnect the pulse train from the stepper motor.

P1 is a panel potentiometer that adjusts the height of the pulses in the pulse train.

All op-amps are CA3160s with power supplies of +5 V and ground, unless otherwise indicated.

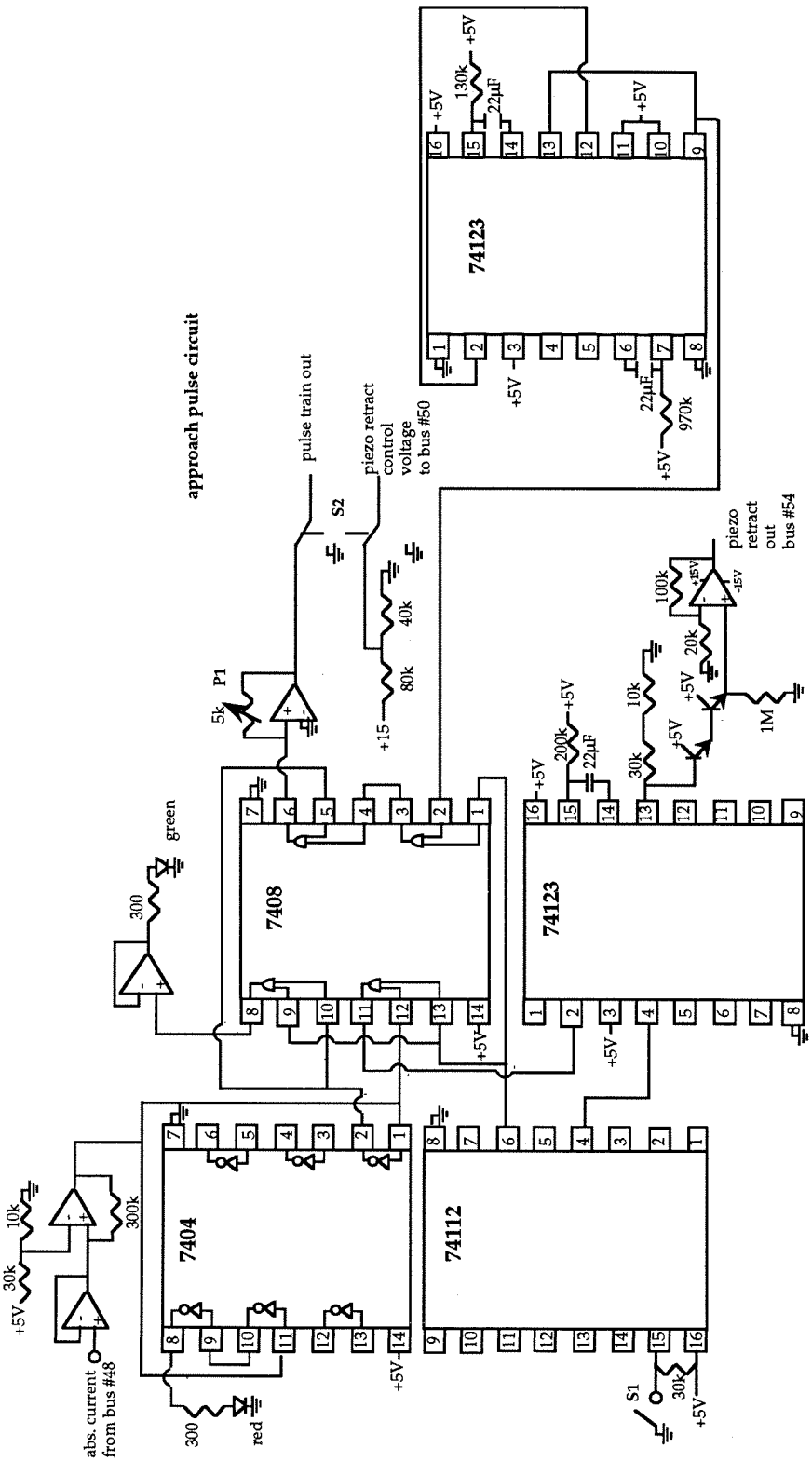
approach pulse circuit
pulse train out
piezo retract control voltage to bus #50
S2
P1
5k
+15
80k
40k
green
300
7408
74123
74123
7404
74112
+5V
10k
30k
300k
abs. current from bus #48
300
red
S1
30k
130k
22µF
970k
200k
100k
20k
1M
piezo retract out bus #54

Figure A7: Bias Supply Circuit

The bias supply circuit sets the bias between the tip and the sample. It has two ranges and allows the user to apply a pulse of adjustable height and width to the bias.

S1 is a panel switch that switches the range of bias voltages between ±15 V and ±400 mV.

S2 is a panel switch, momentary closed, that triggers a pulse in the bias voltage.

P1 is a panel potentiometer that adjusts the bias voltage.

P2 is a panel potentiometer that adjusts the height of the bias voltage pulse.

P3 is a panel potentiometer that adjusts the width of the bias voltage pulse.

All op-amps are AD544s or equivalent.

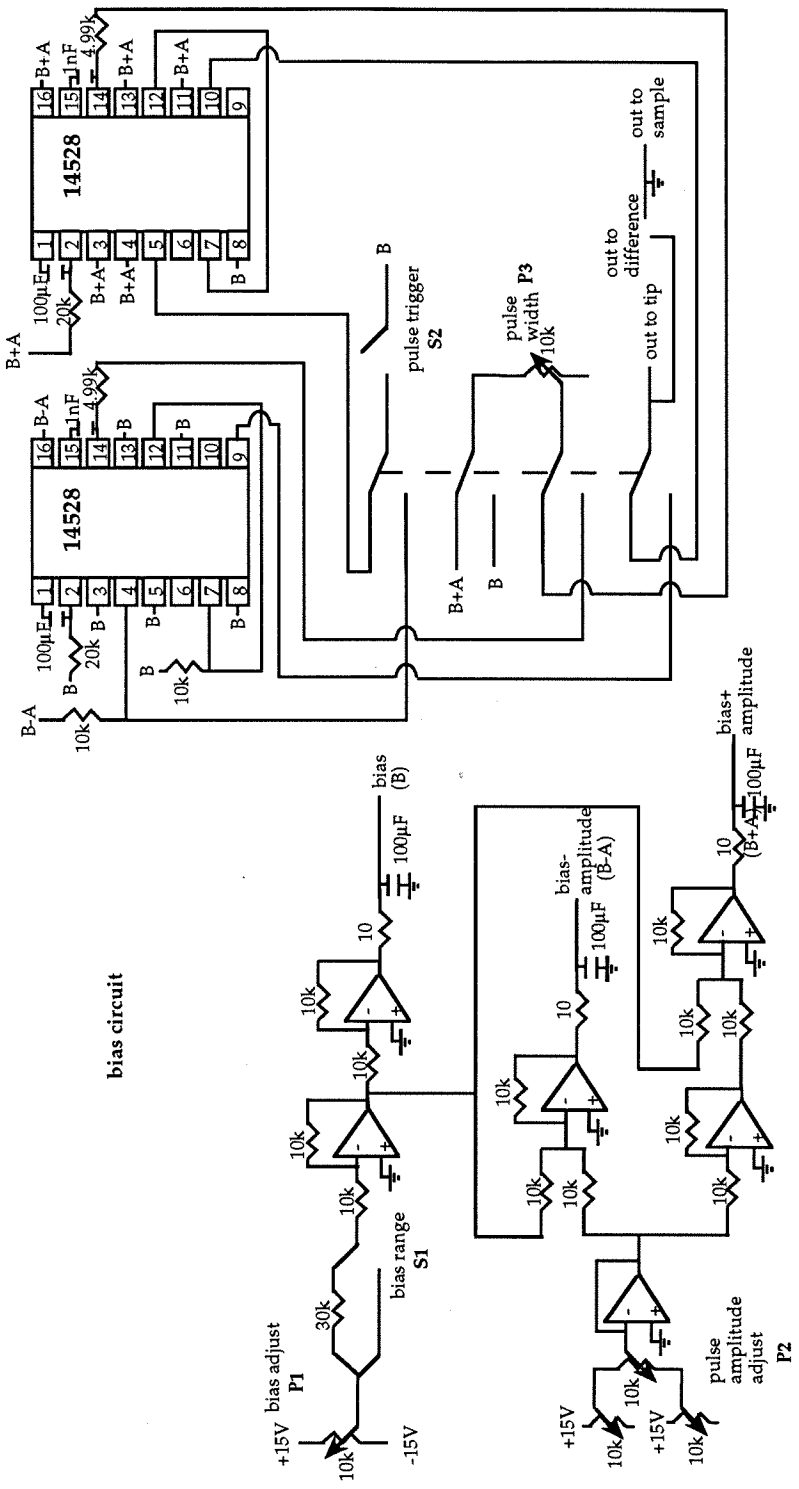
14528
14528
B+A
B-A
B
100µF
20k
10k
4.99k
1nF
pulse trigger
S2
pulse width P3
10k
out to difference
out to tip
out to sample
bias circuit
bias (B)
100µF
bias-amplitude (B-A)
bias+ amplitude
(B+A)
bias adjust P1
+15V
-15V
30k
bias range S1
pulse amplitude adjust P2
10k
10

Chapter 4:
Measurements of Solvent Effects on Local Barrier Heights in STM

Introduction

The question of what factors affect local barrier heights in STM experiments is both interesting and difficult to answer. Unfortunately, local barrier heights for most tip/sample combinations appear to be strongly modified by the presence of contaminants (in the form of carbonaceous material or water) on the tip and surface.[1,2,3] True tests of the conductance of adsorbates on surfaces or solvent molecules in the tunnel gap are also hindered by the presence of such contaminants. A detailed discussion of these effects is presented in Chapter 2 of this thesis. In order to unambiguously examine the effective barrier height of solvents in the tunnel gap, it would be very desirable to obtain a surface that is free of contaminants.

Finding a contaminant free surface is a remarkably difficult enterprise. It is well known from surface spectroscopy that most initially clean surfaces rapidly accumulate several monolayers of carbon and water under non-ultrahigh vacuum (UHV) conditions. Even under UHV, most pristine surfaces will slowly accumulate contamination unless the vacuum is exceptionally good. Ordered gold surfaces have a tendency to remain cleaner than most surfaces; this relative cleanliness is reflected in reports of relatively high effective barrier heights for gold in air.[4,5,6] Unfortunately, for all its stability, gold has a high mobility on itself and disorders over time, losing its resistance to contamination.

Another even more promising substrate is the Pt(111)($\sqrt{7}$x$\sqrt{7}$)R19.1°-I surface (for the sake of convenience, this surface will be referred to as the ($\sqrt{7}$x$\sqrt{7}$) surface in the remainder of this chapter). First prepared and characterized by Hubbard and Felter, this surface is both hydrophobic and remarkably resistant to contamination in air.[7] It has also been imaged with STM in air.[8,9] If this surface truly remains contaminant free, it should ideally yield barrier heights on the order of several electronvolts with a Pt or Pt/Ir tip, since the work functions of platinum and iridium are on the order of 5.7 eV,[10] and that of iodine is in the range of 2.8 to 6.8 eV.[11] Unfortunately, no work function measurements specifically for the ($\sqrt{7}$x$\sqrt{7}$) surface have been reported, so a more precise estimate of the predicted barrier height is not possible.

Another advantage of the ($\sqrt{7}$x$\sqrt{7}$) surface is that it provides a convenient method for estimating degree of contamination. If any contamination of the surface occurs during experiments, the amount of carbon and oxygen can be compared to the amount of iodine. Since the iodine coverage is known to be three iodine atoms per seven platinum atoms, a rough estimate of carbon and oxygen coverage can be obtained. Such an attempt to quantify the extent of contamination has not been described in the various reports of barrier height measurements, even where low barrier heights are presumed to result from contamination.[1-5]

Experimental Procedure

Surface preparation and characterization

In order to carry out the desired scanning tunneling spectroscopy experiment, it was necessary to prepare a Pt(111)($\sqrt{7}$x$\sqrt{7}$)R19.1°-I surface that was free of contaminants. The preparation and characterization of this surface involved extensive use of low energy electron diffraction (LEED) and x-ray photoelectron spectroscopy (XPS). A drawing and description of the ultrahigh vacuum surface analytic system used in the described experiments is given in Figure A1 of the appendix to this chapter. A detailed description and discussion of the preparation of the surface is also given in the appendix to this chapter. A description of the scanning tunneling microscope and control electronics used in the experiments is provided in Chapter 3 of this thesis.

The clean ($\sqrt{7}$x$\sqrt{7}$) surface was prepared according to a procedure based on a method originally developed by Hubbard *et al.*[12] Clean in this sense meant the surface gave a sharp, bright, low background ($\sqrt{7}$x$\sqrt{7}$)R19.1° LEED pattern, and no carbon or oxygen was detectable by XPS. The sample was removed through an electrochemical antechamber attached to the main system, which had been baked overnight at ~150 °C and allowed to cool. This process was necessary to obtain a clean surface, since removal through a rapid access load-lock (pumped by a turbo pump) tended to result in extensive contamination of the surface, probably due to the process of venting the turbo pump. The electrochemical chamber, on the other hand, could be vented with dry argon or nitrogen separately from any turbo pumps or other oil driven pumps. This procedure proved

to be intrinsically cleaner than removing the sample through the rapid access load-lock. Again, clean meant that the sample still produced a sharp, low background ($\sqrt{7}x\sqrt{7}$) LEED pattern and was free of oxygen and carbon by XPS.

After the STM experiments were carried out, the platinum crystal was mounted on a UHV sample stub and loaded into the electrochemical chamber. The chamber was pumped down to a pressure of lower than $1x10^{-4}$ torr using a liquid nitrogen cooled sorption pump, and the sample was transferred to the main UHV system. The surface was examined with LEED and XPS to determine the degree of contamination. Estimation of carbon and oxygen coverage is described in the Results section.

STM experiments

Prior to the STM experiments, the solution cell, attached tubing, and Teflon cap were soaked for several hours in a mixture of RBS detergent (which is a standard de-greasing agent) and de-ionized water. Everything was then rinsed with fresh Nanopure water and allowed to air-dry in a laminar flow hood. A nitrogen gun was periodically used to dispel water droplets from crevices. The STM base was reassembled just prior to the experiments. This procedure was employed to prevent contamination of any solvent added to the solution cell by the cell and components.

Once the sample was removed from UHV, it was loaded into the STM, using a sample holder topped with a metal plate as described in Chapter 3. The quartz post of the sample holder was wrapped with Teflon tape as well as being lined with a Teflon o-ring to insure a firm, solvent-tight fit. Pt/30% Ir tips were prepared a few minutes prior to the experiments by electrochemical etching in a NaCN/KOH solution as described in the literature.[13] The tip was brought within a few hundred microns of the sample surface using the manual coarse approach system described in Chapter 3. Automatic approach was generally achieved with pulse heights of 6-8 V.

Once tunneling current was established, the system generally required 1-2 hours to reach thermal equilibration. Rather frequently, the tunneling current coupled into a noise source that contained components

at ~5 kHz and ~60 Hz. Attempts to exclude the noise through grounding lines, shielding, and filtering were generally unsuccessful. The only approach that worked was waiting for a window of quiet and operating at low gains and high damping filters.

When the noise was not present and drift due to thermal imbalance or sample roughness was near zero, the active feedback could be disabled without significant change in the tunneling current. An external, linear scanning voltage was applied to the sample and hold voltage such that the tip was retracted at a rate of about 3 Å/sec. The current was recorded as a function of change in the voltage being applied to the z piezo on an x-y chart recorder. An overview of the experimental set-up is shown in Figure 1. When the tunneling current had decayed to zero (generally after an increase in tunneling gap of 15-20 Å), the scan was reversed, and the tip was re-extended toward the surface, again at a rate of ~3 Å/sec. If the retraction and extension curves overlapped or were within a few millivolts (i.e., tenths of angstroms) of each other, the curve was deemed to be free of distorting factors such as thermal drift or piezo creep. If there was significant discrepancy between the retraction and extension curves, the data were disregarded. Several curves were taken for a given spot at a given bias voltage. Periodically, a series of 1 μs, 1 V, tip negative pulses were applied to the bias voltage in an attempt to clean the tip. Such pulses were sufficiently short that they did not affect the feedback. The same general procedure was used for barrier height measurements in air and hexadecane.

For experiments involving hexadecane, several curves were first taken in air to establish that the electronics were functioning properly. Hexadecane was chosen because it is an inert, high boiling liquid that is a common greasy standard in contact angle measurements.[14] The hexadecane was kept in a nitrogen purged glove box until a few hours before its use in the STM. At that time, ~10 mL were transferred to a bottle with a Teflon-lined cap, where it remained until addition to the STM solution cell. The hexadecane was drawn into a glass syringe and injected into the STM cell through polyethylene or Teflon tubing. The level of the hexadecane was monitored so that it covered the surface of the sample but did not contact the tip holder or piezo. Generally, addition of hexadecane

to the STM cell caused the tip to drift out of tunneling range, requiring re-approach.

After addition of hexadecane to the STM cell, the system was allowed to thermally equilibrate before retraction and extension curves were measured. Several curves were taken at each spot and bias voltage. The level of hexadecane was checked periodically to insure that the surface of the sample remained covered. At the end of the STM experiment, the hexadecane was removed from the cell, the base was disassembled, and the sample was rinsed with isopropanol before being returned to the UHV system. The rinsing was carried out to reduce contamination of the UHV sample holder and other components by hexadecane.

Data processing

The data were digitized by hand using a Houston Instruments Hi-pad digitizer and a conversion program. The digitized data were then transferred to standard graphing programs and evaluated. XPS spectra were recorded and analyzed using software provided with the system.

Results

In general, the retraction/extension curves showed an exponential dependence on the gap width. A typical retraction curve is shown in Figure 2a. A plot of the logarithm of the current versus change in gap width is shown in Figure 2b. This curve was taken in air at a tip positive bias of 200 mV; the inferred barrier height is 0.33 eV. This barrier height is calculated from a fit to the exponential curve using the equation:

$$i_t \propto V_B \exp(-A\phi_{eff}^{1/2} s)$$

where V_B is the bias voltage, A is a constant taken to be 1.025 $eV^{-1/2}Å^{-1}$, ϕ_{eff} is the effective barrier height in electronvolts, and s is the gap width in angstroms. For a detailed discussion of this equation and the effective barrier height, see Chapter 2.

The log of the current versus gap width showed an abrupt change in slope at about 10 pA. An abrupt change of this sort was observed for most of the digitized curves, but it was not used to determine the barrier height.

These data are in a region where the sensitivity of the pre-amplifier is questionable. In addition, this region is close to the baseline, and digitization errors are likely. Thus, while the change in slope might have physical meaning, it is just as likely to be due to systematic errors in data acquisition and processing.

Average barrier heights as a function of bias voltage obtained in air are shown in Table 1. The values reported are the means of the barrier heights calculated from all curves that showed exponential, reproducible behaviour, as described in the Experimental section. At least four values were used to calculate each mean, and the errors represent the standard deviation. Disappointingly, the barrier heights are much lower than one would expect for this tip/sample combination, based on the work functions for platinum, iridium, and iodine. Regardless, measurements were conducted in hexadecane to determine if the barrier height was significantly different in the solvent than in air. In addition, a greater bias voltage range was explored. The results of the hexadecane experiments are listed in Table 2. The same criteria apply for these values as for the values listed in Table 1, except that, due to more extensive noise at the higher bias voltage, only three values were included in the mean calculated for a bias voltage of 3 V. A few general trends are apparent from the data.

Average Barrier Heights in Air

bias voltage (mV)	average barrier height (eV)
50	0.24±0.13
100	0.13±0.07
200	0.29±0.06
500	0.25±0.06

Table 1: Average barrier heights as a function of bias voltage in air. Bias voltage signs are referenced to the tip.

Average Barrier Heights in Hexadecane

bias voltage (mV)	average barrier height (eV)
-500	0.67±0.40
-50	0.38±0.26
50	0.20±0.11
500	0.74±0.42
3000	1.31±1

Table 2: Average barrier heights as a function of bias voltage in hexadecane. Bias voltage signs are referenced to the tip.

First, the barrier height does not appear to depend on the magnitude of the bias voltage in air. There does appear to be some bias voltage dependence in hexadecane, although the degree of deviation in the measurements renders any conclusions tentative at best. Both the trends and degree of deviation are shown in Figure 3, which depicts plots of the average barrier heights versus bias voltages in air and hexadecane.

Second, there does not appear to be a significant difference between the barrier heights measured in air versus those measured in hexadecane at a bias voltage magnitude of 50 mV. The barrier height at a bias voltage magnitude of 500 mV does appear to be greater in hexadecane than in air, although the deviation in measurements in hexadecane was rather extensive at both positive and negative biases. Consequently, it is rather difficult to draw any firm conclusions from these data.

Finally, although not evident from the listed data, the barrier height measured under a given ambient and at a given bias voltage was not time dependent; that is, the barrier heights did not decrease over time, as reported by various investigators.[5,6] Since the authors in these reports explain the drop in barrier height as accumulation of contamination at a given spot, that suggests that little contamination accumulated on the ($\sqrt{7}$x$\sqrt{7}$) surface during the process of obtaining a set of curves. For the experiments reported here, each curve took several seconds to obtain and

several were obtained at a given spot, over the course of a few minutes. Whether the curve was representative of a relatively high or low barrier height did not depend on the order in which it was obtained. In addition, curves obtained later in the day did not show lower barrier heights than those obtained earlier in the day. Again, all this suggests that variations in data are not merely a function of changes in degree of contamination.

The lack of any true distinction between the barrier heights in air and the barrier heights in hexadecane discouraged us from extending the study to water. Some preliminary studies in air and water using a platinum foil substrate yielded similar barrier heights and deviations as those reported here. Experiments involving water require tips partially insulated with glass and are consequently more difficult than those involving hexadecane; thus, it seemed pointless to conduct those experiments over the optimized ($\sqrt{7}$x$\sqrt{7}$) surface.

Surface contamination was evident by both XPS and LEED after the STM experiments. However, the extent of contamination was highly dependent on how the surface had been treated. Generally, the surface was highly contaminated after STM experiments under hexadecane. In most cases, no LEED pattern was visible and there was extensive coverage of carbon and oxygen evident by XPS, as shown in the top spectrum in Figure 4. This spectrum is typical of XPS spectra of the ($\sqrt{7}$x$\sqrt{7}$) surface after experiments involving hexadecane, which also involved extensive rinsing (as described in the Experimental section).

An estimate of the degree of contamination can be obtained by comparing the area under the C 1s peak to the area under the I $3d_{5/2}$ peak. After normalizing for differences in the photoionization cross-sections and electron escape depths, the ratio of carbon to iodine was about 16:1. Assuming that the coverage of iodine was still that for a ($\sqrt{7}$x$\sqrt{7}$) surface (known to be three iodine atoms for every seven surface platinum atoms[4]) which is roughly half of a full monolayer, then the amount of carbon was about eight monolayers. Taking the thickness of one monolayer of carbon to be the atomic diameter of carbon (~1.5 Å), this translates to about 12 Å of carbon contamination. This is a thick layer of contamination and would be expected to have a profound affect on barrier height measurements if it were present during the entire course of the experiments.

However, that degree of contamination is not necessarily intrinsic to the experimental conditions. The lower spectrum in Figure 4 is typical of that for a surface that had only been exposed to air and the STM apparatus (in this case for nine hours) and not to hexadecane or rinsing. In addition, the ($\sqrt{7}$x$\sqrt{7}$) LEED pattern was still visible when the sample was only exposed to air, indicating that the surface had not disordered or lost its protective layer of iodine. For this particular spectrum, the amount of carbon contamination that had accumulated was roughly a monolayer, which would not necessarily be expected to strongly affect the barrier height, particularly at greater tip-sample separations.

Discussion

The first conclusion that can be drawn from the results is that the Pt(111)($\sqrt{7}$x$\sqrt{7}$)R19.1°-I surface does not provide the reproducibly contaminant free, high barrier height substrate we had hoped for. This is evident from the information provided by LEED and XPS, as well as the relatively low barrier heights obtained in air. The surface does remain reasonably clean in air for relatively long periods of time, as discussed in the results section. Indeed, the relatively small degree of contamination on the surface raises the question of the role of the tip in barrier height measurements. Generally, the tip is not emphasized in considerations of STM images and barrier heights, since the nature of the tip is difficult to treat and similar images can be obtained with different tip materials.[15,16] However, the tip clearly must play a part in supporting tunneling current and can be contaminated with carbon or water just like the sample surface.

The microscopic nature of the end of the tip makes it a difficult subject for characterization, and we could think of no treatment that would guarantee a clean tip. We hoped that the bias pulsing, described in the Experimental section, would be sufficient to clean the tip as it had for some investigators.[3] That approach was probably not successful, since all the barrier heights obtained in air and most of the barrier heights obtained in hexadecane were much lower than would be expected for a clean system.

The most attractive explanation for the low barrier heights observed in both air and hexadecane is that contamination-mediated surface forces

determine the effective barrier height, as proposed by various groups.[2,17] This model, described in Chapter 2, essentially describes the contamination layer as acting as a spring. As the tip retracts, the contamination spring stretches with it, effectively decreasing the rate at which the tip retracts from the surface. This also decreases the rate at which the tunnel gap widens and thus lowers the barrier height inferred from the fit of tunneling current versus increasing gap width. Assuming that the level of contamination is a combination of tip and sample for the case of the ($\sqrt{7}$x$\sqrt{7}$) surface and that this level is constant over the surface, the barrier height would be expected to be fairly constant over the surface and independent of bias voltage, as is the case in air.

If the model described above is accurate, the presence of hexadecane on the surface would not necessarily be expected to influence the barrier height. The overwhelming influence is from the surface force interaction; little modulation is provided by the hexadecane in the gap. It is also conceivable that the hexadecane could rinse some of the contamination away, effectively increasing the inferred barrier height. That would be consistent with the slightly higher barrier heights measured in hexadecane than in air.

Other types of surfaces might be more suitable for these measurements than the Pt(111)($\sqrt{7}$x$\sqrt{7}$)R19.1°-I surface. Song *et al* .[5] and Pan *et al.*[6] saw differences in the effective barrier heights for various solvents using gold as the substrate, although the barrier heights for gold in air were low. Thus, gold might provide more reproducible and reliable measurements than the Pt-I system used in the experiments described above. Organic films such as Langmuir-Blodgett films or alkanethiols are additional types of substrates that might provide qualitative differences in solvent effects on barrier heights. Sasaki *et al.*[4] saw reproducible barrier heights of 2 eV in air for Langmuir-Blodgett films deposited on various substrates, regardless of the barrier height of the substrate. The reproducibility of the barrier height they obtained is an attractive feature of the films and would possibly allow for more definitive investigations of solvent effects in such systems.

Conclusion

We attempted to carry out reproducible measurements of the effects of solvents on barrier heights in STM. Measurements of this kind are hampered by the presence of contamination on the sample surface, which tends to lower the effective barrier height and complicate the interpretation of the effects of solvent. As our substrate, we chose the Pt(111)($\sqrt{7}$x$\sqrt{7}$)R19.1°-I surface, which is well characterized and resistant to contamination in air. With this surface, we hoped to measure a reproducible, high barrier height in air, and then use the same substrate to measure, unambiguously, the effects of solvent on the barrier height. Unfortunately, the barrier height measurements in air yielded low, scattered barrier heights on the order of 0.25 eV, an order of magnitude less than that predicted from the work functions of the materials comprising the tip and the sample. Measurements in hexadecane yielded barrier heights that were the same or even greater than those measured in air, a result that runs counter to prediction and other experiments of this kind.

While this experiment did not work the way we had hoped it would, it did provide some insights. Rough estimates of the degree of surface contamination after the STM experiments in air using LEED and XPS indicated that the surface did not disorder or accumulate much more than a monolayer of carbonaceous contamination. These leads to the conclusion that the tip must play a role equal to that of the surface in contributing to low effective barrier heights. It is possible that other surfaces, such as Langmuir-Blodgett films or alkanethiol monolayers on gold, might yield more reproducible results.

References

(1) Binnig, G.; Rohrer, H.; Gerber, Ch.; Weibel, E. *Appl. Phys. Lett.* **1982**, *40*, 178-180.

(2) Mamin, H.J.; Ganz, E.; Abraham, D.W.; Thomson, R.E.; Clarke, J. *Phys. Rev. B* **1986**, *34*, 9015-9018.

(3) Gimzewski, J.K.; Möller, R. *Phys. Rev. B* **1987**, *36*, 1284-1287. Gimzewski, J.K.; Möller, R.; Pohl, D.W.; Schlittler, R.R. *Surf. Sci.* **1987**, *189/190*, 15-23.

(4) Sasaki, A.; Iwata, F.; Katsumata, A.; Fukaya, J.; Aoyama, H.; Akiyama, T.; Nakano, Y.; Fujiyasu, H. *Jpn. J. Appl. Phys.* **1993,** *32,* 2952-2957.

(5) Song, J.P.; Mørch, K.A.; Carneiro, K.; Thölén, A.R. *J. Vac. Sci. Technol. B* **1994,** *12,* 2237-2242.

(6) Pan, J.; Jing, T.W.; Lindsay, S.M. *J. Phys. Chem.* **1994,** *98,* 4205-4208.

(7) Felter, T.E.; Hubbard, A.T. *J. Electroanal. Chem.* **1979**, *100,* 473-491.

(8) Schardt, B.C.; Yau, S.-L.; Rinaldi, F. *Science* **1989**, *243,* 1050-1053.

(9) Yau, S.-L.; Vitus, C.M.; Schardt, B.C. *J. Am. Chem. Soc.* **1990**, *112,* 3677-3679.

(10) D.R. Lide, Editor, *CRC Handbook, 74th Edition,* CRC Press: Boca Raton, FL, 1994, p**12**-105.

(11) R. C. Weast, Editor, *CRC Handbook, 57th Edition*, CRC Press: Cleveland, OH, 1976, pE81-E82.

(12) Wieckowski, A.; Schardt, B.C.; Rosasco, S.D.; Stickney, J.L.; Hubbard, A.T. *Surf. Sci.* **1984,** *146,* 115-134.

(13) Penner, R.M.; Heben, M.J.; Lewis, N.S. *Anal. Chem.* **1989**, *61,* 1630-1636.

(14) Ulman, A. *Introduction to Ultrathin Organic Films,* Academic Press: New York, 1991, p48-58.

(15) Lang, N.D. *Phys. Rev. B* **1987**, *36,* 8173-8176. Lang, N.D. *Phys. Rev. B* **1988**, *37,* 10395-10398.

(16) Tersoff, J.; Hamann, D.R. *Phys. Rev. Lett.* **1983**, *50,* 1998-2001.

(17) Coombs, J.H.; Pethica, J.B. *IBM J. Res. Develop.* **1986**, *30,* 455-459.

Figure 1:
An overview of the experimental set-up used to obtain tunneling current vs. Δs curves. The PARC 175 supplies the linear scanning voltage applied to the z piezo which causes the piezo to retract or extend. The tunneling current is converted to a voltage signal and amplified by the pre-amplifier such that 1 nA of tunneling current results in a 1 V output signal from the pre-amplifier. The signal from the pre-amplifier is plotted as a function of change in z piezo voltage on the x-y recorder. The change in z piezo voltage is related to change in tip position by the voltage response of the z piezo, which is 32 Å/V as described in Chapter 3.

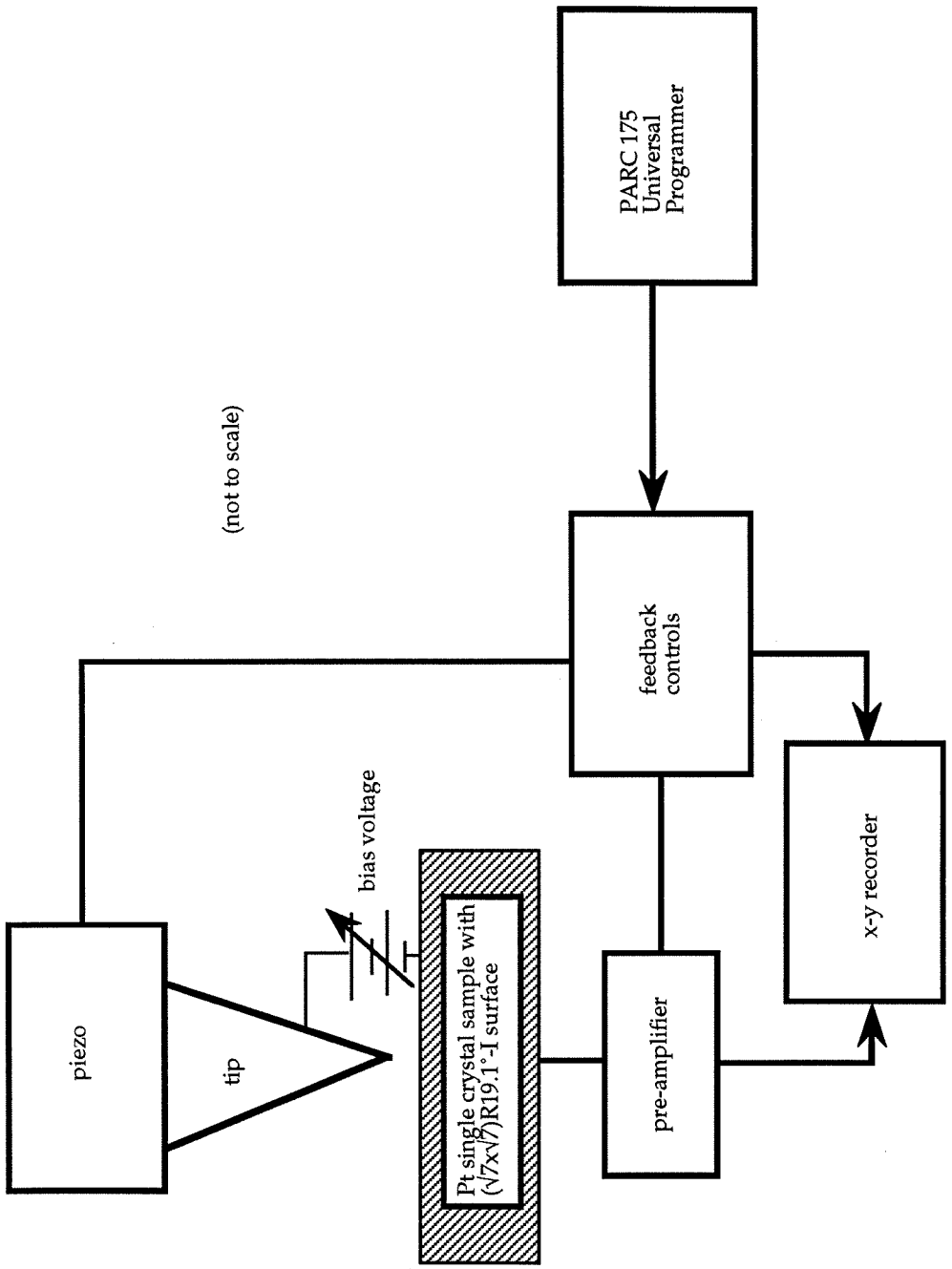
PARC 175
Universal
Programmer
feedback
controls
x-y recorder
pre-amplifier
Pt single crystal sample with
(√7x√7)R19.1°-I surface
bias voltage
tip
piezo
(not to scale)

Figure 2:

a: A digitized plot of the tunneling current vs. increase in tunnel gap width. The sample was a freshly prepared Pt(111)($\sqrt{7}$x$\sqrt{7}$)R19.1°-I surface, with a freshly etched Pt/30 %Ir tip. The curve was collected in air with a tip positive bias voltage of 200 mV. The current was filtered with a 40 Hz low pass filter to exclude line noise. The data are indicated by open circles and the solid line is the exponential fit to the data.

b: A plot of the log of the tunneling current vs. increase in tunnel gap. The same data set as shown in part a was used.

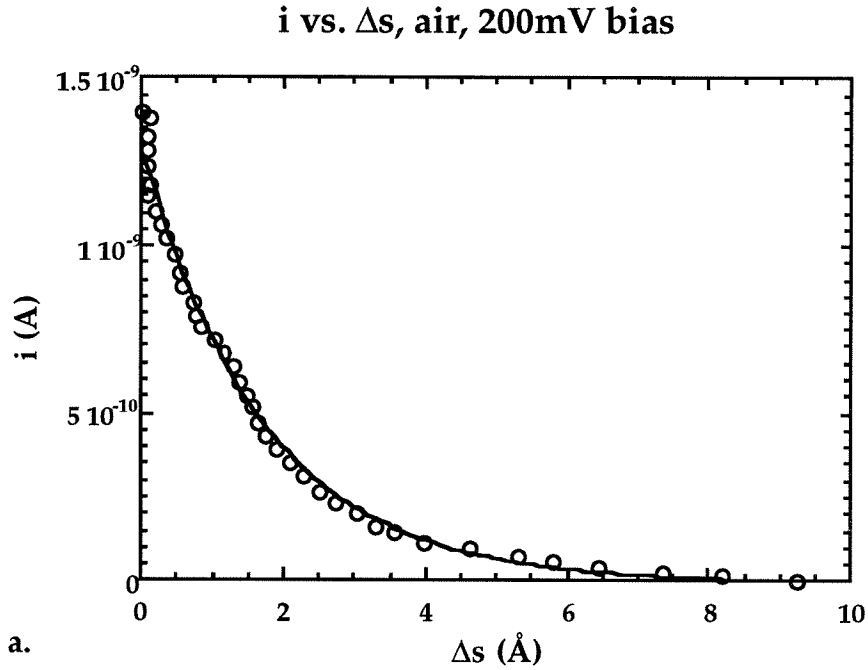
i vs. Δs, air, 200mV bias
1.5 10-9
1 10-9
5 10-10
0
i (A)
0
2
4
6
8
10
Δs (Å)

a.

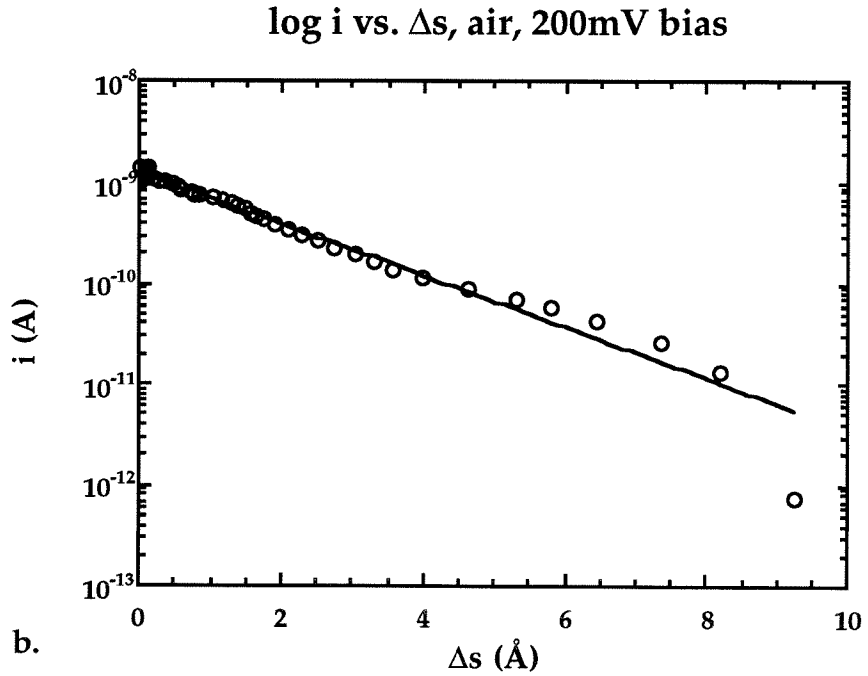
log i vs. Δs, air, 200mV bias
10-8
10-9
10-10
10-11
10-12
10-13
i (A)
0
2
4
6
8
10
Δs (Å)

b.

Figure 3:
a: A plot of the average barrier heights obtained in air as function of bias voltage. The error bars represent the standard deviation in barrier heights at a given bias.
b: A plot of the average barrier heights obtained in hexadecane as a function of bias voltage. Again, the error bars represent the standard deviation in barrier heights measured at a given bias.

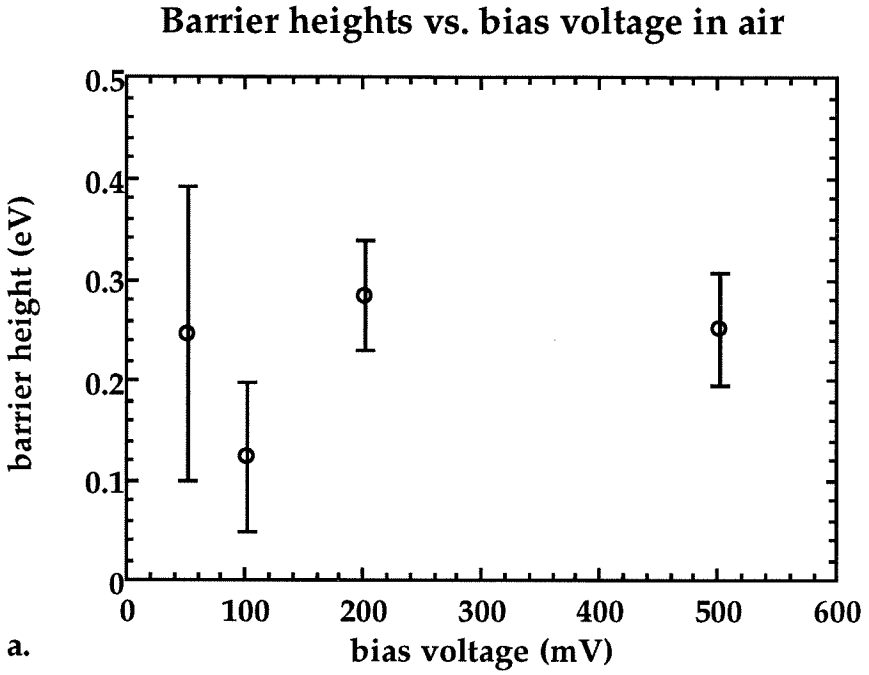
Barrier heights vs. bias voltage in air
barrier height (eV)
0.5
0.4
0.3
0.2
0.1
0
0
100
200
300
400
500
600
bias voltage (mV)

a.

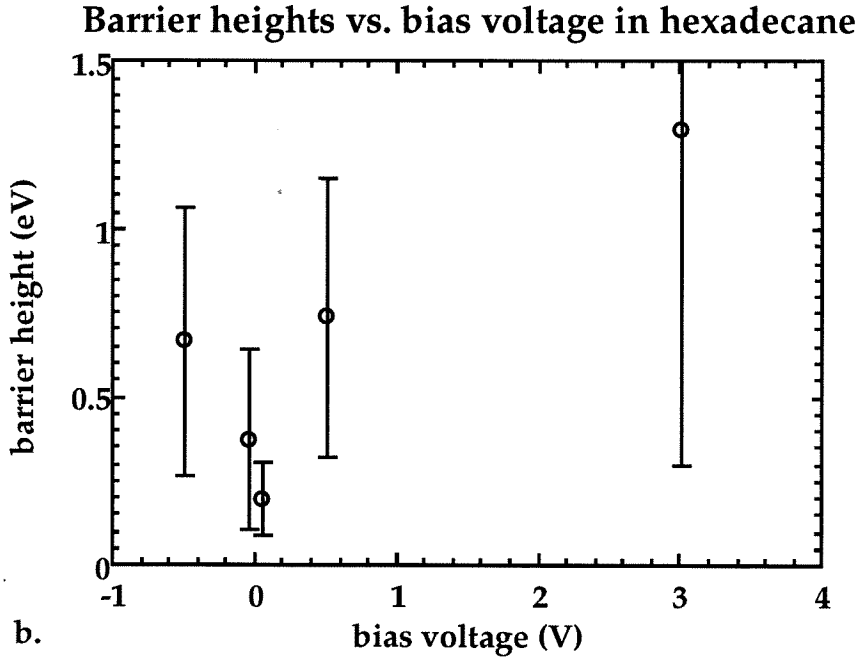
Barrier heights vs. bias voltage in hexadecane
barrier height (eV)
1.5
1
0.5
0
-1
0
1
2
3
4
bias voltage (V)

b.

Figure 4:
Typical XPS spectra of the Pt(111)($\sqrt{7}$x$\sqrt{7}$)R19.1°-I surface after the sample was used in STM barrier height measurements. The upper spectrum is typical of the surface when the sample had been in air several hours, hexadecane was used in the measurements, and the sample had been rinsed with isopropanol before being returned to UHV. The lower spectrum is typical of the surface when the sample had merely been in air for several hours during the course of the STM experiments. Both spectra were taken with a beam size of 400x1000 μm^2 and a pass energy of 155 eV. At this beam size and pass energy, the FWHM of the Au $4f_{7/2}$ peak is 1.50 eV. The position of the beam on the crystal roughly corresponded to the area of the surface involved in the STM experiments.

XPS spectra of surface after STM experiments

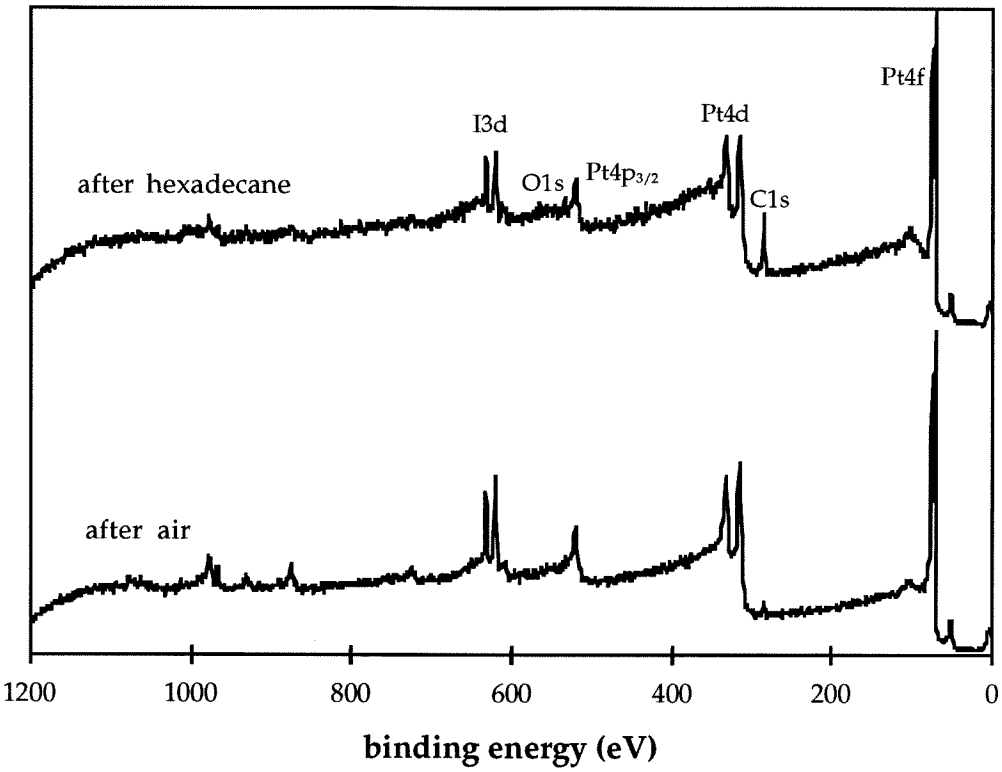

Appendix:
Preparation and Characterization of the Pt(111)($\sqrt{7}$x$\sqrt{7}$)R19.1°-I Surface

Surface Preparation

In order to carry out the described scanning tunneling spectroscopy experiment, it was necessary to prepare a surface that was free of contaminants and would stay free of contaminants. This holy grail of surface science does exist in the form of the Pt(111)($\sqrt{7}$x$\sqrt{7}$)R19.1°-I surface, which can resist adsorption of contaminants for several hours to several days under the right conditions.[1] Exactly what the "right conditions" are varies with preparation method and venue.

The Pt(111)($\sqrt{7}$x$\sqrt{7}$)R19.1°-I surface was first prepared and characterized by Felter and Hubbard in 1979.[2] The initial preparation involved dosing a clean Pt(111) surface with gaseous iodine under ultrahigh vacuum (UHV) conditions. The surface was characterized with low energy electron diffraction (LEED), quantitative Auger electron spectroscopy (AES), and electrochemistry. The iodine overlayer was found to be hydrophobic and remarkably stable to exposure to air. Unlike most surfaces, it also remained free of contaminants upon exposure to solution or air.

Hubbard and co-workers found that the Pt(111)($\sqrt{7}$x$\sqrt{7}$)R19.1°-I surface could be formed under a variety of conditions.[3,4,5] Most conveniently, it could be formed at atmospheric pressures by heating a Pt(111) surface over iodine crystals under a blanket of nitrogen or argon.[5] This procedure produces a surface with an excess of iodine which must be annealed to yield the desired iodine overlayer. The exact conditions necessary to prepare the desired surface vary with experimental apparatus, crystal size, and other factors. This appendix will detail the conditions which yield the surface with the available equipment.

Initially, we attempted to prepare the surface based on a variety of methods established by Hubbard and others.[5,6] Prior to the ready availability of ultrahigh vacuum analytical instrumentation in our labs, the sample was prepared at atmospheric pressure. This was done by heating a platinum single crystal oriented to the (111) face on one side to a red-orange color (~600-700 °C) with a hydrogen flame in a flow of nitrogen. The crystal was then allowed to cool over iodine crystals in an atmosphere of nitrogen. The sample was characterized electrochemically by the underpotential deposition of silver, which should be very sensitive

to the structure and cleanliness of the surface.[5] However, eventual characterization of a surface prepared in this manner with low energy electron diffraction (LEED) and Auger electron spectroscopy (AES) showed no order and the presence of carbon and silver as well as iodine and platinum. In addition, the carbon Auger peak was in the position indicative of graphite, suggesting that the carbon layer formed in the heating process.

Other attempts to prepare the surface involved the use of an ultrahigh vacuum analytical apparatus built in our labs. A schematic and brief description of this apparatus and the instruments that are a part of it appears in Figure A1 of this appendix. This apparatus made the characterization of the surface both convenient and unambiguous. The sample could be cleaned in UHV and then characterized by LEED and x-ray photoelectron spectroscopy (XPS) prior to treatment, then easily characterized again to determine the results of the treatment.

Cleaning of the surface in UHV involves mounting the sample on a heating stub and sputtering and annealing the surface until it appears ordered by LEED and clean by XPS. The sample can be heated either indirectly by conductive heating or directly by resistive heating. For conductive heating, the sample rests on the surface of a specially designed heating stub, the top of which is a molybdenum shell containing a tungsten wire set in a high temperature ceramic. When the stub is plugged into the heating stage and the current turned on, the tungsten wire is resistively heated and the entire top of the stub becomes hot. This method has several drawbacks, all of which relate to the fact that the top of the heating stub must become very hot to effectively heat the sample. This can cause alloying between the platinum sample and molybdenum surface. In addition, any contaminants on the heating stub can migrate to the sample, which makes cleaning of the sample more difficult.

The cleanest method for heating the platinum crystal is by resistive heating. This is done by spot-welding 0.016" or 0.020" platinum wires to the edges of the platinum crystal. During the spot-welding process, the crystal is wrapped in tissue and held firmly in a small vise with the edge to be welded exposed. The platinum wire is pressed firmly to the edge of the crystal with one probe tip with the other probe tip in contact with the edge

of the crystal itself. In general, molybdenum probe tips are used to prevent the tip from melting to the platinum. Several short pulses of 10-15 W·s are generally necessary to establish a firm weld. The weld should be able to withstand gentle tugging and manipulation. Each wire should be welded to the crystal in several spots to ensure sufficient support and electrical contact.

Once firm spot-welds are formed, the sample is cleaned in UHV to remove contaminants and form a well-defined Pt(111)(1x1) surface. The sample is mounted on the heating stub as shown in Figure A2. The wires are compressed between nuts screwed onto the threaded banana plugs on the stub. The back of the sample rests on ceramic beads lining the central post of the stub. This configuration ensures that the aligned and polished surface of the platinum crystal is level and exposed to the argon ion beam and the LEED screen. The stub is plugged into the heating stage, and the sample is sputtered by an aligned, defocused beam of oxygen-free argon for about 10 minutes. Typical conditions for sputtering platinum are an argon pressure of ~$1x10^{-7}$ torr, 10 mA emission current, and a beam energy of 3 keV. The sample is then heated at about 600 °C while sputtering for an additional 10 minutes. The beam is turned off and the sample is heated at 800-850 °C for 3-5 minutes. This is usually sufficient to produce a bright, sharp surface LEED pattern, as shown in Figure A3a. A typical XPS spectrum of a clean platinum surface is shown in the lower spectrum of Figure A4.

The temperature is controlled by maintaining a constant current produced by a Kepco power supply configured to be a constant current source. With the sample mounting configuration described above, a current of 5-6 A is sufficient to heat the sample to 600 °C, and a current of 7.5-8 A is sufficient to heat the sample to 800-850 °C. These settings depend somewhat on the thermal mass of the sample and must be empirically adjusted for different crystals. Above 700 °C, an optical pyrometer is used to monitor the temperature of the sample. Below 700 °C, a Pt-Pt/Rh thermocouple can be used to determine temperature; however, the thermocouple must be in good contact with the sample, and the output has a tendency to fluctuate. It is easier and usually sufficient to estimate the temperature by the color of the crystal. At 600 °C the crystal is

dull red, with the color becoming brighter and more orange as the temperature increases.

At beam energies of 60-150 eV, LEED patterns give information about the long range order of the top two atomic layers of a surface. A highly ordered, clean surface produces spots that are sharp and bright while most of the screen appears dark (i.e., there is no background.) If the surface is disordered or only slightly ordered, there will be no LEED pattern at these energies or the spots in the pattern will appear faint and blurry. If there is a crystalline surface below a monolayer or two of contamination, the spots will be faint and the whole screen will be fairly bright. Further discussions of the LEED phenomenon and solving LEED patterns can be found in the literature.[7]

Once a good LEED pattern is obtained, the sample can be treated to obtain a clean, ordered iodine overlayer. A variety of attempts were made to prepare the surface through various treatments in the glove box attached to the UHV system and in the electrochemical chamber. The glove box treatments involved exposing a freshly cleaned platinum sample to iodine crystals and vapour for five minutes to an hour. These procedures tended to produce surfaces that had large amounts of carbon and oxygen, contrary to the results expected from the literature.[3,4,5]

The electrochemical chamber was used to treat the sample with iodine vapour and aqueous solutions of potassium iodide (KI). For all types of treatment, the sample was translated into the electrochemical cell, and the gate valve between the cell and the glove box load-lock was sealed. For treatment with solution, the electrochemical chamber was vented with dry, oxygen-free argon, the sample was inverted over the Teflon solution cell, and fresh, dilute solutions of KI were introduced into the solution cell. The sample was then lowered toward the solution until the sample surface contacted the solution. The KI solution was then drained out, and fresh Nanopure water was introduced to rinse the sample. The water was then drained, and the chamber was pumped down to a pressure of about 1×10^{-4} torr with a liquid nitrogen cooled sorption pump. The sample could then be transferred to the main UHV system for characterization.

For treatments with iodine vapour, the Teflon base and solution cell was replaced with a stainless-steel flange equipped with venting valves. One of the valves was plumbed to the oxygen-free argon line, and the other valve was connected to a stainless-steel tube sealed at one end and packed with iodine crystals. The iodine valve could be opened to permit iodine vapour to flow into the electrochemical cell, either when the chamber was under vacuum or pressurized with argon. After the sample was exposed to iodine vapour, the residual gases were pumped off with the sorption pump, and the sample was transferred to the main system. Unfortunately, neither type of treatment produced the desired surface.

After a visit to the labs of Art Hubbard, a method that was compatible with our UHV system and yielded the desired surface was developed. This method involved treating a clean platinum single crystal with iodine at atmospheric pressure, then gently annealing the crystal in UHV while monitoring the LEED pattern. A detailed description of the procedure follows.

After cleaning by sputtering and annealing in the manner described above, the sample is removed from UHV through a rapid load-lock. The sample is loaded into the iodine dosing chamber, as shown in Figure A5. The platinum wires are connected to silver rods with silver barrel connectors to provide support and electrical connection for resistive heating. The silver rods are set into a Teflon cap that fits snugly into the top of the dosing chamber. Industrial grade argon flows through Teflon tubing and a Teflon valve into the lower inlet of the chamber. It flows out through a Teflon valve and tubing into a water bubbler. The rate of argon flow can easily be adjusted at the inlet valve.

Power is supplied by a variac with a high current limit, and connection from the variac to the rods is made with a standard power cord terminating in copper alligator clips. The level of iodine is 1-2 mm below the sample. The power is slowly increased until the wires begin to glow yellow-white and the sample is a dull red (~600 °C). The sample is held at that temperature for 3-5 minutes; the heat is then turned off and the sample is allowed to cool under a slow flow of argon for 3-5 minutes. The

cycle is then repeated, and the sample is finally allowed to cool until the Teflon cap can be removed (generally 5-10 minutes).

Some care must be taken with the materials and temperature. Silver was found to be the optimal metal for the barrel connectors. Copper and stainless steel resulted in high levels of carbon deposits on the sample surface. In addition, if the sample overheats, a form of silicon oxide deposits on the sample, either from the glass walls or from residual silicon oil contamination. Finally, solder should be avoided in any connection anywhere close to the chamber since it reacts with escaping iodine and can contaminate the sample with tin. If the sample is contaminated, several cycles of sputtering and annealing are necessary to clean it.

Upon removal from the dosing chamber, the sample is again mounted on the heating stub and returned to UHV through the fast load-lock. The surface is examined by x-ray photoelectron spectroscopy (XPS) to determine the initial iodine coverage and check for contamination. There should be little or no carbon or oxygen. A typical XPS spectrum for a freshly treated sample is shown by the upper spectrum in Figure A4. If the surface is satisfactory, the sample is transferred to the LEED/mass spectrometry chamber. At this point LEED should produce a faint (1x1) pattern with a fairly strong background at a beam energy of 65 eV.

The desired iodine overlayer is formed by a series of flash desorptions while the surface structure is monitored with LEED. Note that the ion gauge in the mass spectrometer/heating chamber must be off since it can heat the sample and cause re-ordering of the adlayer. The heating stub is plugged into the heating stage and the current is turned on for 10s intervals. The current is set a few amps lower than the current required for annealing to obtain a clean (111) LEED pattern. The LEED pattern is checked after each heating interval. The sample should not be left under the LEED electron beam for more than a few seconds, since local heating can occur, changing the structure of the iodine overlayer.

After a few heating intervals, the sample shows a bright, sharp (3x3) pattern, depicted in Figure A3b. The spots gradually blur with more heating, and the ($\sqrt{7}$x$\sqrt{7}$) pattern (shown in Figure A3c) grows in. Further heating results in the formation of the Pt(111)($\sqrt{3}$x$\sqrt{3}$)R19.1°-I overlayer, shown in Figure A3d. Once the desired pattern begins to appear, the

heating intervals are shortened to 5-7 seconds to prevent continued iodine desorption and formation of the next surface. When a bright, sharp LEED pattern for the desired surface is obtained, the sample is allowed to cool for 5-10 minutes to suppress further desorption of iodine. If the LEED pattern still shows the desired surface, XPS spectra are taken to determine the cleanliness of the surface. Figure A6 shows wide scans of each of the three adlayers. Generally, several higher resolution scans of the C1s region need to be collected and summed to determine the level of contamination. Figure A7 shows a typical wide scan spectrum and a high resolution spectrum of a clean ($\sqrt{7}$x$\sqrt{7}$) surface. A final LEED pattern is taken to insure that no re-ordering occurred during the XPS scans.

The three surfaces formed by the iodine overlayers are not equivalent. The (3x3) and ($\sqrt{7}$x$\sqrt{7}$) surfaces are both hydrophobic and reported to be stable to exposure to air.[1,4] However, experience shows that the ($\sqrt{7}$x$\sqrt{7}$) overlayer is more robust and resists contamination for a longer time. The ($\sqrt{3}$x$\sqrt{3}$) surface is hydrophilic;[4] experience shows that this surface is not air stable.[1] Consequently, while all three surfaces are suitable for experiments in UHV or under oxygen free conditions (i.e., electrochemistry under argon), the ($\sqrt{7}$x$\sqrt{7}$) surface is the more appropriate for experiments in air.

Discussion

A clean Pt(111) surface is quite sensitive to carbon contamination, and the extent of contamination affects the formation of an iodine overlayer. Consequently, not all methods of surface preparation worked equally well. The treatments carried out in the glove box and electrochemical chamber probably involved a platinum surface that was highly contaminated by the time it was exposed to iodine. While iodine is a powerful oxidizing agent and will displace contaminants under the right circumstances, it is not all powerful. Heating the sample very close to the iodine crystals is thought to activate the iodine, allowing it to etch the platinum surface as it binds to it.[1] This destroys any contaminated layers and forms a passivating, non-polar iodine layer. Further annealing under clean, UHV conditions allows selective desorption of iodine and the formation of ordered iodine overlayers on the platinum surface.

Even this procedure is not guaranteed to produce a perfect surface, as mentioned in the preparation details. Occasionally, large amounts (i.e., several monolayers) of carbon deposit on the surface along with the iodine layer. While some of this carbon is probably in a volatile form (such as carbon dioxide) and desorbs upon heating, the remainder stays and forms a layer of graphite. The presence of graphite is easily identified by the presence of rings in the LEED pattern and a large carbon signal in the XPS spectrum. This graphite overlayer can only be removed by sputtering and annealing the sample, as described above.

The LEED pattern is the accepted method for determining the adlayer structure. However, the shapes of the iodine XPS peaks are very sensitive to the positions of the iodine atoms and can also be used as a diagnostic of surface order. The most striking difference can be seen in the iodine $3d_{5/2}$ region, as shown in Figure A8. The peak corresponding to the (3x3) overlayer is intense and narrower than that corresponding to the ($\sqrt{7}$x$\sqrt{7}$) overlayer. The two peaks have almost equal areas since the overlayers contain almost equal amounts of iodine atoms, with the iodine coverage for the (3x3) adlayer being 0.44 monolayers and that for the ($\sqrt{7}$x$\sqrt{7}$) adlayer being 0.43 monolayers, as shown in Figure 9. However, the iodine atoms sit in different symmetry sites in the two overlayers, giving rise to different peak shapes.

When the iodine is in the ($\sqrt{7}$x$\sqrt{7}$) configuration, the I $3d_{5/2}$ peak shows a distinct shoulder at 618.5 eV, with the main peak appearing at 619.5 eV. The whole region can be fit to two peaks separated by 0.95 eV with an area ratio of 2:1. This can be explained by the two different sites occupied by the iodine in the unit cell.[8] As shown in Figure A9a, a given unit cell contains a total of one iodine sitting in an atop site (that is, directly on top of a platinum atom), and a total of two iodine atoms in 3-fold sites (that is, in the hollow formed by three platinum atoms).

The I $3d_{5/2}$ peak for the (3x3) structure is narrower than that for the ($\sqrt{7}$x$\sqrt{7}$) structure, which is surprising in light of the proposed lattice pattern. The unit cell is proposed to contain a total of one iodine atom in an atop site, a total of two atoms in two-fold sites, and a total of one atom in a four-fold site, as shown in Figure A9b. It is possible to fit the peak to three peaks with area ratios of 1:2:1, but the energy difference between the

peaks is less than that expected from the difference in the ($\sqrt{7}$x$\sqrt{7}$) structure.

The I $3d_{5/2}$ peak corresponding to the ($\sqrt{3}$x$\sqrt{3}$) structure is lower in intensity and narrower than the peaks for the other two structures. This is expected since the calculated coverage of iodine atoms is 0.33 monolayers. In addition, all the iodine atoms are predicted to sit in three-fold symmetry sites, as shown in Figure A9c; hence, they are chemically equivalent and give rise to one peak.

Summary

This appendix describes the preparation and characterization of three iodine overlayers on the Pt(111) surface. Each of the three surfaces has a distinctive LEED pattern and XPS spectrum. The ($\sqrt{7}$x$\sqrt{7}$) overlayer is particularly stable to exposure to air and solution and is well suited to experiments that must be performed outside of UHV conditions.

References

(1) A.T. Hubbard and D.G. Frank, personal comunication.

(2) Felter, T.E.; Hubbard, A.T. *J. Electroanal. Chem.* **1979,** *100,* 473-491.

(3) Garwood, G.A.; Hubbard, A.T. *Surf. Sci.* **1980,** *92,* 617-635.

(4) Lu, F.; Salaita, G.N.; Baltruschat, H.; Hubbard, A.T. *J. Electroanal. Chem.* **1987,** *222,* 305-320.

(5) Wieckowski, A.; Schardt, B.C.; Rosasco, S.D.; Stickney, J.L.; Hubbard, A.T. *Surf. Sci.* **1984,** *146,* 115-134.

(6) Zuraski, D.; Rice, L.; Hourani, M.; Wieckowski, A. *J. Electroanal. Chem.* **1987,** *230,* 221-231.

(7) See for example: G. Ertl and J. Küppers, *Low Energy Electrons and Surface Chemistry,* 2nd edition, VCH Publishers: Deerfield Beach, FL, 1985, pp. 210-266.

(8) DiCenzo, S.B.; Wertheim, G.K.; Buchanan, D.N.E. *Phys. Rev. B* **1984,** *30,* 553-557.

Figure A1:
Diagram of the top view of the ultrahigh vacuum (UHV) surface analysis instrument.

Pumping system:

The mass spectrometry and LEED chambers are directly connected and pumped by a CTI Cryogenics cryo pump with a pump rate of 1000 L/s; they have a baseline pressure of $<5x10^{-10}$ torr. The XPS chamber is also pumped by a 1000 L/s CTI Cryogenics cryo pump and operates at a baseline pressure of $<5x10^{-10}$ torr. The cross between the LEED chamber and the XPS chamber is pumped by a small CTI Cryogenics cryo pump and generally has a baseline pressure of $2x10^{-9}$ torr. The fast load-lock is pumped by an 80 L/s turbo pump (Varian) that is back-pumped by a mechanical pump. The glove box load-lock is pumped by a 200 L/s turbo pump (Varian) that is also back-pumped by a mechanical pump.

LEED:

The LEED unit is a VG Microtech reverse view LEED (model AEP 8011). It utilizes three-grid optics for retarding voltages and focusing, and a fluorescent screen at 5 kV versus machine ground for imaging patterns. For standard LEED operation, the electron beam has an energy range of 5-1000 eV. The assembly can also be used to obtain Auger spectra. In this mode, the beam energy is set to 3 keV, the retarding grids are used to scan the energies of the emitted electrons, and the LEED screen is used to collect the electrons. Specific details about LEED operation, maintanance, and repair can be found in the manual.

XPS:

The XPS system is an M-probe surface spectrometer (Surface Science Instruments.) The x-ray source is a focused, monochromatized Al $K_{\alpha 1,2}$ line with an energy of 1486.6eV. The incident x-ray beam strikes the surface at an angle of 55 ° off surface normal; the analyzer is also positioned at an angle of 55 ° with respect to surface normal. The energy scale of the spectrometer is calibrated to the Au $4f_{7/2}$ line (binding energy=84.00 eV) from a clean gold foil. The linearity is checked with a sputter clean copper foil using the Cu $2p_{3/2}$ line (binding energy=932.67 eV.) The instrumental line width is a function of beam size and analyzer pass energy and is calibrated with the Au $4f_{7/2}$ peak. Beam sizes and pass

energies and the corresponding nominal resolutions for the various spectra appearing in this thesis are listed here. A beam size of 400x1000 μm^2 and an analyzer pass energy of 155 eV results in a nominal full width at half maximum (FWHM) of the Au $4f_{7/2}$ peak of 1.50 eV. For a nominally circular beam of 300 μm diameter and a pass energy of 155 eV, the FWHM of the Au $4f_{7/2}$ peak is 1.45 eV. For a nominally circular beam of 300 μm diameter and a pass energy of 105 eV, the FWHM of the Au $4f_{7/2}$ peak is 1.25 eV. For a nominally circular beam of 300 μm diameter and a pass energy of 54 eV, the FWHM of the Au $4f_{7/2}$ peak is 0.90 eV.

Mass spectrometer:

The mass spectrometer is a VG quadrapole Sensorlab linked to a PC computer. The quadrapole has a mass detection range of 1-300 AMU and uses Faraday and electron multiplier detectors. The minimum detectable partial pressure is nominally $4x10^{-14}$ torr.

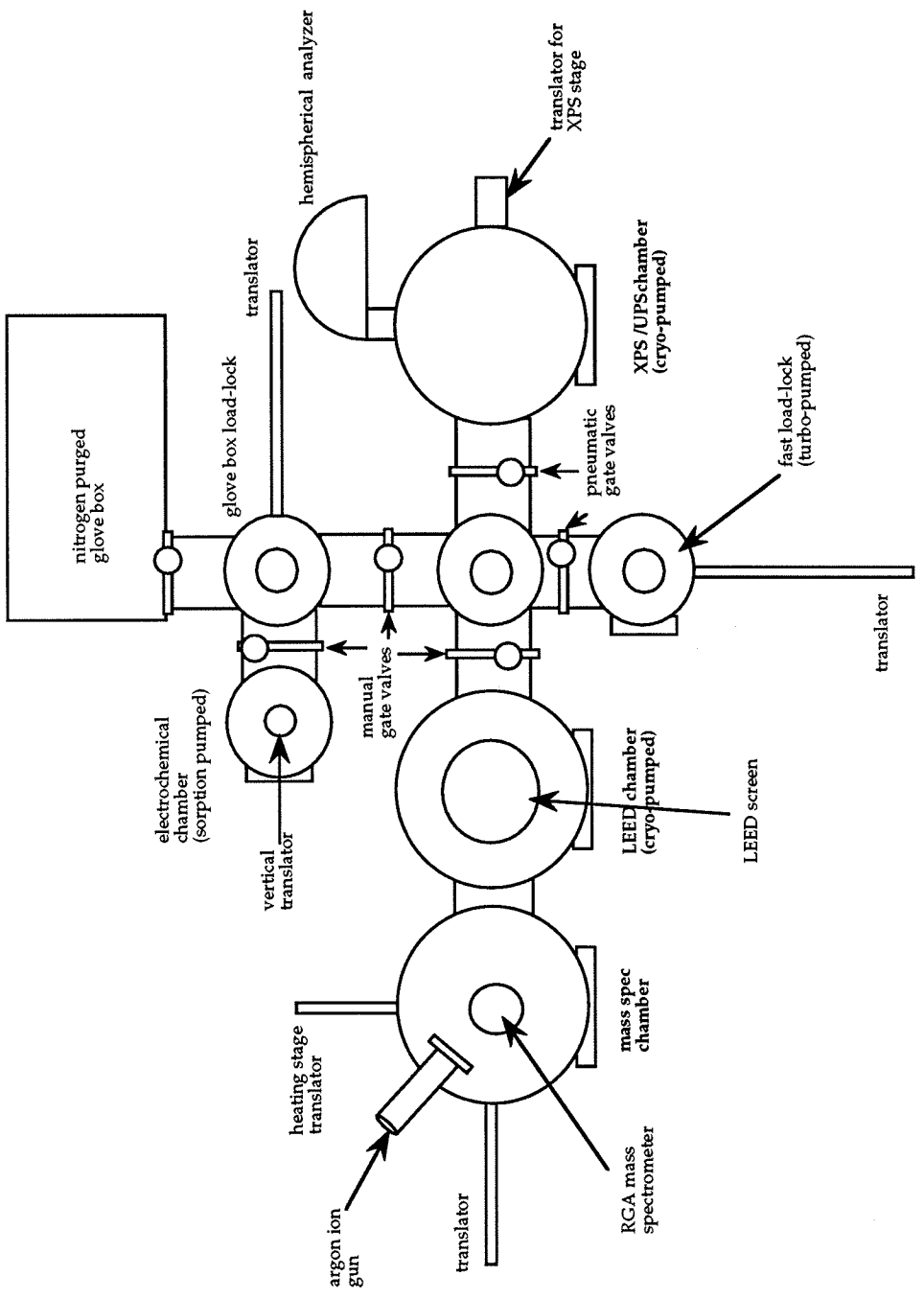
nitrogen purged glove box
glove box load-lock
translator
hemispherical analyzer
translator for XPS stage
XPS /UPSchamber (cryo-pumped)
pneumatic gate valves
fast load-lock (turbo-pumped)
translator
electrochemical chamber (sorption pumped)
vertical translator
manual gate valves
LEED chamber (cryo-pumped)
LEED screen
heating stage translator
mass spec chamber
argon ion gun
translator
RGA mass spectrometer

Figure A2:
A representation of the sample mounted on the heating stub. The oriented and polished face of the crystal should be flat and centered over the central post of the stub to produce the best LEED pattern.

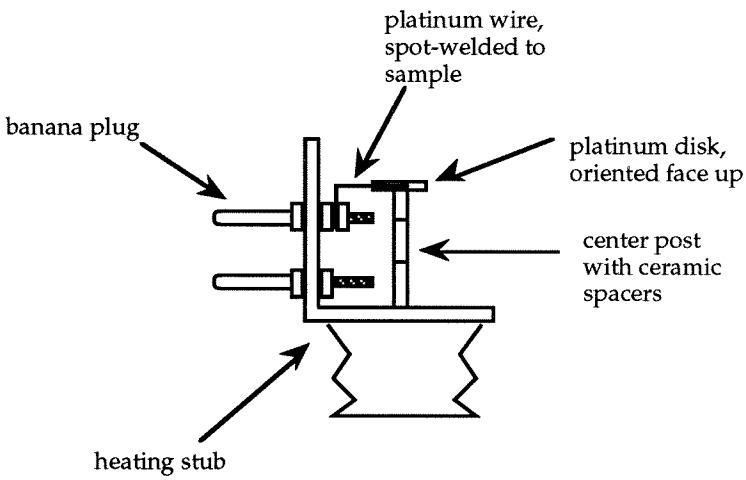
platinum wire,
spot-welded to
sample
banana plug
platinum disk,
oriented face up
center post
with ceramic
spacers
heating stub

side view

Figure A3:

a: Typical LEED pattern of a clean, annealed Pt(111)(1x1) surface at a beam energy of 70 eV.

b: Typical LEED pattern of a Pt(111)(3x3)-I surface at a beam energy of 70 eV.

c: Typical LEED pattern of a Pt(111)($\sqrt{7}$x$\sqrt{7}$)R19.1°-I surface (with a ($\sqrt{3}$x$\sqrt{3}$)R30° pattern beginning to grow in) at a beam energy of 64 eV.

d: Typical LEED pattern of a Pt(111)($\sqrt{3}$x$\sqrt{3}$)R30°-I surface at a beam energy of 65 eV.

All photographs were taken with an aperature setting of 2.82 and exposure times of either 15 or 30 sec. The sample was slightly off normal to the electron beam and the screen, hence the patterns are slightly off-center.

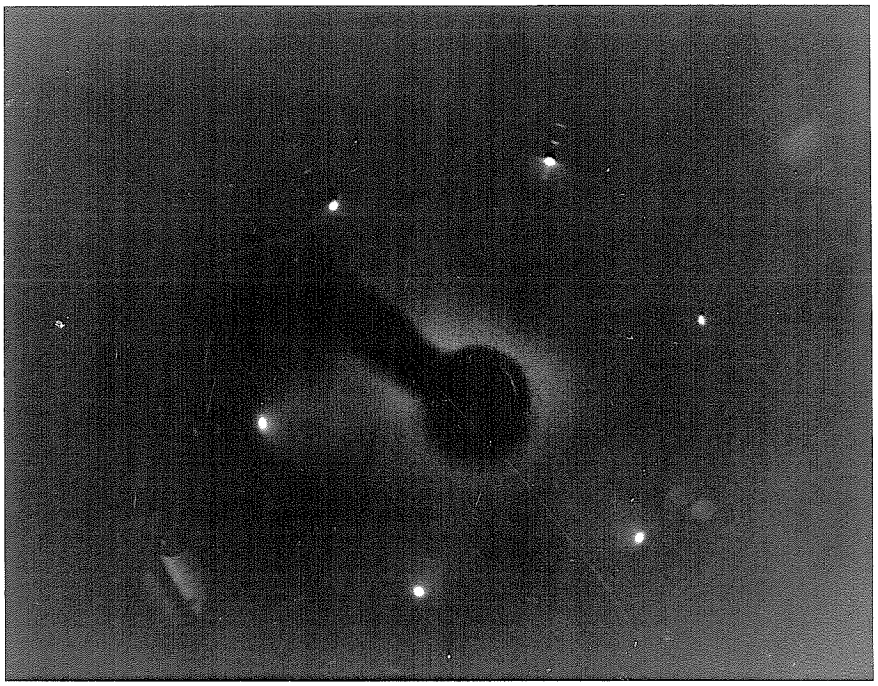

a.

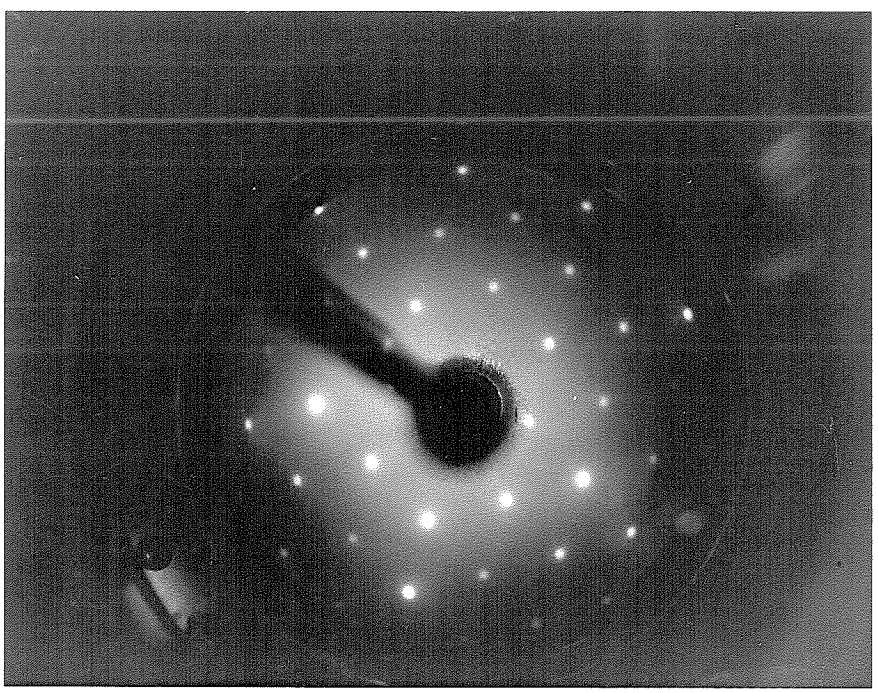

b.

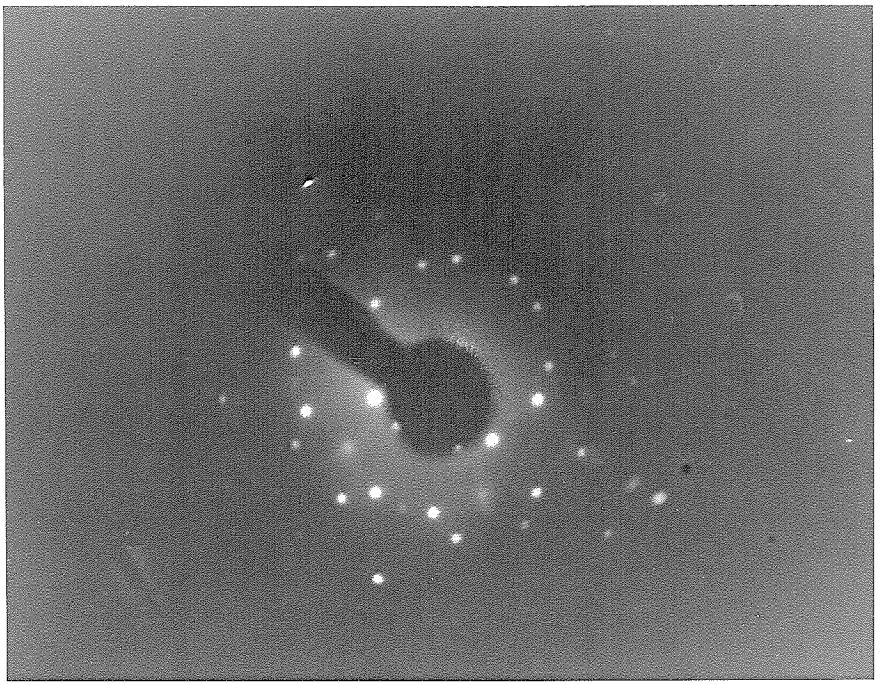

c.

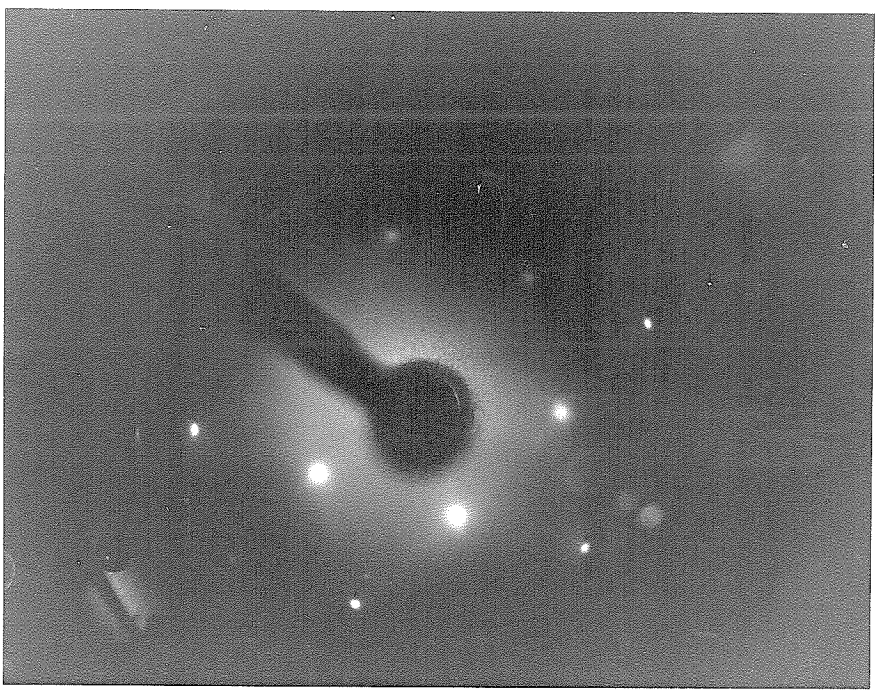

d.

Figure A4:
A comparison of the XPS spectra for a clean platinum surface (lower spectrum) and a freshly treated Pt-I surface (upper spectrum). The major platinum and iodine peaks and the C1s peak are labelled. Both spectra were taken with a beam size of 400x1000 μm^2 and a pass energy of 155 eV. With this beam size and pass energy, the nominal FWHM of the Au $4f_{7/2}$ peak is 1.50 eV.

XPS spectra of clean Pt vs. Pt freshly treated with I

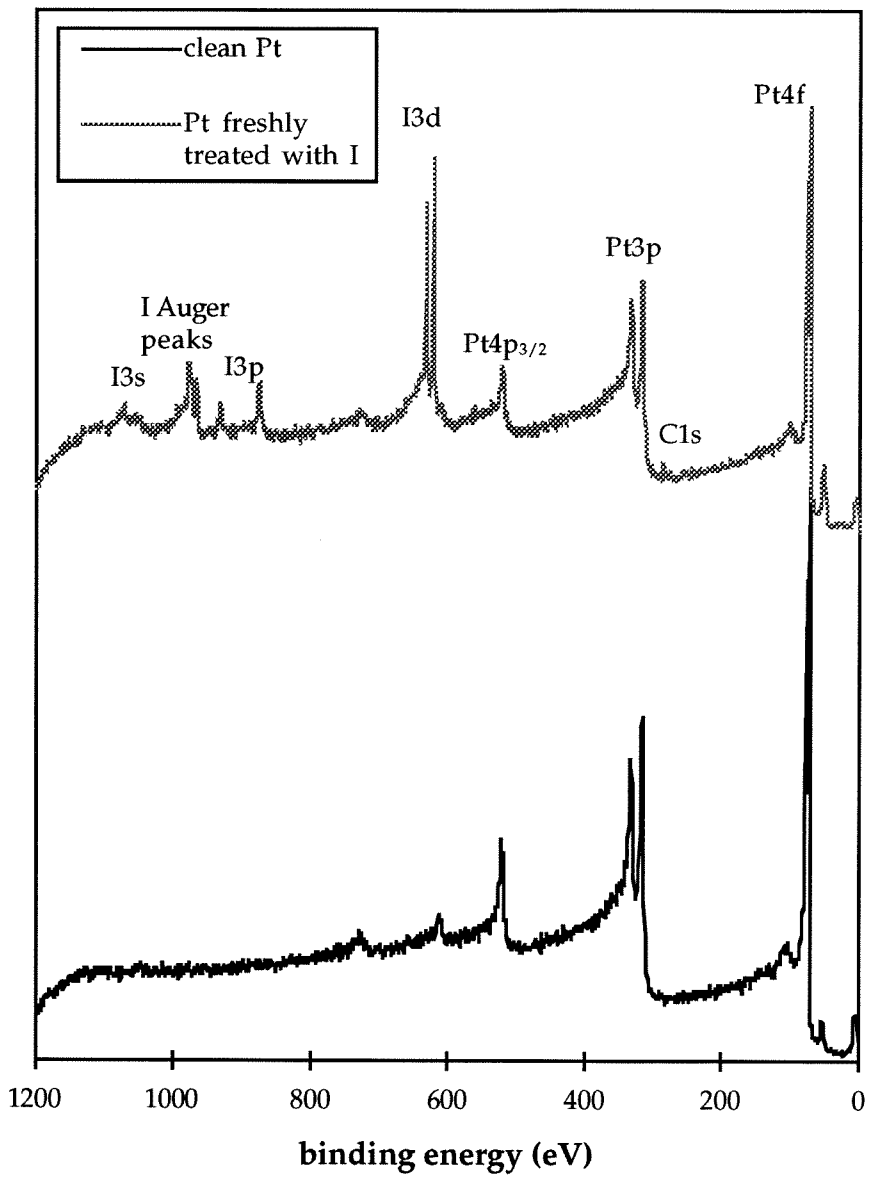

Figure A5:
The platinum sample as mounted in the iodine dosing chamber. The sample is suspended from silver rods a few millimeters above the iodine crystals. Silver barrel connectors provide physical and electrical connection.

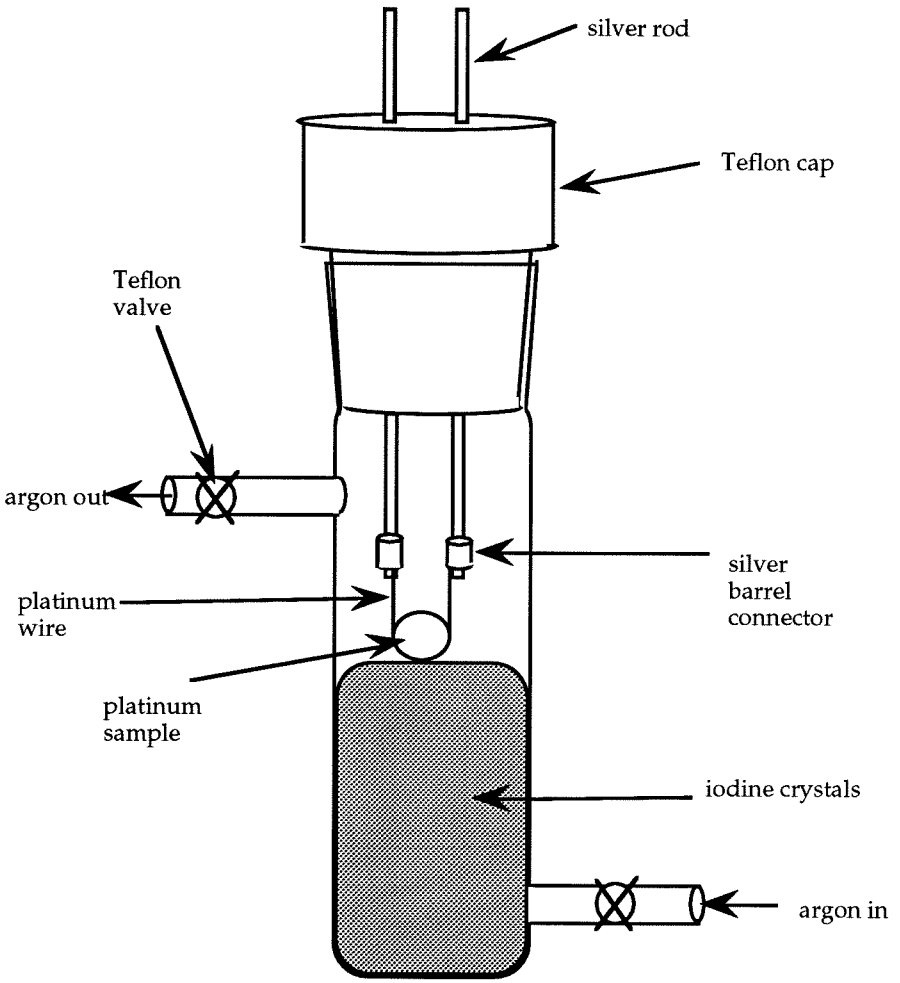
silver rod
Teflon cap
Teflon
valve
argon out
silver
barrel
connector
platinum
wire
platinum
sample
iodine crystals
argon in

Figure A6:
Typical XPS spectra of the three Pt-I overlayers. All spectra were taken with a beam size of 400x1000 μm^2 and a pass energy of 155 eV on roughly the same spot on the sample. With this beam size and pass energy, the nominal FWHM of the Au $4f_{7/2}$ peak is 1.50 eV. Each spectrum represents one scan. All three spectra are free of carbon and oxygen, and the intensities of the I 3d peaks decrease going from the (3x3) to the ($\sqrt{7}$x$\sqrt{7}$) to the ($\sqrt{3}$x$\sqrt{3}$) surfaces.

XPS spectra of various Pt-I adlayers

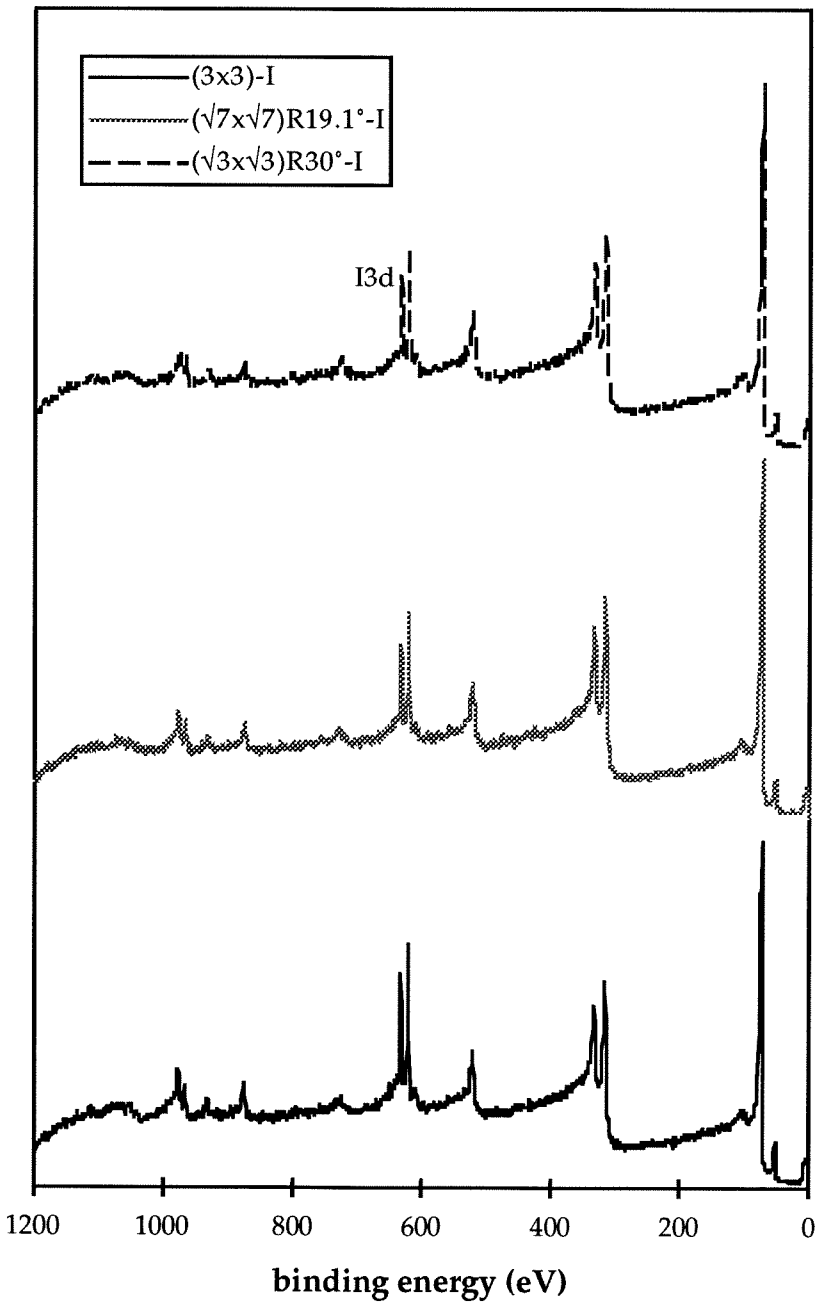

Figure A7:

a: A typical XPS spectrum for the Pt(111)($\sqrt{7}$x$\sqrt{7}$)R19.1°-I surface. The spectrum represents a single scan taken with a beam diameter of 300 μm and a pass energy of 155 eV. With this beam size and pass energy, the FWHM of the Au $4f_{7/2}$ peak is 1.45 eV.

b: A higher resolution scan of the C 1s region taken at the same spot as the above spectrum. The region was scanned for 3 minutes using the 300 μm beam size and a pass energy of 105 eV. With this beam size and pass energy, the FWHM of the Au $4f_{7/2}$ peak is 1.25 eV. This spectrum represents the sum of 180 scans. Note that the region is very flat, indicating that any carbon present is below the detection limit of the instrument, which is nominally a tenth of a monolayer.

Pt(111)(√7x√7)-I, survey scan

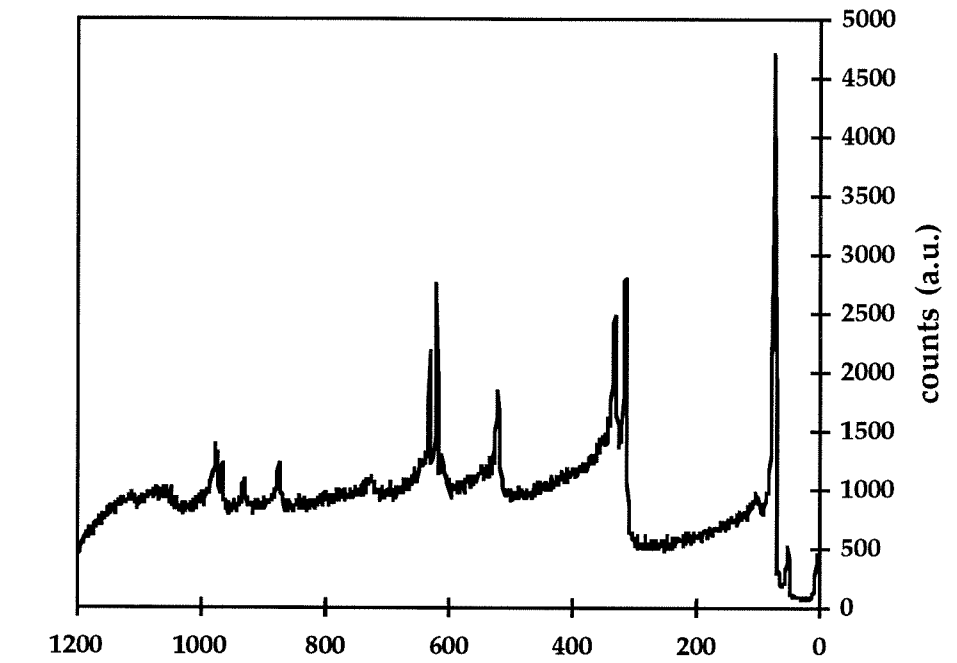

a.

Pt(111)(√7x√7)-I, C1s region

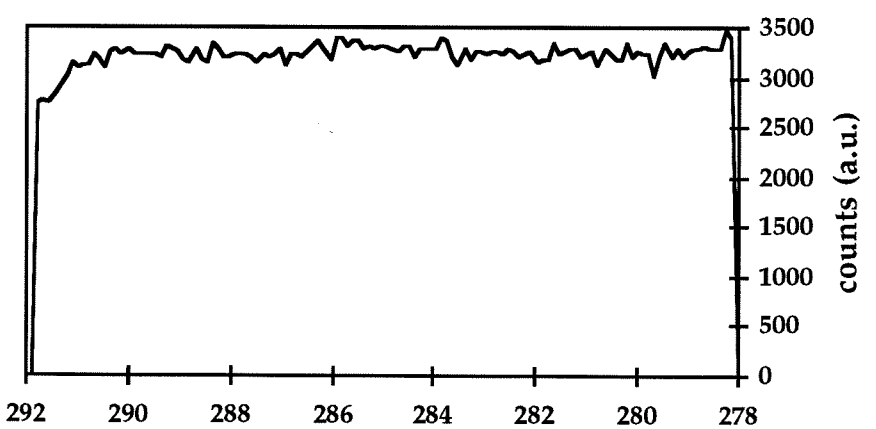

b.

Figure A8:
Typical XPS spectra of the I $3d_{5/2}$ region for three different overlayers of iodine on platinum. The text explains the difference in intensities and shapes for the three peaks. Each spectrum corresponds to a high resolution scan acquired for 3 minutes with a pass energy of 54 eV and a beam size of 300 μm. With this beam size and pass energy, the FWHM of the Au $4f_{7/2}$ peak is 0.90 eV. Each spectrum represents the sum of 180 scans.

I3d$_{5/2}$ region for three adlayers

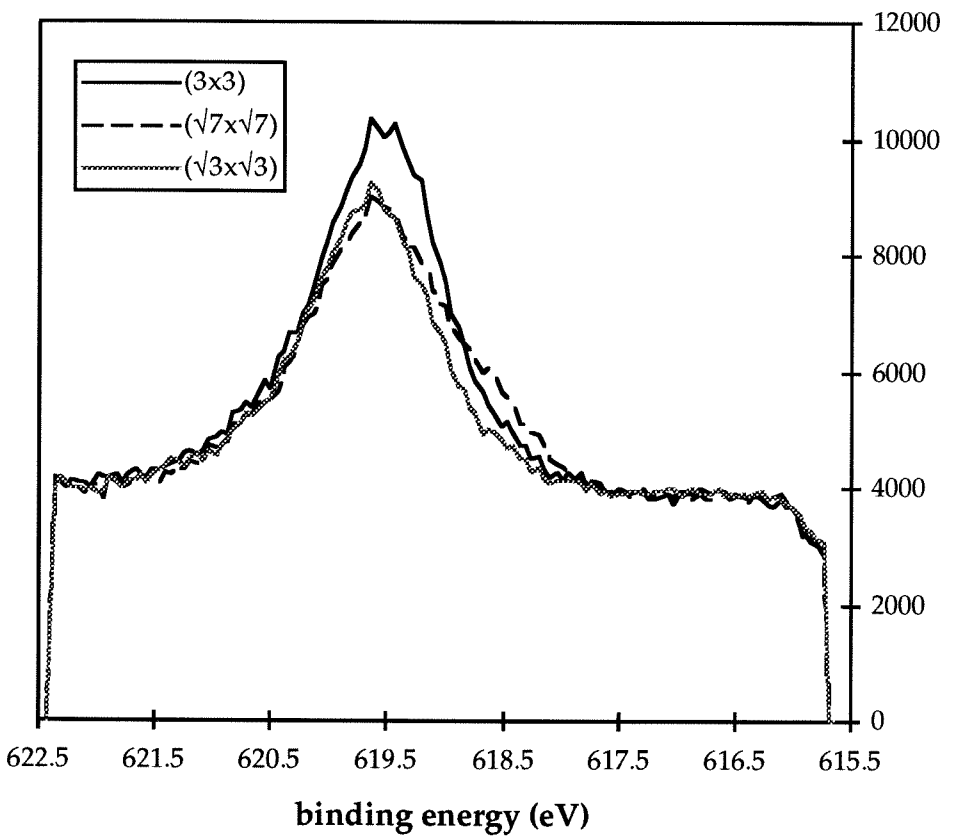

Figure A9:

a: A schematic depiction of the Pt(111)(3x3)-I lattice structure. The grid represents the Pt(111) surface, with each intersection corresponding to a platinum atom. The open circles represent iodine atoms, and the unit cell is outlined in dashed lines. Each unit cell contains a total of four iodine atoms and nine platinum atoms, corresponding to an iodine coverage of 4/9 or 0.44 monolayers.

b: A schematic depiction of the Pt(111)($\sqrt{7}$x$\sqrt{7}$)R19.1°-I lattice structure. Each unit cell contains a total of three iodine atoms and seven platinum atoms, corresponding to an iodine coverage of 3/7 or 0.43 monolayers.

c: A schematic depiction of the Pt(111)($\sqrt{3}$x$\sqrt{3}$)R30°-I lattice structure. Each unit cell contains a total of one iodine atom and three platinum atoms, corresponding to an iodine coverage of 1/3 or 0.33 monolayers.

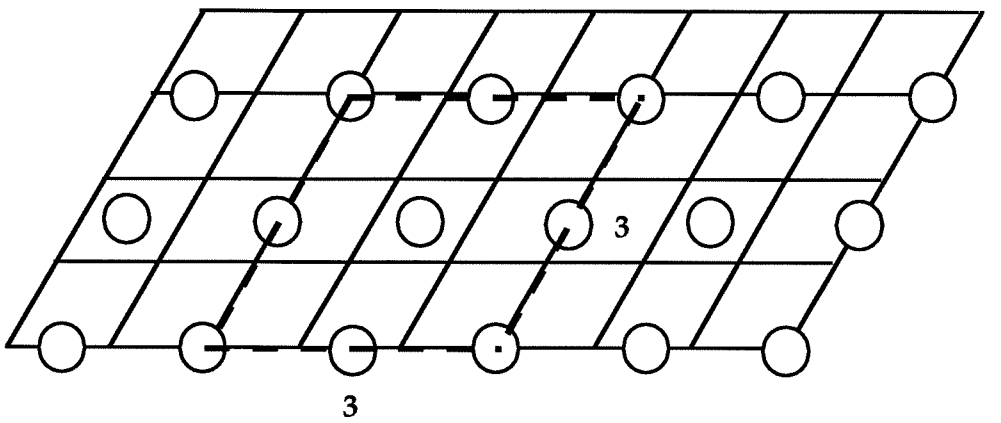

a.

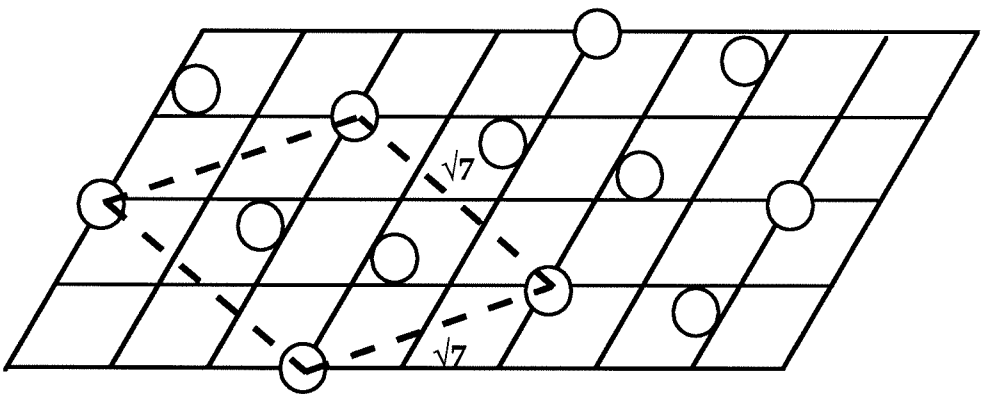

b.

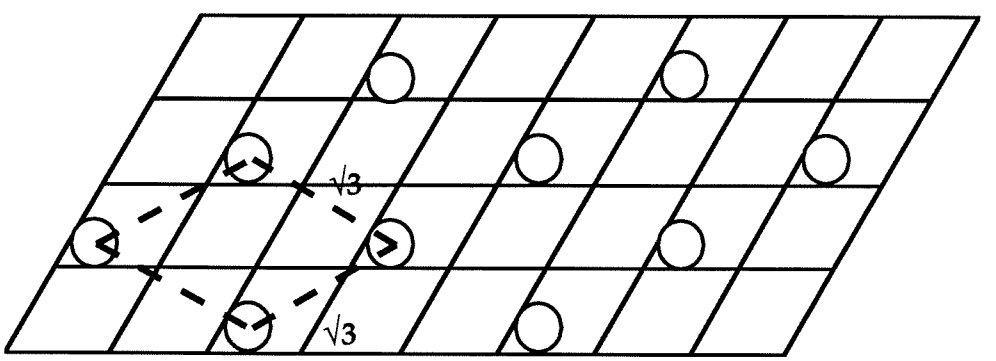

c.